1·0

2·8

2·5

3·15

2·2

3·5

1·1

4·0

2·0

4·5

1·8

1·25 1·4 1·6

NATIONAL BUREAU OF STANDARDS
MICROCOPY RESOLUTION TEST CHART

AD–A158 058

A THEORETICAL INVESTIGATION

OF

ACOUSTIC CAVITATION*

DTIC
ELECTE
AUG 1 5 1985

A

THE UNIVERSITY OF MISSISSIPPI
PHYSICAL ACOUSTICS RESEARCH GROUP
DEPARTMENT OF PHYSICS AND ASTRONOMY

85   8   12   104

Technical Report for

Office of Naval Research

Contract N00014-84-C-0193

A THEORETICAL INVESTIGATION

OF

ACOUSTIC CAVITATION*

by

K. W. Commander and L. A. Crum
Physical Acoustics Research Laboratory
Department of Physics and Astronomy
The University of Mississippi
Oxford, MS 38677
July 15, 1987

AUG 1 5 1985

A

*Ph.D. Dissertation by first-named author.

SECURITY CLASSIFICATION OF THIS PAGE *(When Data Entered)*

REPORT DOCUMENTATION PAGE	READ INSTRUCTIONS BEFORE COMPLETING FORM	
1. REPORT NUMBER 4-85	**2. GOVT ACCESSION NO** AD-A158058	**3. RECIPIENT'S CATALOG NUMBER**
4. TITLE (and Subtitle) A Theoretical Investigation of Acoustic Cavitation	**5. TYPE OF REPORT & PERIOD COVERED** Technical	
	6. PERFORMING ORG. REPORT NUMBER	
7. AUTHOR(s) K. W. Commander and L. A. Crum	**8. CONTRACT OR GRANT NUMBER(s)** N00014-84-C-0193	
9. PERFORMING ORGANIZATION NAME AND ADDRESS Physics Acoustics Research Laboratory Department of Physics and Astronomy University of MS, Oxford, MS 38677	**10. PROGRAM ELEMENT, PROJECT, TASK AREA & WORK UNIT NUMBERS**	
11. CONTROLLING OFFICE NAME AND ADDRESS	**12. REPORT DATE** July 15, 1985	
	13. NUMBER OF PAGES 112	
14. MONITORING AGENCY NAME & ADDRESS(if different from Controlling Office)	**15. SECURITY CLASS. (of this report)** Unclassified	
	15a. DECLASSIFICATION/DOWNGRADING SCHEDULE	

16. DISTRIBUTION STATEMENT (of this Report)

Approved for Public Release: Distribution Unlimited

17. DISTRIBUTION STATEMENT (of the abstract entered in Block 20, if different from Report)

18. SUPPLEMENTARY NOTES

19. KEY WORDS (Continue on reverse side if necessary and identify by block number)

Nonlinear dynamics
Cavitation
Bubbles

20. ABSTRACT (Continue on reverse side if necessary and identify by block number)

See following page.

DD , FORM, 1473 1 JAN 73 EDITION OF 1 NOV 65 IS OBSOLETE
S/N 0102- LF- 014- 6601

SECURITY CLASSIFICATION OF THIS PAGE *(When Data Entered)*

Interest in cavitation dates back to the mid 1800's; however, there was no significant theoretical work in this area until the paper by Lord Rayleigh in 1917 described the collapse of a spherical cavity. Since this time there have been contributions to the theory by many scientists. In the late 1940's and early 1950's, contributions by Blake, Plesset, Neppiras, Noltingk, and Poritsky significantly advanced the theory resulting in an equation for the bubble dynamics known as the Rayleigh-Plesset equation. This equation was shown to work quite well under some conditions.

Recent experiments have shown that when the acoustic driving frequency is near one of the bubble's harmonic resonances, the theoretical values predicted by the Rayleigh-Plesset equation are inconsistent with observed values. This inconsistency lead Prosperetti to consider the internal pressure term in the Rayleigh-Plesset equation in a more general manner. In the past the internal pressure of a bubble was assumed to be accurately predicted by a polytropic approximation. Prosperetti considered the internal pressure from the conservation equations, resulting in a much more accurate formulation.

This study is an analysis of the two methods, showing where they agree and where they disagree. The new formulation also provides additional information about the internal thermodynamics of a bubble, which is explored in some detail. Results are shown for the internal temperature of a cavitating bubble as a function of radial coordinate and time. Internal pressures for a variety of conditions are shown and are in good agreement with earlier predicted values.

Finally, the different models of acoustic cavitation are examined using some of the recent techniques in dynamical systems. "Feigenbaum trees" were made for the two models of interest. This method for analyzing an equation was shown to be very sensitive to the internal pressure term, and thus it is an appropriate method for comparing different acoustic cavitation theories.

TABLE OF CONTENTS

Page

LIST OF FIGURES

INTRODUCTION

The focus of this dissertation is on numerical modeling of stable acoustic cavitation. Neppiras [1] defines stable acoustic cavitation as the oscillation of cavities or bubbles about some equilibrium size. In general the oscillations need not be linear, but may vary with time in a very complex manner. The adjective stable implies that the bubble exists for many cycles without breaking up or dissolving. On the other hand, a transient cavitation event is one which usually exists for one cycle or less. The bubble grows to several times its equilibrium size and then collapses violently breaking into many smaller bubbles. We will only deal with stable cavitation here.

Before pressing onward with the latest acoustic cavitation theories, let us briefly examine the short history of this field of Physics. Interest in cavitation dates back to Besant [2] in 1859. However, there was no significant theoretical work in this field until that of Rayleigh [3] in 1917. This paper by Rayleigh described the collapse of a spherical cavity. Of course Lord Rayleigh is most famous for his treatise The Theory of Sound which he started writing while on vacation in Egypt in 1872. This monumental work took five years to reach the press and it is a credit to Rayleigh's abilities that it is still considered today as the foundation of physical acoustics.

Between Rayleigh's paper in 1917 and the late 1940's, all

1

theoretical work in cavitation was concerned with hydrodynamically-generated cavitation, usually by propellers on ships. In 1949 Blake [4] published the first systematic study on acoustic cavitation. Shortly after this publication, the classic papers by Plesset [5], Neppiras and Noltingk [6,7], and Poritsky [8] appeared that significantly advanced the theory. It was about this time that many groups began working on the problem of acoustic cavitation. Plesset added variable pressure and surface tension terms to the theory of Rayleigh and for his contribution the resulting equation with a damping term added by Poritsky is called the Rayleigh-Plesset equation. This equation is derived and discussed in chapter 1.

The basic problem of acoustic cavitation is to find the pressure and velocity fields of the two phase medium consisting of a bubble or cavity and a surrounding fluid which theoretically extends to infinity. Recent advances in ultrasonic instruments used for medical purposes have made a knowledge of the internal temperature of an oscillating bubble important as well. High temperatures in the interior of the bubble can produce free radicals which could be dangerous to biological systems [9]. In practice the bubble's radius as a function of time is also of interest as well. Although the new theoretical model is very complex and requires a lot of computer time for its solution, all of the quantities mentioned above can be obtained from its solution.

In this study numerical methods are used extensively to solve the basic equations of acoustic cavitation for the case of a spherically

oscillating bubble in which the internal pressure is defined by a method suggested by Prosperetti [10]. A thorough comparison with previous results will be made to see just what parameter values necessitate the use of this more complex model. In chapter 4 it will be shown that this new theory leads to a different type of coupling between the liquid and gas phases through the use of "Feigenbaum trees" [11,12].

The most elementary model of acoustic cavitation considered here is the Rayleigh-Plesset equation, derived by Plesset [5] with the viscous damping term added by Poritsky [8]. Extensive numerical investigations were carried out for this equation by Noltingk and Neppiras [6,7] and later by Flynn [13,14]. Since that time several approximate analytical solutions to the Rayleigh-Plesset equation have been derived, including a solution to second order in the asymptotic expansion by Prosperetti [15]. These solutions were thought to be adequate until recent experimental data showed a large deviation between theory and experiment for driving frequencies in the vicinity of a harmonic of the resonance frequency of the bubble. It will be shown that the new theory is closer to experimental data in these sensitive frequency ranges and thus is a better model for the thermal damping in the bubble.

The first chapter contains a brief derivation of some of the basic equations in cavitation. Included in this section are the well-known Rayleigh equation and the Rayleigh-Plesset equation. The more advanced equations for radial bubble oscillations are discussed as well and relationships between them are pointed out. After establishing the

heating term is given by Prosperetti [8] as

$$\rho c_p\left(\frac{dT}{dt}\right) + \frac{T}{\rho}\left(\frac{\partial\rho}{\partial T}\right)_p \frac{dP}{dt} = \nabla \cdot (K\nabla T), \tag{40}$$

where T is the internal temperature, c_p the specific heat of the gas at constant pressure, and K is the thermal conductivity of the gas. Multiplication of equation (38) by $c_p T$ and adding it to equation (40) results in

$$\frac{d}{dt}\left(\rho c_p T\right) + \frac{T}{\rho}\left(\frac{\partial\rho}{\partial T}\right)_p \frac{dP}{dt} = \nabla \cdot (K\nabla T). \tag{41}$$

Using the ideal gas assumption it is easy to show that

$$\rho c_p T = \frac{\gamma}{\gamma-1} P \quad \text{and} \quad \left(\frac{T}{\rho}\right)\left(\frac{\partial\rho}{\partial T}\right)_p = -1. \tag{42}$$

Sustituting equations (42) and (37) into (41) results in

$$\frac{\dot{P}}{\gamma P} + \nabla \cdot \left(U - \left[\frac{\gamma-1}{\gamma P}\right]K\nabla T \right) = 0. \tag{43}$$

Because of the previously assumed spherical symmetry, one can multiply both sides of equation (43) by dV and integrate. Applying the divergence theorem to the second term yields the following

$$\int\left(\frac{1}{\gamma P}\right)\frac{dP}{dt} \, dV + \int\left(U - \left[\frac{\gamma-1}{\gamma P}\right]K\nabla T\right) \, dA = 0. \tag{44}$$

Carrying out the integration yields

$$\frac{4\pi r^3 \dot{P}}{3\gamma P} + \left(U - \left[\frac{\gamma-1}{\gamma P}\right]K\frac{\partial T}{\partial r}\right)4\pi r^2 = 0. \tag{45}$$

Now, solving for the gas velocity U gives

$$\rho \left(\frac{\partial U}{\partial t} + U \frac{\partial U}{\partial r} \right) + \frac{\partial P}{\partial r} = \nabla \cdot \underline{\underline{\tau}} , \qquad (35)$$

where ρ, P, U, and $\underline{\underline{\tau}}$ denote the density, pressure, radial velocity, and viscous stress tensor of the gas in the bubble. $r = 0$ corresponds to the center of the bubble and $r = R$ corresponds to the wall of the bubble of radius R. The boundary conditions for the velocity are

$$U(r=0,t) = 0 \text{ and } U(r=R,t) = dR/dt. \qquad (36)$$

From the assumption of spherically symmetric oscillations and radial gas velocities, it is clear that the internal pressure P_i is only a function of the radial coordinate r and time t. In section C of this chapter we will show that order of magnitude estimates reveal that we can replace equation (35) by

$$P_i = P_i(t) \text{ or } P_i = P_i(R) \qquad (37)$$

since $R = R(t)$.

Next, the continuity equation is considered (see for example Batchler [23])

$$\frac{D\rho}{Dt} + \rho \nabla \cdot U = 0 , \qquad (38)$$

where

$$\frac{D}{Dt} = \frac{\partial}{\partial t} + U \frac{\partial}{\partial r} . \qquad (39)$$

Finally, the conservation of energy equation without the viscous

B.   An exact formulation for the internal pressure

The need for a more accurate expression for the internal pressure
of a bubble as a function of both the bubble radius and time led
Prosperetti [10] to a direct approach using the conservation equations
for the interior of a bubble. The derivations that follow are along the
lines given by Prosperetti.

Certain assumptions about the geometry of the bubble oscillations
and the nature of the gases and liquids will be made from the start of
the derivation.   These assumptions set some limitations on the theory
that follows.   These limitations will be discussed in detail in section
C of this chapter.

The first assumption made is that the bubble oscillations are
spherical and that the velocity of the gas in the bubble is only a
function of a radial coordinate and time.   Fanelli et. al. [41] have
shown that diffusion of gas in and out of the bubble is only important
at low ambient pressures and hence the assumption of no mass transport
across the bubble wall is appropriate.   This study is only concerned
with bubble oscillations in water at or near room temperature.   Since
the vapor pressure of water at room temperature is small compared to
that of the gas in the bubble, it is neglected in our derivation.   The
final assumption is that the gas in the bubble is an ideal gas.

The momentum conservation equation can be written as follows (see
for example Aris [24])

Until recently the polytropic approximation was thought to be quite accurate over a wide range of driving pressures, frequencies, and bubble radii that are of interest. However, Crum and Prosperetti [19] have shown that the polytropic approximation can give quite different results when the driving frequency is in the vicinity of one of the harmonics of the resonance frequency of the bubble. It is this difficulty that led Prosperetti to search for a better expression for the internal pressure, which is the subject of the next section.

reference [18]. Even though equation (28) looks quite different from (26), substitution of

$$H = (P - P_\infty)/\rho_\infty \qquad (32)$$

into (28) with C held constant simplifies (28) to (26). Thus, these two equations are actually quite similar.

To this point, only the fundamental equations for radial oscillations have been discussed and not the problem of how to model the internal pressure. For some time now the internal pressure has been approximated by an expression involving a polytropic exponent of the form given by Zwick [40]

$$P_i = P_0 (R_0/R)^{3\kappa} . \qquad (33)$$

Here κ is the polytropic exponent and P_0 is the internal pressure of the bubble at equilibrium defined by

$$P_0 = P_\infty + 2\sigma/R_0 , \qquad (34)$$

where R_0 is the equilibrium radius of the bubble (note that equation (30) is of this form as well). Using this approximation for P_i, it is straightforward to solve equation (25) numerically using a fourth order Runge-Kutta method to a high degree of precision. There are of course other numerical methods to solve this type of second order nonlinear ordinary differential equation, but the Runge-Kutta method is probably the most widely used and suffices here.

by the condition on the normal stresses

$$P_i(R,t) = P(R,t) + 2\sigma/R + 4\mu\dot{R}/R. \tag{27}$$

It is easy to show that as c approaches infinity, equation (26) simplifies to the Rayleigh-Plesset equation (25).

There are numerous equations equivalent to or similar to equation (26) in the literature [30,32,35,37]. Prosperetti [38] has discussed this fact and argues in favor of equation (26) for reasons of better numerical convergence. For this reason equation (26) is used as one of the fundamental equations for this study.

Another equation which is very popular in the literature is that by Gilmore [30]; however, the form used here is given by Lauterborn and Suchla [18] as

$$R\left(1 - \frac{\dot{R}}{c}\right)\ddot{R} + \frac{3}{2}\left(1 - \frac{\dot{R}}{3c}\right)\dot{R}^2 - \left(1 - \frac{\dot{R}}{c}\right)H - \frac{\dot{R}}{c}\left(1 - \frac{\dot{R}}{c}\right)R\frac{dH}{dR} = 0, \tag{28}$$

where H is the free enthalpy, which for water is given by

$$H = \frac{n}{n-1}\frac{A^{1/n}}{\rho_0}\{[P(R) + B]^{(n-1)/n} - (P_\infty + B)^{(n-1)/n}\}. \tag{29}$$

The pressure at the bubble wall P(R) and the speed of sound c are given by

$$P(R) = \left(P_0 + \frac{2\sigma}{R}\right)\left(\frac{R_n}{R}\right)^{3\gamma} - \frac{2\sigma}{R} - \frac{4\mu\dot{R}}{R} \tag{30}$$

and

$$C = [C_0^2 + (n-1)H]^{\frac{1}{2}}. \tag{31}$$

Typical values of the constants in these equations are given in

time, the solution of (21) is of the form

$$\phi = Ar^k + Br^{-k}. \tag{23}$$

The boundary conditions imply that $A = 0$, $k = 1$, and $B = -RR^2$. Thus, equation (23) becomes

$$\phi = - \frac{\dot{R}R^2}{r}. \tag{24}$$

Now substituting equations (24) and (20) into (22) yields the Rayleigh-Plesset equation

$$R\ddot{R} + \frac{3}{2}\dot{R}^2 = \frac{1}{\rho}\left[P_g(R,t) - P_s(t) - \frac{2\sigma}{R} - \frac{4\mu\dot{R}}{R}\right]. \tag{25}$$

There are many equations in the literature describing spherical bubble oscillations [37]. Probably the best-known of these equations is the Rayleigh-Plesset equation (25). One of the limitations of this equation is the assumption of an incompressible liquid. This implies that the speed of sound in the liquid must be infinite. Prosperetti [38] has shown that following the procedure used by Keller and Miksis [39] the following equation of motion for the radial bubble oscillations can be obtained

$$\left(1 - \frac{\dot{R}}{c}\right)R\ddot{R} + \frac{3}{2}\dot{R}^2\left(1 - \frac{\dot{R}}{3c}\right) = \left(1 + \frac{\dot{R}}{c}\right)\frac{P(R,t) - Ps(t+R/c)}{\rho} + \frac{R}{\rho c}\frac{dP(R,t)}{dt}. \tag{26}$$

Here $P(r,t)$ is the pressure on the external side of the bubble wall. The pressure $P(R,t)$ is related to the internal bubble pressure $P_i(r,t)$

$$\frac{\partial \phi}{\partial t} + \frac{1}{2}(\nabla\phi)^2 + h = 0. \tag{18}$$

Setting the right hand side of equation (18) equal to zero implies that ϕ approaches zero as r approaches infinity. The other boundary conditions on equations (17) and (18) are

$$\left(\frac{\partial \phi}{\partial t} = \dot{R}\right)\Bigg|_{r=R(t)} \tag{19}$$

and

$$P_g(R,t) = P(R,t) + \frac{2\sigma}{R} + 4\mu\dot{R}/R, \tag{20}$$

where P_g is the pressure in the bubble, P the pressure on the liquid side of the interface, and σ the surface tension of the liquid. Equations (17) and (18) together with the boundary conditions (19) and (20) have been the subject of considerable theoretical work [30-37].

The equations above can be simplified by assuming in the continuity equation that the speed of sound c is infinite, implying that the density ρ is constant. These assumptions reduce equation (17) to Laplace's equation

$$\nabla^2 \phi = 0 \tag{21}$$

and equation (18) to

$$\frac{\partial \phi}{\partial t} + \frac{1}{2}(\nabla\phi)^2 + \frac{P-P_0}{\rho} = -\frac{P_s(t)}{\rho}, \tag{22}$$

where P_s is the variable part of the pressure in the liquid. Since these equations are only dependent on the radial space coordinate and

where

$$\frac{D}{Dt} = \frac{\partial}{\partial t} + U \cdot \nabla . \tag{13}$$

Here, μ is the viscosity of the liquid and ρ is the density of the liquid, both assumed to be constant. For our purposes the term in equation (12) involving the viscosity is small, and together with equation (9) we can write equation (12) as

$$\frac{\partial u}{\partial t} + u\frac{\partial u}{\partial r} = - \frac{1}{\rho}\frac{\partial P}{\partial r} . \tag{14}$$

Considered here are bubble oscillations where the internal temperature remains low enough so that evaporation and condensation at the interface can be neglected. This assumption allows us to treat the liquid as isothermal and an equation of state involving the pressure and density can be assumed, which leads to the following expressions involving the molar enthalpy h and the speed of sound c [28]

$$\rho dh = dP \quad \text{and} \quad c^2 d\rho = dP. \tag{15}$$

Assuming a velocity potential ϕ such that

$$U = \nabla\phi \quad \text{and} \quad u = \frac{\partial\phi}{\partial r}, \tag{16}$$

the continuity equation (11) becomes

$$\nabla^2\phi + \frac{1}{c^2}\left(\frac{\partial h}{\partial t} + \frac{\partial\phi}{\partial r} \frac{\partial h}{\partial r}\right) = 0. \tag{17}$$

Performing one integration results in the Bernoulli integral

This famous equation can be very useful as a starting point in deriving acoustic cavitation theories.

Next, the acoustic cavitation equations are derived by starting from first principles – namely the conservation equations. Since spherically symmetric oscillations are dealt with exclusively, the velocity in spherical coordinates is given by

$$U = u\hat{e}_r, \text{ where } u = |U|. \tag{9}$$

There are numerous texts in fluid mechanics and transport phenomena, but several advanced texts that are particularly useful are those by Batchelor [23], Aris [24], Bird, Stewart, and Lightfoot [25], and Landau and Lifshitz [26]. Some intermediate texts that are useful are those by Lu [27], John [28], and Bertin and Smith [29].

The continuity equation or conservation of mass equation can be written as

$$\frac{\partial \rho}{\partial t} + \nabla \cdot (\rho U) = 0. \tag{10}$$

Using equation (9) for U this becomes

$$\frac{\partial \rho}{\partial t} + u\frac{\partial \rho}{\partial r} + \frac{\rho}{r^2}\frac{\partial}{\partial r}\left(r^2 u\right) = 0, \tag{11}$$

where r is the radial coordinate measured from the center of the bubble. The equation of motion or conservation of linear momentum equation known as the Navier-Stokes equation can be written as

$$\rho\frac{DU}{Dt} = -\nabla P + \mu\nabla^2 U, \tag{12}$$

$$u = R^2\dot{R}/r^2. \tag{3}$$

Substituting equation (3) into (2) and integrating results in the kinetic energy given by

$$K = 2\pi\rho R^3\dot{R}^2. \tag{4}$$

The power J can be defined by

$$J = \underline{F} \cdot \underline{u}, \tag{5}$$

where $\underline{F}$ is the force which equals pressure times area and $\underline{u}$ is the velocity of the fluid. Since the force and velocity are both radially directed and antiparallel, the power at infinity becomes

$$J = \lim_{r\to\infty} \left[-P\right]\left[4\pi r^2 u\right]. \tag{6}$$

Substituting equation (3) for u and recalling that the pressure at infinity is P_o we get

$$J = -P_o \, 4\pi R^2\dot{R}. \tag{7}$$

The time derivative of the kinetic energy (4) is given by

$$J = 2\pi\rho(3R^2\dot{R}^3 + 2R^3\dot{R}\ddot{R}). \tag{8}$$

Equating the power (7) with the time derivative of the kinetic energy (8) results in the Rayleigh equation

$$R\ddot{R} + \frac{3}{2}\dot{R}^2 = -P_o/\rho. \tag{1}$$

Chapter 1

Theoretical development

A. The acoustic cavitation equations

Before discussing the derivation of the acoustic cavitation equations, let us first recall the method of obtaining the Rayleigh equation [3]

$$R\ddot{R} + \frac{3}{2}\dot{R}^2 = -P_o/\rho. \tag{1}$$

Here, R, P_o, and ρ denote the bubble radius, pressure at infinity, and density of the liquid respectively. Dots denote differentiation with respect to time. It is assumed that the liquid is inviscid, incompressible, and has no surface tension; also the internal pressure is assumed to be zero.

Following the method of Batchelor [23], the time rate of change of kinetic energy of the fluid is assumed to be equal to the power developed at infinity. The kinetic energy of the fluid is defined by

$$K = \int_R^\infty \tfrac{1}{2}\rho\, 4\pi r^2 u^2\, dr, \tag{2}$$

where u is the magnitude of the fluid velocity. The continuity equation together with the above assumptions imply that the magnitude of the velocity can be written as

The temperature profiies will prove very helpful in determining what type of damage could be caused by therapeutic and diagnostic ultrasound instruments.

The results in chapter 4 are separated from those in chapter 3 because they come from a completely different approach to understanding how the model behaves under certain initial conditions. The system of equations describing the bubble motion is viewed as a dynamical system. In analyzing the dynamical system some of the recent techniques such as those by Ott [20], Huberman and Crutchfield [21], and Grebogi, Ott, and Yorke [22] are employed. This analysis will show that the type of damping used in the equations dramatically alters the results of these techniques.

Finally, in chapter 5 some general conclusions are drawn from the information compiled and suggestions are made as to what direction new research should follow. Ideas for both new experimental work, not discussed in previous chapters, and improvements in the theoretical model will be presented.

fundamental equations of acoustic cavitation, the internal pressure is then considered. The method of Prosperetti [10] will be employed in developing the theory used to solve for the internal pressure. Chapter 1 concludes with a brief error analysis for all the terms discarded in the conservation equations, which are used to solve for the internal pressure.

Chapter 2 deals with the numerical solution of the system of acoustic cavitation equations that is derived in chapter 1. The first step is to find the dimensionless form of all the equations that will be used in computer programs. Next, the numerical techniques used to solve this coupled system of nonlinear ordinary and partial differential equations along with the finite difference representation of the equations are described in detail. A brief error analysis for the numerical methods used concludes this chapter.

Chapter 3 contains results not previously known and comparisons between the new results and those of previous theories. In particular, radius verses time curves for several models and frequency response curves such as those by Cramer [17] and Lauterborn and Suchla [18] are compared to the new theory. A good test to determine how well the theory estimates the damping is to compare theoretical levitation number curves with the experimental ones obtained by Crum and Prosperetti [19]. Chapter 3 concludes with a discussion of the internal thermodynamics of bubbles. Both temperature profiles and pressure curves are presented as a function of radius or time for a variety of initial conditions.

$$U = \frac{1}{\gamma P}\left[(\gamma-1)K\frac{\partial T}{\partial r} - \frac{1}{3}r\dot{P}\right]. \tag{46}$$

Using the boundary conditions (36) and evaluating equation (46) at $r = R$ gives the following ordinary differential equation for $\dot{P}$

$$\dot{P} = \frac{3}{R}\left[(\gamma-1)K(T_\infty)\left(\frac{\partial T}{\partial r}\right)\bigg|_R - \gamma P\dot{R}\right]. \tag{47}$$

With the approximation of uniform pressure, equation (47) contains all of the information present in the continuity equation. Having already simplified two of the three original partial differential equations, we turn our attention once again to the energy equation. Using the ideal gas assumption, equation (40) becomes

$$\left(\frac{\gamma}{\gamma-1}\right)\frac{P}{T}\left[\frac{\partial T}{\partial t} + U\frac{\partial T}{\partial r}\right] - \dot{P} = \nabla \cdot (K\nabla T), \tag{48}$$

where U and dP/dt are defined by equations (46) and (47) respectively. The boundary conditions for equation (48) are continuity of temperature and heat fluxes across the bubble wall. If the liquid is cold enough so that the vapor pressure of the liquid is small compared to that of the gas (an assumption which holds at room temperature), one can assume that the temperature boundary condition is

$$T(r=R,t) = T_\infty. \tag{49}$$

This assumption greatly simplifies the solution of equation (48) and will be discussed at length in section C of this chapter.

During the collapse phase of the bubble motion, the gas temperature

can be exceedingly high. For this reason one must take into account the variation of the thermal conductivity K(T) for the gas in the bubble. Since the temperature of the gas is a function of both position and time, so is the conductivity. This presents a problem on the right hand side of equation (48). The standard technique for dealing with this difficulty is to define a new variable τ as an integral of the conductivity over appropriate limits such as

$$\tau = \int_{T_\infty}^{T} K(x)\,dx. \tag{50}$$

Another standard change of variables to simplify equation (48) is to define a fixed boundary rather than a varying one by introducing the new radial coordinate

$$y = r / R(t). \tag{51}$$

Using equations (46), (50), and (51) along with some algebraic manipulations one can write equation (48) as

$$\frac{\partial \tau}{\partial t} + \left[\frac{\gamma-1}{\gamma PR^2}\right]\left(\frac{\partial \tau}{\partial y} - y\frac{\partial \tau}{\partial y}\Big|_1\right)\frac{\partial \tau}{\partial y} - D\dot{P} = \frac{D}{R^2}\nabla^2\tau, \tag{52}$$

where the Laplacian is with respect to y and D(P,t) is defined by

$$D(P,t) = \frac{K(T)}{c_p \rho(P,T)} = \left[\frac{\gamma-1}{\gamma}\right]\frac{K(T)T}{P}, \tag{53}$$

which is the form of the thermal diffusivity for an ideal gas. The boundary conditions for τ are given by

$$\tau(y=1,t) = 0. \tag{54}$$

The substitutions (50) and (51) are also made in equations (46) and

(47). The new forms of these two equations add nothing to the theory
and will be omitted here. They can be found in chapter 2, section A.

All of the equations necessary to solve for the bubble's radius as
a function of time using the new model for the internal pressure have
now been derived. Because of the techniques employed, one also gets
$P(t)$ and $T(r,t)$ as well as $R(t)$. The temperature information will prove
to be very important in some practical problems discussed later.

The method of solution of these equations is simple in principle.
The Rayleigh-Plesset equation (25) or an appropriate equation containing
the compressibility terms (26) is coupled to the energy equation (52),
the pressure equation (47), and $U = dR/dt$. One can solve this system of
differential equations for the radius, pressure, velocity, and
temperature as a function of time by using numerical methods. The exact
method of solution is discussed in detail in chapter 2 section B.

C.   Limitations of the exact formulation

In numerical modeling of physical problems, there is usually a compromise between the degree of accuracy desired and the amount of computer power available to do the analysis. As the accuracy of the equations is increased by adding smaller and smaller physical effects, it sometimes happens that a set of equations is arrived at that is too complicated to solve. Without the aforementioned approximations for the internal pressure of a cavitation bubble, the new model would have this problem. However, enough information has been included in the equations to give considerable improvement over previous models for the range of parameter values which are of interest. As one ventures out of this parameter range, one might hope, but should not expect the new theory to agree very closely with experimental values.

The focus of this study is to show an improved performance for the fundamental equations given in section A of this chapter. Since all of these equations assume radial oscillations, it is assumed that this is the case for the treatment of the internal pressure. Prosperetti [42] gives conditions favorable for non-spherical oscillations and the parameter values used exclude this type of behavior. Using a Levitation cell like the one used by Crum [43], one can easily detect the onset of non-spherical oscillations. This device is used for experimental measurements and one can determine if appreciable non-spherical oscillations are occurring which might cause the data to deviate from those predicted by the theory. One can conclude that any differences

between theoretical and experimental values must be due to some other approximations we have made.

In the derivation of the fundamental equations in section A of this chapter it was assumed that the bubble wall velocity is equal to the liquid velocity at $r = R$. Prosperetti [44] has shown that this is valid only if little or no mass transfer takes place across the interface. The error due to this effect is of the order of the ratio of the density of the gas in the bubble to the density of the surrounding liquid. A typical value for this ratio is 0.001 or less.

Previously, the momentum equation (35) was shown to imply that $P_i = P_i(t)$. This required the assumption that all of the terms in the momentum equation contribute to but a small spatial pressure difference in the bubble. Prosperetti [10] gives a short account for each term in equation (35). The overriding factor in keeping $\Delta P/P$ small for the terms on the left hand side of the equation is the mach number M. As long as $M < 0.1$, all of the terms on the left hand side give rise to a small value of $\Delta P/P$. The viscous stress term on the right hand side of equation (35) can be written as [29]

$$\nabla \cdot \underline{\underline{\tau}} = \mu \nabla^2 U = \mu \left[\frac{1}{r^2} \frac{\partial}{\partial r} \left(r^2 \frac{\partial U}{\partial r} \right) \right] \bigg|_{r=R} , \qquad (55)$$

where

$$U = \dot{R}r/R. \qquad (56)$$

Substitution of (56) into (55) gives

$$\nabla \cdot \underline{\underline{\tau}} = \frac{2\mu\dot{R}}{R^2} . \qquad (57)$$

Prosperetti [10] has shown that the contribution of equation (57) to the pressure gradient in the bubble is approximately $2\mu\dot{R}/PR$. Assuming that the viscosity of air at room temperature is approximately 1.8×10^{-4} Poise, a bubble radius of 50 microns, and a pressure of 1 atmosphere, one obtains a value for $\Delta P/P$ of approximately 0.001.

The small value of the viscosity of air also allows us to neglect the viscous heating term in the the energy equation (40). The form of this term is given in reference [25] as

$$\tau_{rr}\frac{\partial U_r}{\partial r} = \mu\dot{R}/R. \tag{58}$$

The internal gas has been modeled as an ideal gas in several places in the theory. This seems reasonable for the temperature and pressure ranges that are of interest. This choice is easy to justify since the largest deviations from room temperature and standard pressure are toward higher values as the bubble collapses. Callen [45] shows that at higher temperatures air behaves more like that of an ideal gas. Because of their complexity, more exact equations of state would not be easy to incorporate into the theory.

Finally we need to discuss the error introduced when the boundary condition (49) is used for the energy equation (48). As long as the vapor pressure of the liquid is small compared to that of the gas pressure, one can assume that very little vaporization and condensation takes place over one cycle. This restriction implies that there is very little heat exchanged on the boundary in the form of latent heat. The

other process by which heat is exchanged on the boundary is by conduction across the interface. Prosperetti [10] has shown that if T_c, T_s, T_∞, and K are the center temperature, surface temperature, ambient liquid temperature, and the thermal conductivity, then if the heat fluxes in each region across the interface are set equal we get

$$\frac{T_S - T_\infty}{T_c - T_s} \sim \left(\frac{K_g c_p \rho_g}{K_l c_{pl} \rho_l}\right)^{\frac{1}{2}}, \tag{59}$$

where l and g denote the liquid and gas regions respectively. A typical value for the right hand side of (59) is 0.001. This implies that T_s is approximately equal to T_∞ as was assumed in the boundary condition (49).

When the liquid temperature is high enough so that evaporation and condensation are important, one must be careful in applying this approximation. Prosperetti [10] gives a thorough discussion of this problem. For the liquid temperatures that are of interest, however, this does not present a problem.

Because of the complexity of the conservation equations and the many approximations that have been made, one might ask if it is really worth all the trouble to solve for P_i in this manner. It will become evident in chapter 3 that the extra work involved here pays handsome dividends in terms of a theoretical model which more closely approximates experimental observations. In chapter 3 the theories will be compared to each other as well as to experimental results.

Chapter 2

Numerical solution of the equations

A. Dimensionless form of the equations

Perhaps the first step in solving a system of differential equations numerically is finding a dimensionless form of the equations [46]. In many cases a dimensionless form of the equations is much more stable from a numerical point of view. It is also much easier to compare the accuracy of different numerical methods if the equations are in a dimensionless form. Before describing the nondimensionalization procedure, let us first recall the four equations in the new system with the change of variables given by equations (50) and (51)

$$\left(1 - \frac{\dot{R}}{c}\right)R\ddot{R} + \frac{3}{2}\dot{R}^2\left(1 - \frac{\dot{R}}{3c}\right) = \left(1 + \frac{\dot{R}}{c}\right)\frac{P(R,t) - P_S(t+R/c)}{\rho} + \frac{R}{\rho c}\frac{dP(R,t)}{dt} \quad , \quad (26)$$

$$\frac{\partial \tau}{\partial t} + \left(\frac{\gamma-1}{\gamma PR^2}\right)\left(\frac{\partial \tau}{\partial y} - y\frac{\partial \tau}{\partial y}\Big|_1\right)\frac{\partial \tau}{\partial y} - D\dot{P} = \frac{D}{R^2}\nabla^2\tau \quad , \quad (52)$$

$$\dot{P} = \frac{3}{R}\left(\frac{\gamma-1}{R}\left(\frac{\partial \tau}{\partial y}\right)\Big|_1 - \gamma P\dot{R}\right) \quad , \quad (60)$$

and
$$U = dR/dt. \quad (61)$$

In the definitions which follow, dimensionless quantities will be denoted with a subscript *. A suitable value for a reference length is

the equilibrium radius R_o. The internal pressure at equilibrium, P_o, which is related to R_o through equation (34), is used as the reference pressure. The reference time used is the reciprocal of the driving frequency ω and the reference temperature used is the ambient liquid temperature T_∞. These and other derived quantities are listed below for later reference

$$R = R_o R_*, \quad P = P_o P_*, \quad t = t_*/\omega,$$
$$P_\infty = P_o P_{\infty *}, \quad P_s = P_o P_{s*}, \quad T_\infty = T_\infty T_*, \tag{62}$$
$$c = \omega R_o c_*, \quad \tau = D_o P_o \tau_*, \quad D = D_o D_*.$$

The appropriate form of the different derivatives in our system of equations is calculated next. The time derivatives of the radius are

$$\dot{R} = \omega R_o \dot{R}_* \quad \text{and} \quad \ddot{R} = \omega^2 R_o \ddot{R}_* , \tag{63}$$

where the dots over starred variables denote differentiation with respect to the dimensionless time t_*. The other derivatives necessary to complete the non-dimensionalization process are

$$\dot{P} = \omega P_o \dot{P}_*, \quad \nabla^2 \tau = D_o P_o \nabla^2 \tau_*,$$

$$\frac{\partial \tau}{\partial t} = D_o P_o \omega \frac{\partial \tau_*}{\partial t_*} , \quad \frac{\partial \tau}{\partial y} = D_o P_o \frac{\partial \tau_*}{\partial y}, \quad \text{and} \tag{64}$$

$$\left(\frac{\partial T}{\partial r}\right)\bigg|_{r=R} = \frac{D_o P_o}{R_o R_* K(T_\infty)} \left(\frac{\partial \tau_*}{\partial y}\right)\bigg|_{y=1} ,$$

where several steps have been omitted, particularly in the last

equation. An important step in obtaining the last equation is recognizing that

$$\frac{dT}{d\tau} = K(T) \tag{65}$$

by applying Leibniz' rule to equation (50) and taking the reciprocal of the result. Using the substitutions given above, the new system of equations becomes

$$(1 - M)R_* \dot{U}_* + 1.5(1 - M/3)U_*^2 = Z[(1+M)(P_* - P_{\infty*} - P_{S*}(t_* + R_*/c_*)$$
$$- W/R_* - YU_*/R_*) + R_* c_* \dot{P}_*], \tag{66a}$$

$$\frac{\partial \tau*}{\partial t_*} + \left(\frac{\gamma-1}{\gamma}\right) \chi \left(\frac{1}{P_* R_*^2}\right) \left(\frac{\partial \tau*}{\partial y} - y \frac{\partial \tau*}{\partial y}\bigg|_{y=1}\right) \frac{\partial \tau*}{\partial y} - D_* \dot{P}_* = \frac{\chi D_* \nabla^2 \tau*}{R_*^2}, \tag{66b}$$

$$\dot{P}_* = \frac{3}{R_*} \left((\gamma-1)\frac{\chi}{R_*}\left(\frac{\partial \tau*}{\partial y}\right)\bigg|_{y=1} - \gamma P_* U_*\right), \tag{66c}$$

and
$$U_* = dR_*/dt_*, \tag{66d}$$

where

$$Z = \frac{P_o}{\rho_\ell \omega^2 R_o^2}, \quad W = \frac{2\sigma}{R_o P_o}, \quad Y = \frac{4\mu_\ell \omega}{P_o},$$

$$\chi = D_o/(\omega R_o^2), \quad \text{and} \quad \nabla^2 \tau_* = \frac{\partial^2 \tau}{\partial y^2} + \frac{2\partial \tau*}{y \partial y}. \tag{67}$$

In order to calculate D_* it is necessary to find the temperature T from the integral equation (50). One can easily solve for T provided K(T) is of the form

$$K(T) = 5.528T + 1165. \tag{68}$$

Equation (68) was determined by a simple linear regression routine on the experimental data given by Weast [47] (see figure 1). This linear equation for $K(T)$ enables one to integrate equation (50) analytically and obtain a value for T from the resulting quadratic equation.

This concludes the nondimensionalization process for the system of equations. The details on how to solve these equations is the subject of the next section of this chapter.
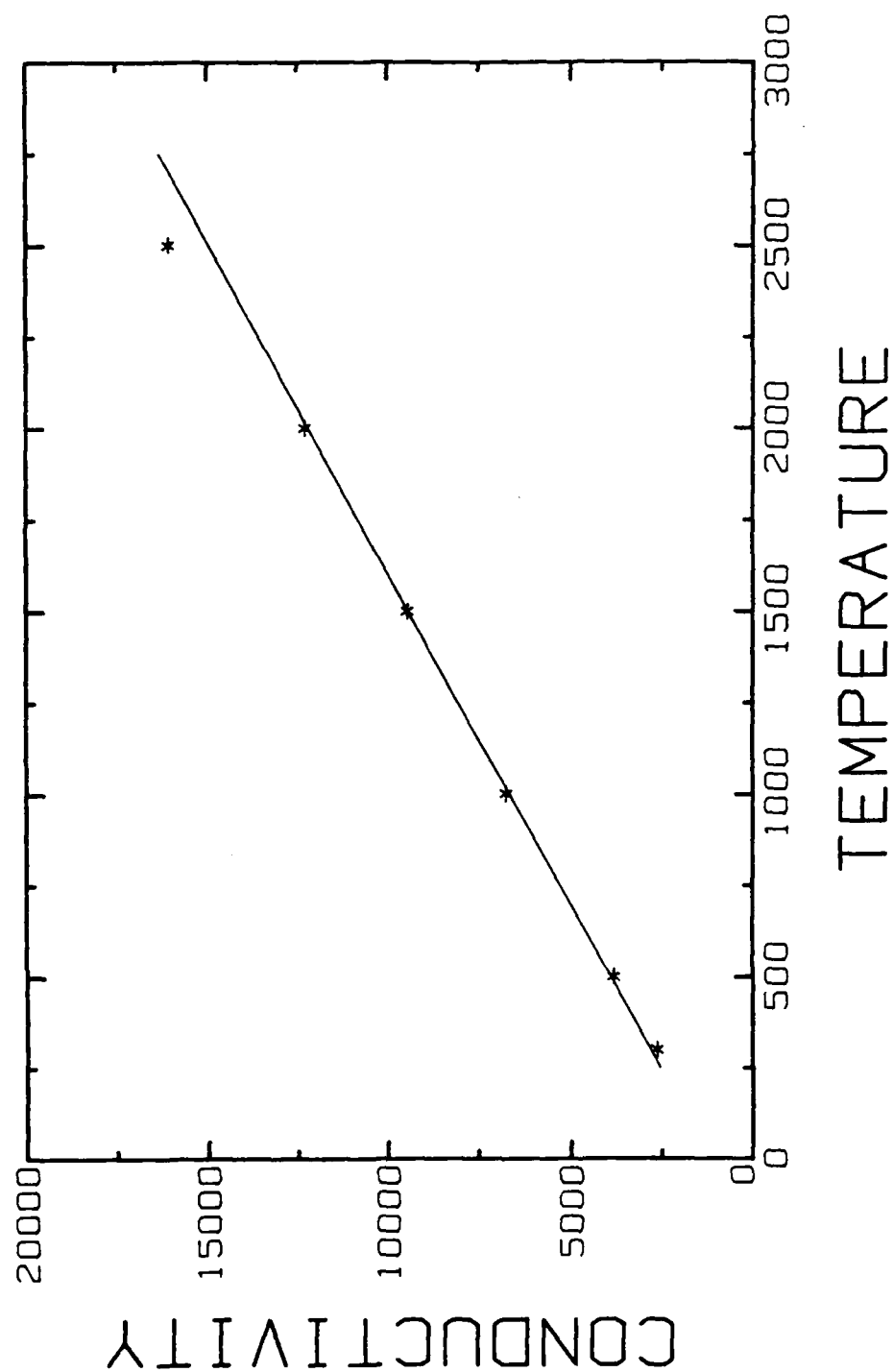
Figure 1. Thermal conductivity of air as a function of temperature. Conductivity in units of ergs/(cm·sec·°K) and temperature in degrees kelvin.

B. Finite difference equations

The system of dimensionless equations derived in section A of this chapter is now solved using numerical methods. Because of the complexity of the system and the coupling between the equations, a multistep method is used. These types of methods offer good accuracy without being as time consuming as some of the single step algorithms such as the Runge-Kutta method.

The algorithm used is as follows. A simple predictor-corrector multistep method is applied to our system of equations [50]. This technique can be illustrated by letting

$$\frac{d\underline{X}}{dt} = \underline{F}(\underline{X}).$$ (69)

The vector $\underline{X}$ denotes the quantities radius, velocity, pressure, and temperature. $\underline{F}(\underline{X})$ is the functional form of the time derivatives of the aforementioned quantities. Using finite differences one can write equation (69) as

$$\underline{X}^{n+1} = \underline{X}^{n} + \frac{\Delta t}{2}[\underline{F}(\underline{X}^{n}) + \underline{F}(\underline{X}^{n+1})].$$ (70)

However, one cannot solve this equation explicitly for $\underline{X}^{n+1}$ because of the complexity of the system of equations. The predictor-corrector scheme overcomes this problem however.

In the predictor step an approximate value for $\underline{X}^{n+1}$ is computed using an Euler method [48] of the form

$$\underline{X}^{n+1} = \underline{X}^{n} + \Delta t \underline{F}(\underline{X}^{n}).$$ (71)

This predicted value of $\underline{X}^{n+1}$ is used in equation (70) to get a more accurate value of $\underline{X}^{n+1}$. In actual practice this corrector step is repeated a second time for additional accuracy. One could repeat this process over and over, but experience has shown that two iterations is sufficient for our needs.

If one finds certain initial conditions and parameter settings which cause the corrector process to converge slowly, a more advanced predictor-corrector algorithm such as the Adams-Moulton method [48] can be used. For the conditions that are of interest, however, the simple method suffices.

Although the techniques outlined above are straightforward in principle, they are rather tedious to apply because of the complexity of the system of equations. In the remainder of this section, a step by step procedure on how to implement this method for this system of equations is discussed. Those not interested in this detailed guide to the solution of the equations are encouraged to skip to the flow chart at the end of this section without loss of continuity.

The first phase of the method is to predict new values of the variables using the Euler equation (71). For convenience the subscript * notation for dimensionless equations (66) is dropped. Predicted values will be denoted with a tilda over them. The first step is finding a predicted pressure at the n+1 time step. This requires the evaluation dP/dt at the nth time step by

$$\dot{P}^n = \frac{3}{R^n} \left[\frac{(\gamma-1)_{\dot{}}}{R^n} \left(\frac{0-\tau_N^n}{\Delta y} \right) - \gamma P^n U^n \right], \tag{72}$$

Chapter 3

Computational results

A. Radius verses time curves

Of all the information obtained from the computer programs, perhaps the simplest to understand and analyze is the radius verses time data. This information gives a numerical picture of the bubble at each time step. One can compare these radius-time curves for different models at a variety of initial conditions and make some conclusions as to where the models agree and disagree. Because some models such as the exact formulation require large amounts of computer time, it is useful to know when a simpler model gives results that are sufficiently accurate *for* one's needs. For this reason we not only show results from the new formulation but also include the results from other methods as well. One can also obtain information about the phase difference between the driving pressure and the bubble oscillations. This phase difference is related to the damping of the system in a complicated manner. Finally one can find the spectrum of the radius-time curves by a simple fourier analysis of the data. This fourier analysis of the curve shows which harmonic modes are dominant in the bubble's radiated noise signal.

In figure 5, the radius verses time curves are compared for an equilibrium radius of 50 microns, a driving pressure amplitude of 0.4 bar, and a driving frequency of 0.4 times the linear resonance

temperature of bubbles at known driving pressures and equilibrium radii. An investigation of this nature is presently under way and the results should be available shortly.

In closing we should mention that experience has shown that by examining a few cycles of the numerical solution, one can easily decide whether equation (70) is stable or unstable. For the stable solutions at high amplitudes, one must wait for new experimental results before deciding how well the new theory models a real cavitation bubble in this extreme region.

D. Applicability

In the next chapter the values given by the new equations are shown to be more accurate than the ones given by the polytropic approximation. This is shown by examining the predicted levitation numbers of each method and comparing them to experimental ones obtained by Crum and Prosperetti [19].

Unfortunately, the levitation number data is still at rather low amplitude and one cannot tell how accurate the solutions are in high amplitude regions. One possible experimental method to test the validity of the numerical solution at high amplitudes is outlined below. One could use the light-scattering technique of Hansen [51] with a very fast photo-diode and a good low noise amplifier attached. This would produce a signal that is related to the radius of the bubble by the relations given by Hansen. Once properly converted to a radius verses time signal one could compare the numerical solution at high amplitudes to this experimental one. Work on this experiment is presently under way and when completed it should provide a definitive test for all nonlinear bubble oscillation equations.

Another test for large amplitude oscillations is determining the interior bubble temperatures experimentally by observing sono-luminescence and comparing them to the numerical values. Dissociation of water molecules into hydroxyl free radicals and hydrogen starts taking place at well defined temperatures [7], which should enable experimentalists to obtain very accurate data on the interior
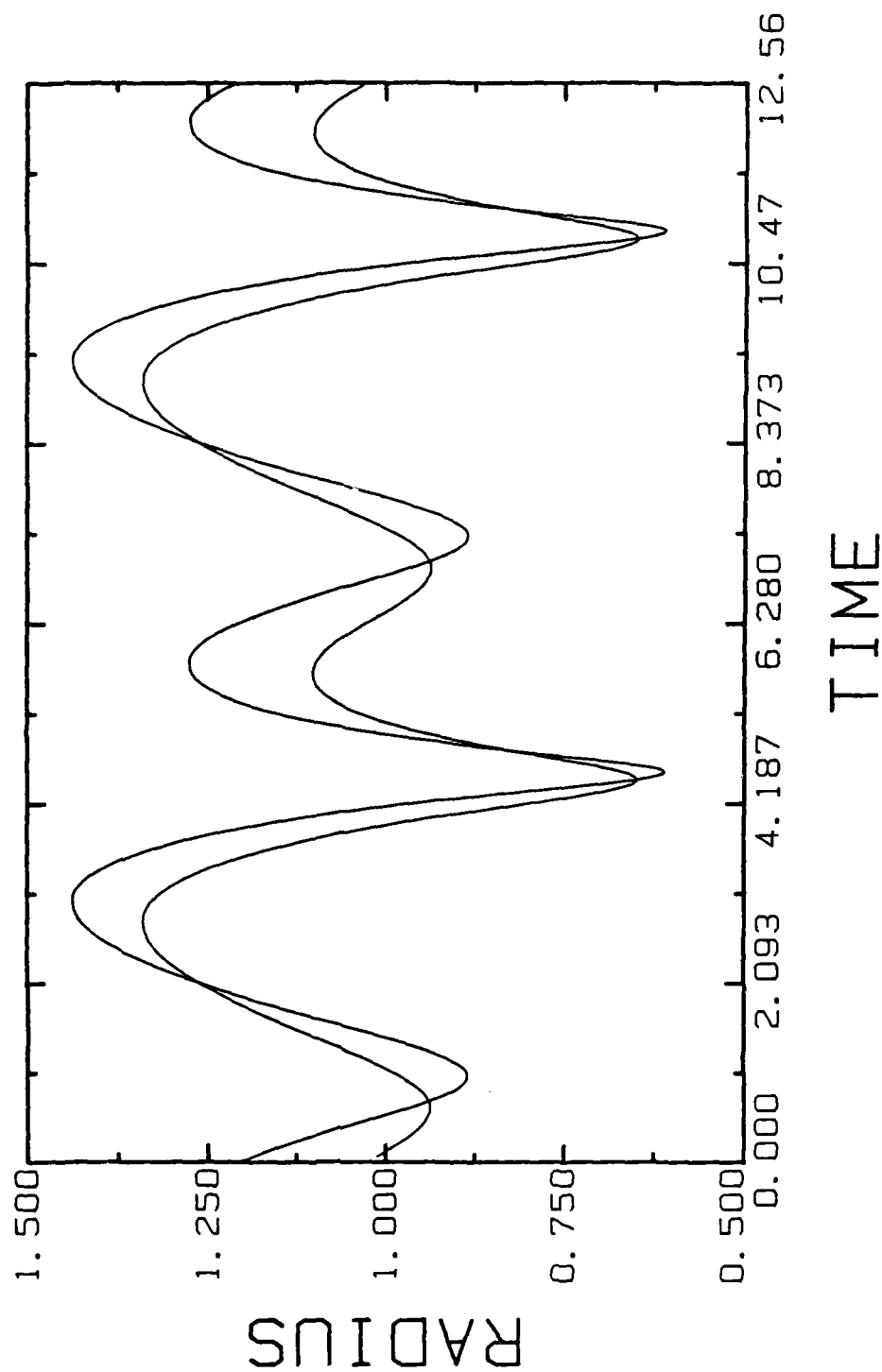
Figure 4. Normalized bubble radius as a function of time for the Rayleigh-Plesset Polytropic equation (lower amp.) and the exact formulation (higher amp.). R_o =50 microns, Pa=0.5 bar, and $\omega=\omega_o/2$.
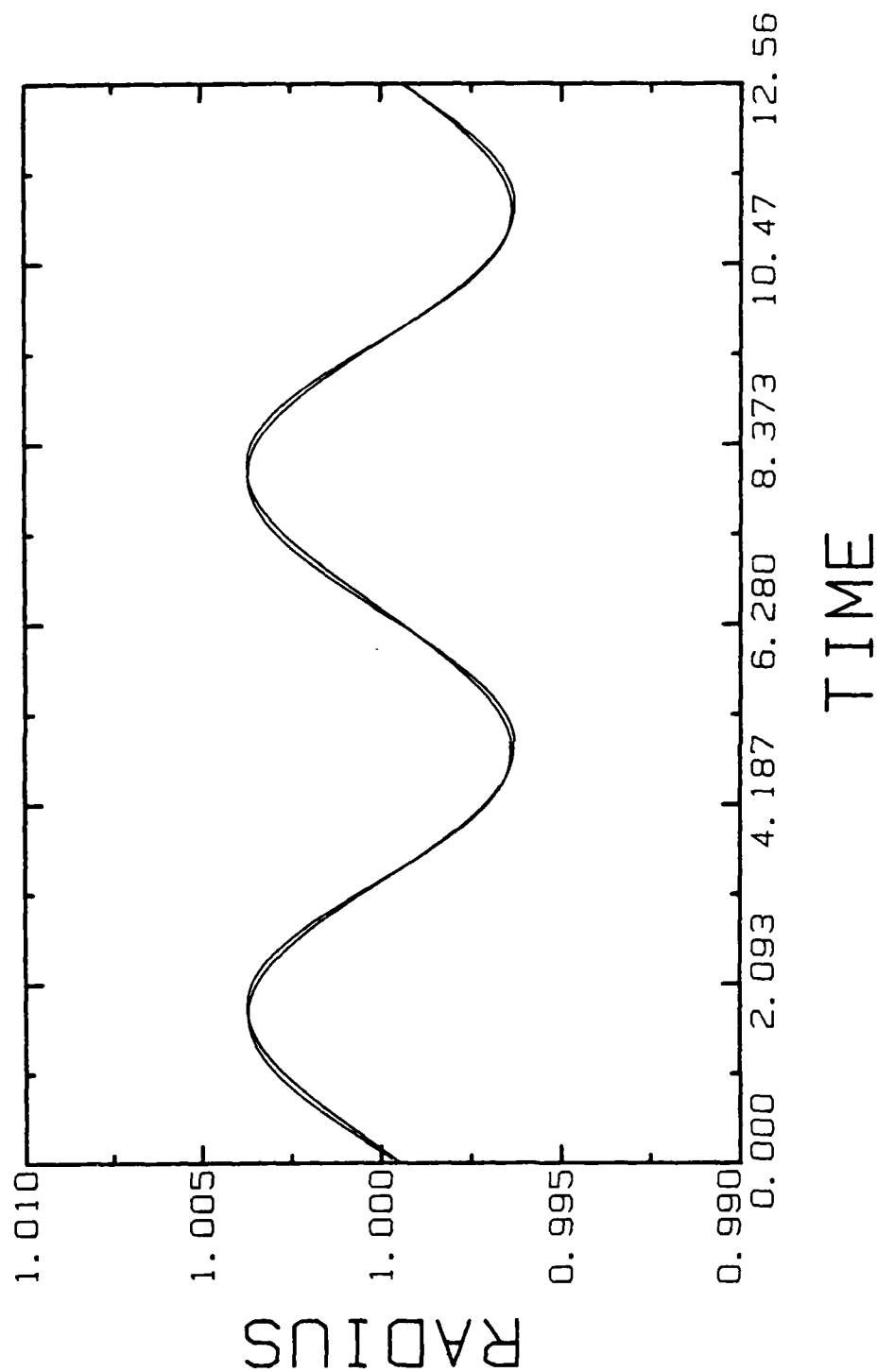
Figure 3. Normalized bubble radius as a function of time for the analytic first order solution and the new exact formulation. R_o=50 microns, Pa=0.01 bar, and $\omega=\omega_o/2$.

insight as to how well the numerical solution approximates an exact analytic solution to the system of equations if one were available. One can make several tests, however, to increase one's confidence in the method used. As a preliminary test the numerical solution for the radius as a function of time is compared to an analytical solution which uses the polytropic approximation and is valid to first order [15]. Of course this comparison can only be made at low driving amplitudes since the analytical solution is only accurate in the low amplitude limit. Figure 3 shows this comparison for a 50 micron bubble driven at half its linear resonance frequency at a pressure amplitude of 0.01 bar. The figure indicates that the numerical solution is nearly identical to the analytical one when driving amplitudes are small. This reassures us that a fundamental mistake has not been made in either deriving the system of equations or in solving them numerically.

For more moderate amplitudes, a comparison is made between the new results and numerical solutions of the Rayleigh-Plesset equation with a polytropic approximation, using a fourth order Runge-Kutta method. The program used to do this calculation was first written by A. Prosperetti. An updated version with modifications made by the author is included in appendix B. Figure 4 shows a comparison between the two models for a 50 micron bubble driven at half its linear resonance frequency and a pressure of 0.50 bar. For this case there is a small difference between the two solutions, however, they are similiar enough to reassure us that the new solution is working properly at this amplitude.

C. Error analysis

A formal error analysis of the complete system of equations in all its detail would be quite difficult. One can, however, give a more general error analysis for the basic methods used, that is, for equations (70) and (71) and the Crank-Nicolson implicit method.

The Euler method or equation (71), which is used as the predictor in the algorithm, has a local or truncation error of order $(\Delta t)^2$ and a global or cumulative error of order (Δt). Equation (70) is known as the Modified Euler method or the Euler predictor-corrector method. The truncation error of the Modified Euler method is of order $(\Delta t)^3$ and the cumulative error is of order $(\Delta t)^2$. For completeness one should also mention the Adams-Moulton method referred to in the previous section. This method has a truncation error of order $(\Delta t)^5$ and a cumulative error of order $(\Delta t)^4$, which is the same as a fourth order Runge-Kutta method.

The Crank-Nicolson method is embedded in equation (70). This method is an implicit one and because of the judicious choice of the constants multiplying the finite difference approximations, the method has a truncation error of order $(\Delta t)^2$ and $(\Delta y)^2$. Since this method is always stable, one knows that errors created at each time step must decay exponentially [48]. One of the nice features of damped driven nonlinear oscillators is that as long as the algorithms are stable the numerical solution is usually being forced toward the exact solution of the equations.

The error analysis above does not, however, give any physical
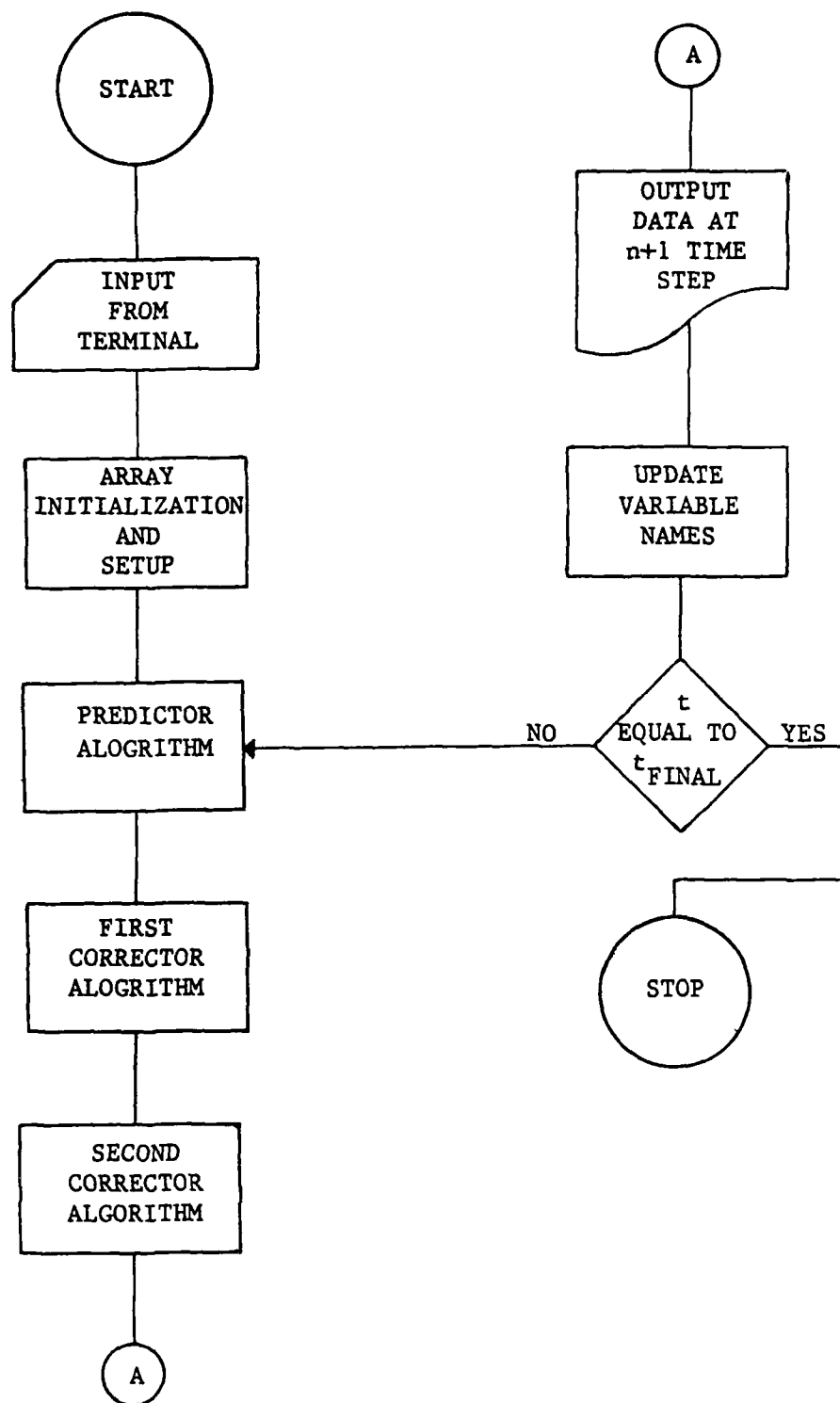
Figure 2. Flowchart for acoustic cavitation program.

(88)

Finally the corrected values for the dimensional temperature and the thermal diffusivity are found by replacing the tilda variables in equations (77) and (79) with the corrected variables denoted by carets.

In order to increase the accuracy at the new time step even more, a second correction exactly the same as the one just described is made. It is these second corrections that are used for the values at the n+1 time step. At this point in the computer program, all of the variables that are of interest are written out and then the variable names are updated. The entire process is then repeated starting at equation (72).

A listing of the computer program is provided in appendix A. Figure 2 is a flowchart for the program and provides a qualitative view of how the system of equations is solved. The error analysis for the numerical methods used is found in the next section of this chapter.

and the corrected pressure derivative from equation (66c) is given by

$$\hat{P}^{n+1} = \frac{3}{\hat{R}^{n+1}} \left[\frac{(\gamma-1)\chi}{\hat{R}^{n+1}} \left(\frac{0-\hat{\tau}_N^{n+1}}{\Delta y} \right) - \gamma \hat{P}^{n+1} \hat{U}^{n+1} \right]. \tag{88}$$

Finally the corrected values for the dimensional temperature and the thermal diffusivity are found by replacing the tilda variables in equations (77) and (79) with the corrected variables denoted by carets.

In order to increase the accuracy at the new time step even more, a second correction exactly the same as the one just described is made. It is these second corrections that are used for the values at the n+1 time step. At this point in the computer program, all of the variables that are of interest are written out and then the variable names are updated. The entire process is then repeated starting at equation (72).

A listing of the computer program is provided in appendix A. Figure 2 is a flowchart for the program and provides a qualitative view of how the system of equations is solved. The error analysis for the numerical methods used is found in the next section of this chapter.

$$- \frac{\Delta t X}{2\Delta y^2 \tilde{R}^{n+1^2}} \left\{ \frac{\gamma-1}{\gamma \tilde{P}^{n-1}} \left[\tfrac{1}{2}(\tilde{\tau}_{i+1}^{n+1} - \tilde{\tau}_{i-1}^{n+1}) + y_i \tilde{\tau}_N^{n+1} \right] + \tilde{D}_i^{n+1}(1-\Delta y/y_i) \right\} \hat{\tau}_{i-1}^{n+i}$$

$$+ \left(1 + \frac{\Delta t X \tilde{D}_i^{n+1}}{\Delta y^2 \tilde{R}^{n+1^2}} \right) \tau_i^{n+1} + \frac{\Delta t X}{2\Delta y^2 \tilde{R}^{n+1^2}} \left(\frac{\gamma-1}{\gamma \tilde{P}^{n+1}} \left[\tfrac{1}{2}(\tilde{\tau}_{i+1}^{n+1} - \tilde{\tau}_{i-1}^{n+1}) \right. \right. \tag{84}$$

$$+ Y_i \tilde{\tau}_N^{n+1}] \tilde{\tau}_N^{n+1} - \tilde{D}_i^{n+1}(1+\Delta y/y_i) \right\} \hat{\tau}_{i+1}^{n+1} = \tau_i^n + \frac{\Delta t}{2} \left(\frac{\partial \tau}{\partial t} \Big|_i^n + \tilde{D}_i \ \dot{\tilde{P}}^{n+1} \right).$$

The next step in the corrector method is finding the corrected bubble wall velocity. Again, equation (70) is applied as before. One must be careful, however, because the $\underline{F}(\underline{X}^{n+1})$ term has both predicted and corrected velocities in it. The appropriate form of equation (70), before solving for the corrected velocity explicitly, is given by

$$\hat{U}^{n+1} = U^n + \frac{\Delta t}{2} \dot{U}^n + \frac{\Delta t}{2\tilde{R}^{n+1}(1-\tilde{M})} \left(-1.5(1-\tilde{M}/3)\tilde{U}^{n+1}\hat{U}^{n+1} \right.$$

$$+ Z[(1+\tilde{M})(\tilde{P}^{n+1} - P_\infty - P_s(t^{n+1} + \tilde{R}^{n+1}/c) - \frac{W+Y\hat{U}^{n+1}}{\tilde{R}^{n+1}} + \tilde{R}^{n+1}c\dot{\tilde{P}}^{n+1}] \right). \tag{85}$$

$$+ \tilde{R}^{n+1}c\dot{\tilde{P}}^{n+1}] \bigg).$$

After equation (85) is solved for the corrected velocity explicitly, the corrected radius at the new time step is found by applying equation (70) which gives

$$\hat{R}^{n+1} = R^n + \frac{\Delta t}{2}(U^n + \hat{U}^{n+1}). \tag{86}$$

Using the corrected values of temperature, velocity, and radius one finds that the corrected pressure from equation (70) is given by

$$\dot{\hat{P}}^{n+1} = P^n + \frac{\Delta t}{2} \dot{P}^n + \frac{3\Delta t}{2\hat{R}^{n+1}} \left(\frac{(\gamma-1)X}{\hat{R}^{n+1}} \left(\frac{0-\hat{\tau}_N^{n+1}}{\Delta y} \right) - \gamma \hat{P}^{n+1} \hat{U}^{n+1} \right) \tag{87}$$

variable, one starts the corrector algorithm using the method of equation (70). The corrected variables will be denoted by a caret above them. The corrector method begins by solving for a corrected temperature array at the n+1 time step. This time, however, it is not a simple matter to solve for the new values because one must use a Crank-Nicolson method [48] to advance the temperature array in time. This is necessary because equation (70) is accurate to second order and each of the embedded algorithms must be at least this accurate or one has defeated the purpose of using equation (70). The Crank-Nicolson method is an implicit method which requires the solution of a tridiagonal system of linear equations for the corrected temperature array. In order to see this more clearly, the energy equation is written in a form with the unknowns and their coefficients on the left hand side and all known quantities on the right hand side. As before, the first node has a special form given by

$$\left(1 + \frac{3\Delta t X \tilde{D}_1^{n+1}}{\Delta y^2 \tilde{R}^{n+1^2}}\right) \hat{\tau}_1^{n+1} - \frac{3X\Delta t \tilde{D}_1^{n+1}}{\Delta y^2 \tilde{R}^{n+1^2}} \hat{\tau}_2^{n+1} = \tau_1^n + \frac{\Delta t}{2}\left(\frac{\partial \tau}{\partial t}\bigg|_1^n + \tilde{D}_1^{n+1}\tilde{P}^{n+1}\right). \quad (83)$$

The general expression for the remaining nodes from i = 2 to N is given by equation (84) below. To solve this tridiagonal system for the corrected temperatures, an algorithm by Forsythe, Malcolm, and Moler [49] was modified for speed. This algorithm is a subroutine called TRIDG in our main computer program which is listed in appendix A.

thermal diffusivity D at each node. This requires that the dimensional temperature be found first by the method mentioned in section A of this chapter. For each node the dimensional temperature is related to the dimensionless temperature by

$$\tilde{T}_i^{n+1} = \frac{1}{\alpha}\left[\sqrt{1+2\alpha(\frac{\gamma-1}{\gamma})\tilde{\tau}_i^{n+1}} - \frac{1165}{K(T_\infty)}\right],\tag{77}$$

where

$$\alpha = 5.528 T_\infty/K(T_\infty).\tag{78}$$

The predicted diffusivity at node i is given by

$$\tilde{D}_i^{n+1} + (\alpha\tilde{T}_i^{n+1} + 1165/K(T_\infty))\tilde{T}_i^{n+1}/\tilde{P}^{n+1}.\tag{79}$$

We can now return to finding new values for the main variables. A predicted value for the radius is obtained from

$$\tilde{R}^{n+1} = R^n + \Delta t U^n.\tag{80}$$

To find a predicted velocity, one first solves equation (66a) for dU/dt and evaluates it at the nth time step. After evaluating this derivative, the predicted velocity is found from the Euler formula by

$$\tilde{U}^{n+1} = U^n + \Delta t\dot{U}^n.\tag{81}$$

The predictor section is concluded once a new value of dP/dt is found by

$$\tilde{P}^{n+1} = \frac{3}{\tilde{R}^{n+1}}\left[\frac{(\gamma-1)\chi}{\tilde{R}^{n+1}}\left(\frac{0-\tilde{\tau}_N^{n+1}}{\Delta y}\right) - \gamma\tilde{P}^{n+1}\tilde{U}^{n+1}\right].\tag{82}$$

Having found a predicted value at the new time step for each

where subscripts denote the node or spatial position and superscripts denote the time step. Using Euler's method one finds the predicted pressure is given by

$$\tilde{P}^{n+1} = P^n + \Delta t \dot{P}^n. \tag{73}$$

The next step involves the temperature array in the bubble. First one has to find the temperature derivatives with respect to time at each node in the bubble. The r=0 node is a special case since the Laplacian operator is different in the limit as r approaches 0 than at any nonzero value of r [46]. The center node or i=1 node is found by

$$\frac{\partial \tau}{\partial t}\bigg|_1^n = D_1^n \left(\frac{6\chi}{R^{n^2}}\left(\frac{\tau_2^n - \tau_1^n}{\Delta y^2}\right) + \dot{P}^n\right). \tag{74}$$

The general equation for the remaining nodes from i=2 to N (N+1 is the bubble wall which was assumed to be at constant ambient temperature) is given by

$$\frac{\partial \tau}{\partial t}\bigg|_i^n = D_i^n \left(\frac{\chi}{\Delta y^2 R^{n^2}}\left(\left(1 + \frac{\Delta y}{y_i}\right)\tau_{i+1}^n - 2\tau_i^n + \left(1 - \frac{\Delta y}{y_i}\right)\tau_{i-1}^n\right)\right.$$

$$\left. + \dot{P}^n\right) - \left(\frac{\gamma-1}{\gamma}\right)\frac{\chi}{P^n R^{n^2}}\left(\frac{\tau_{i+1}^n - \tau_{i-1}^n}{2\Delta y} - y_i \frac{0 - \tau_N^n}{\Delta y}\right)\left(\frac{\tau_{i+1}^n - \tau_{i-1}^n}{2\Delta y}\right). \tag{75}$$

Again using the Euler method one finds predicted temperatures at the new time step n+1 by

$$\tilde{\tau}^{n+1} = \tau_i^n + \Delta t \frac{\partial \tau}{\partial t}\bigg|_i^n. \tag{76}$$

At this point it is appropriate to find predicted values of the

frequency. The Rayleigh-Plesset Polytropic equation is denoted by RPP, the Rayleigh-Plesset Exact pressure formulation by RPE, and the Compressible Exact pressure system of equations by CE. The heavy curve in figure 5 represents the RPE and CE methods which are practicably identical. The compressible equation is only necessary when the driving pressure amplitude is very large and collapse velocities are very high. It takes only a small amount of extra computer time to use the compressible equation in the exact formulation, so we will use the CE method and omit from further discussion the RPE method.

Next, a comparison is made between the solutions given by the CE and RPP methods for a variety of bubble sizes, driving pressure amplitudes, and driving frequencies. Figure 6 shows results for an equilibrium radius of 50 microns, a driving pressure amplitude of 0.4 bar and a driving frequency of 0.8 times the linear resonance frequency. The CE method predicts a larger maximum value of R/R_o than does the RPP method. In figure 7 the equilibrium radius is 50 microns, the driving pressure amplitude is 0.6 bar, and the driving frequency is 0.8 times the linear resonance frequency. Again the CE method predicts a larger maximum value of R/R_o than does the RPP method. Note also the phase difference between the two curves which is easily measurable. These curves have very large amplitudes, however, and the limits of validity of the equations may have been reached or exceeded. One can only wait for new experimental data to determine just how large an amplitude can be used before appreciable error occurs in the results.

TIME

RADIUS

Figure 5. Normalized bubble radius as a function of time for the RPP, RPE, and CE methods. RPE and CE above the RPP curve. R_o=50 microns, Pa=0.4 bar, and ω=0.4ω_o.

Figure 6. Normalized bubble radius as a function of time for the RPP and CE methods. CE above RPP. R_o=50 microns, Pa=0.4 bar, and $\omega=0.8\omega_o$.

Figure 7. Normalized bubble radius as a function of time for the RPP and CE methods. CE above RPP. $R_o = 50$ microns, $Pa = 0.6$ bar, and $\omega = 0.8\omega_o$.

Next, several figures for 10 micron bubbles are examined. Figure 8 represents a 10 micron bubble with a driving pressure amplitude of 0.6 bar and a driving frequency of 0.4 times the linear resonance frequency. Again the pattern is the same as before, with the CE method showing less damping than the RPP method. One can also detect a difference in the magnitude of the second harmonic resonance by inspection of the figure (the small peaks between the larger peaks are mainly due to the second harmonic). Figure 9 concludes this set of results with an equilibrium radius of 10 microns, a driving pressure of 0.6 bar, and a driving frequency of 0.8 times the linear resonance frequency. Again one gets a larger response in the amplitude of the pulsation because the driving frequency is in the vicinity of the main resonance, whereas the curves at the 0.4 frequency are near the second harmonic. In the next section it is shown that the response due to these harmonic resonances is much less than that at the main resonance.

These figures represent only a few of the unlimited number of possible combinations of initial conditions. They do, however, give an idea of the differences in the two theories presented. With careful observation one can detect differences in the pulsation amplitude, the phase shifts between the driving pressure and the bubble response, and in the magnitude of each harmonic if a fourier analysis is carried out for the curves generated.
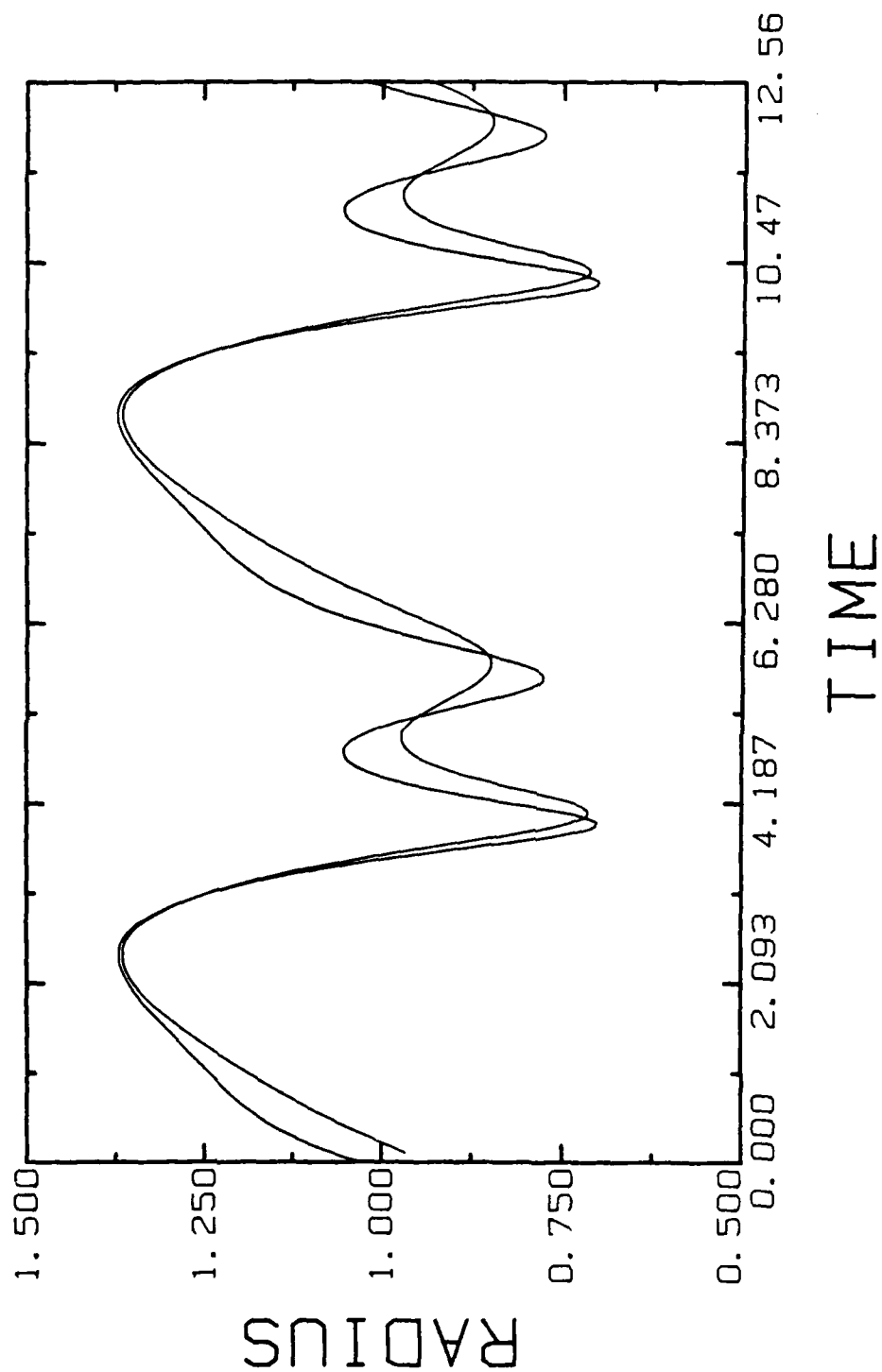
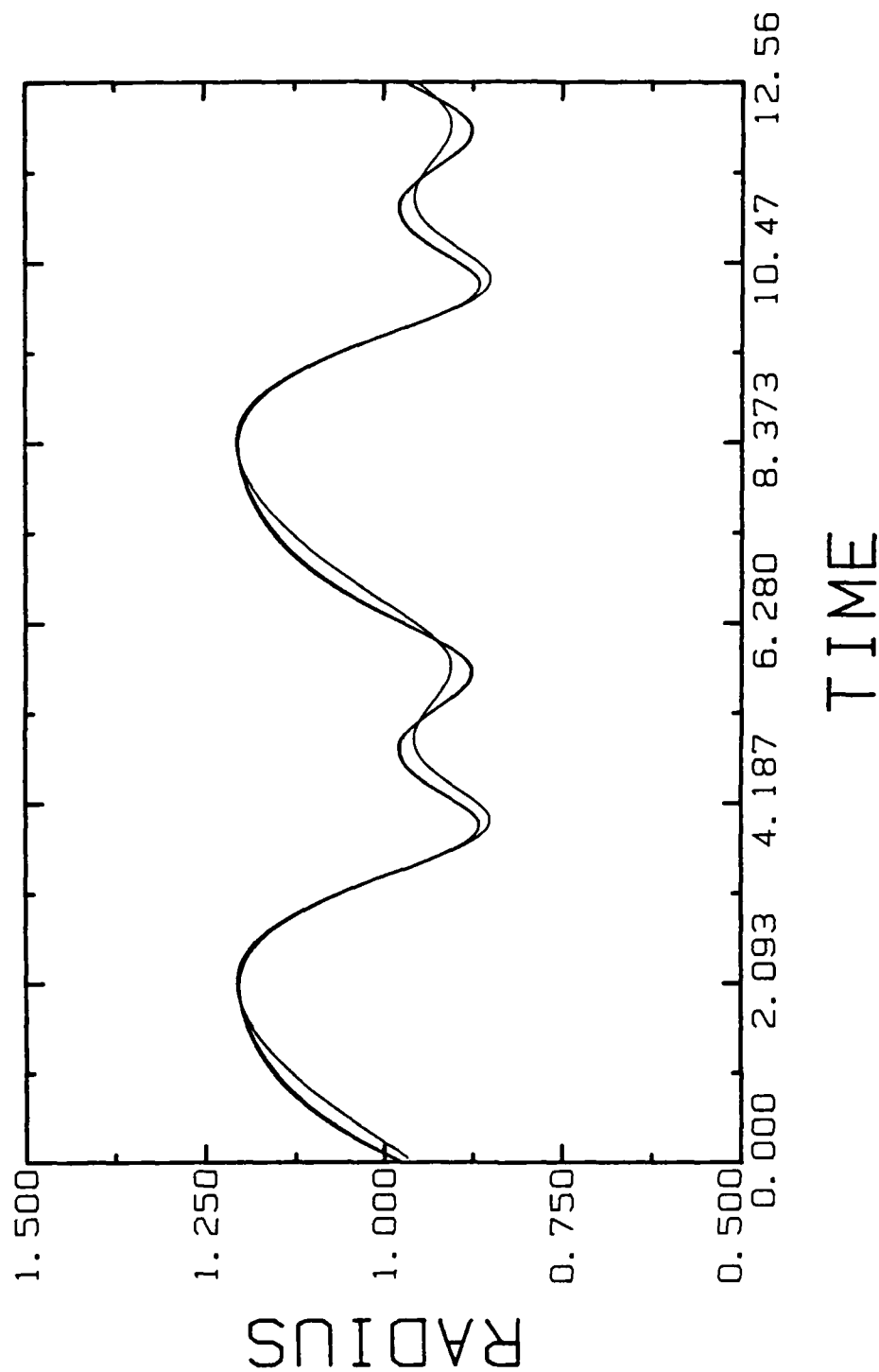Figure 8. Normalized bubble radius as a function of time for the RPP and CE methods. CE above RPP. $R_o = 10$ microns, $Pa=0.6$ bar, and $\omega=0.4\omega_o$.
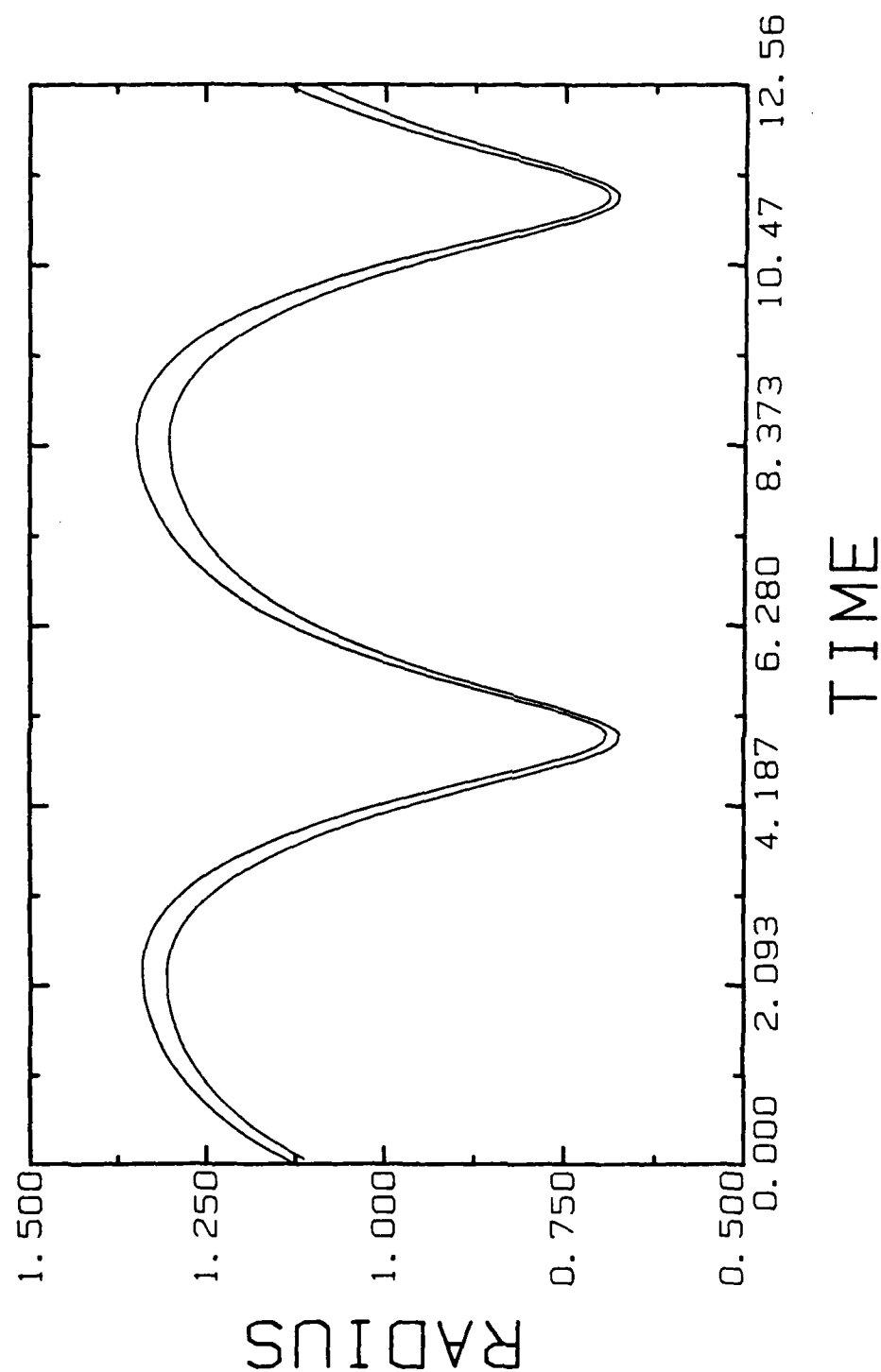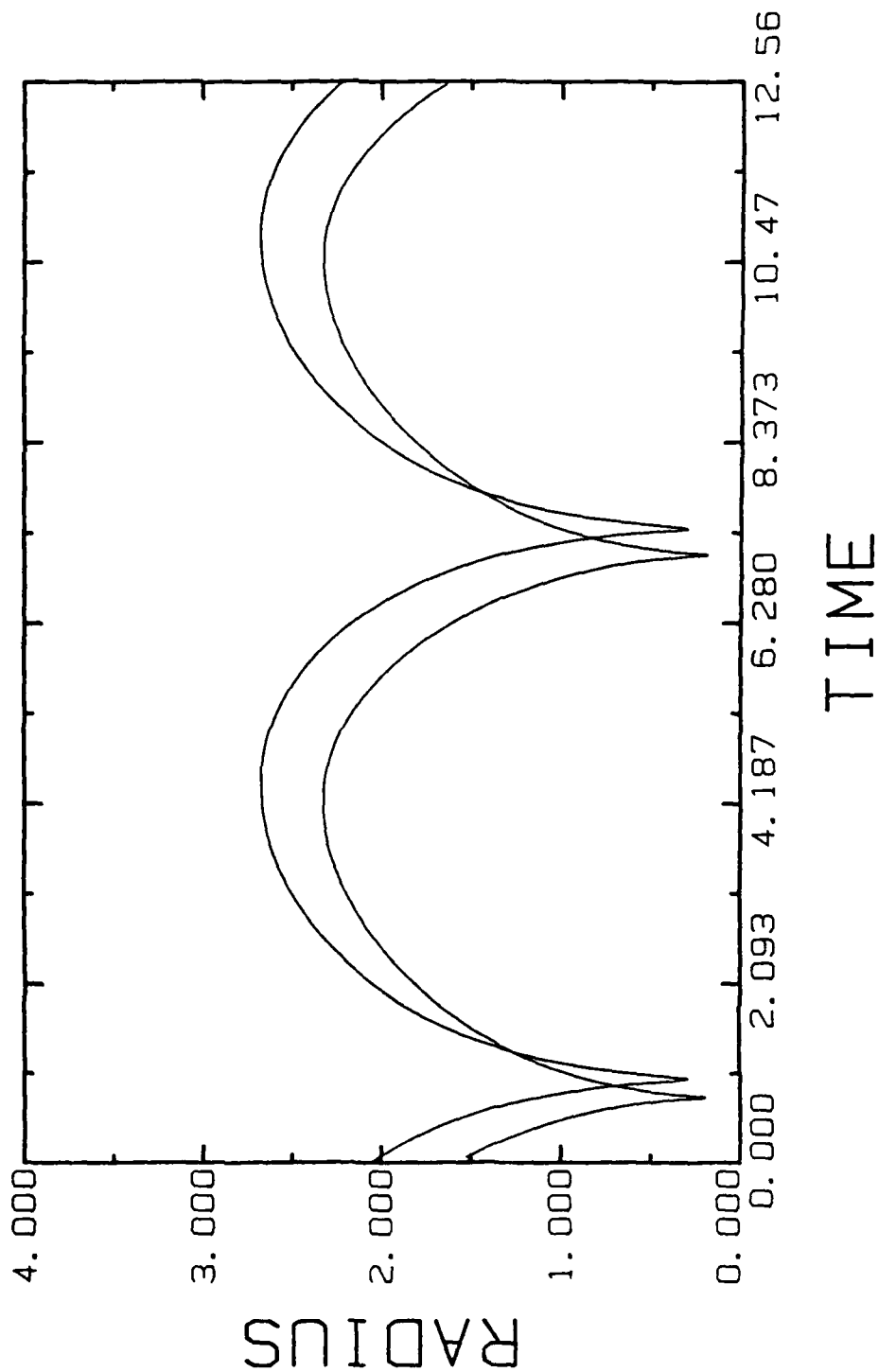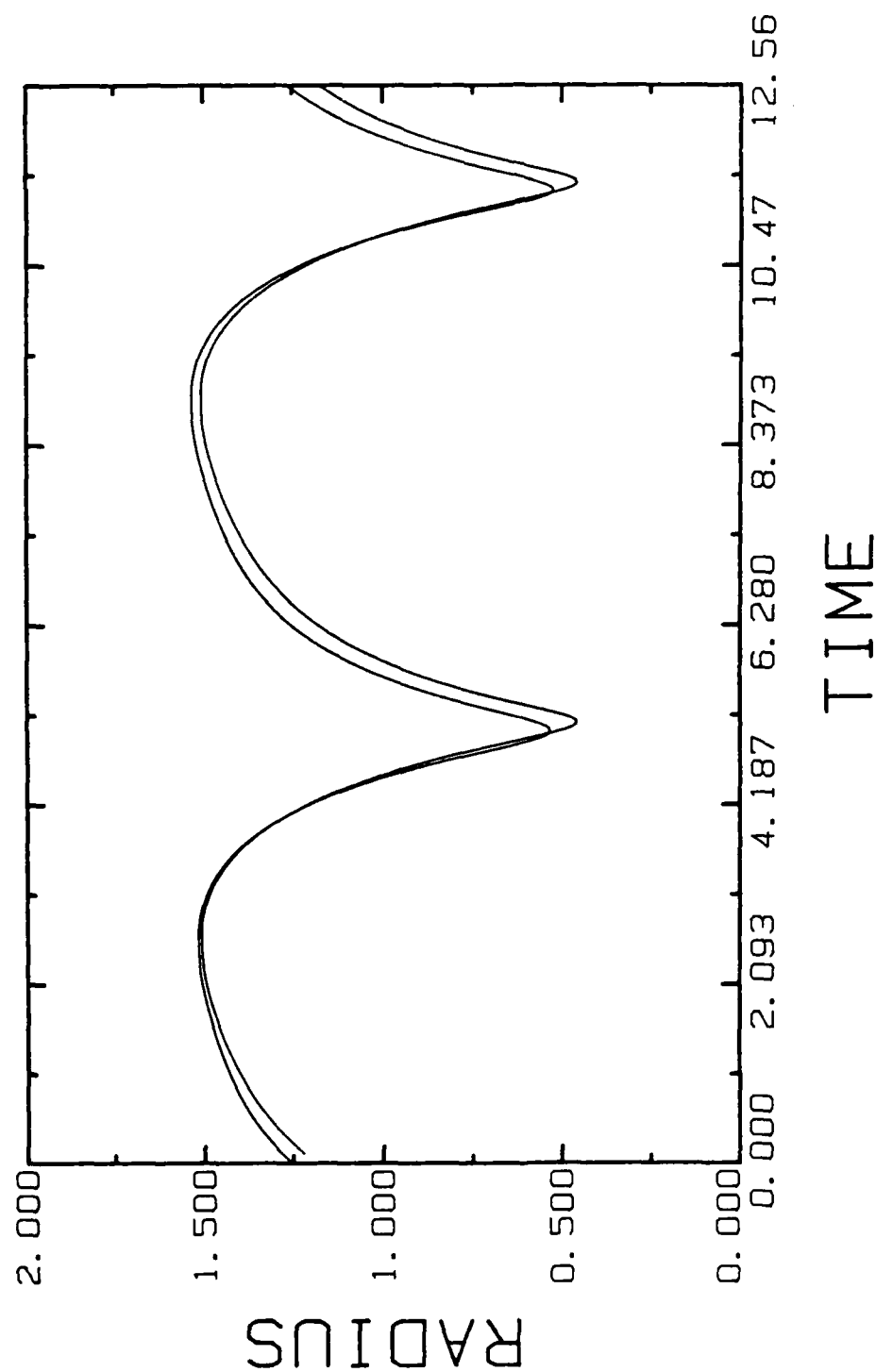
Figure 9. Normalized bubble radius as a function of time for the RPP and CE methods. CE above RPP. $R_o = 10$ microns, Pa=0.6 bar, and $\omega = 0.8 \omega_o$.

B. Frequency response curves

One of the best ways of showing how a bubble responds to a driving force under a variety of initial conditions and parameter settings is through the use of frequency response curves such as those given by Lauterborn [18,52] and Cramer [17]. These graphs show the nonlinear resonance peaks which help to characterize a bubble. This information is of interest to those examining the biological effects of ultrasound since the onset of subharmonic frequencies is often used as an indication of the presence of violent cavitation. Therefore, it is important to know precisely at what fraction of the bubble's resonance frequency that these different modes of oscillation prevail for different driving pressure amplitudes.

In the figures that follow, results are shown for a variety of conditions using the new theory. These results are compared to those by Lauterborn and Cramer to determine where the two theories agree and disagree. Figures 10-12 are frequency response curves generated by the new theory for normalized frequencies between 0.1 and 1.0. The step size used in the frequency domain is 0.01 times the resonance frequency of that particular bubble. Figure 10 shows results for a 10 micron bubble driven at 0.3, 0.5, and 0.7 bar. Figure 11 shows results for a 50 micron bubble driven at 0.2, 0.3, 0.4, and 0.5 bar. Finally figure 12 shows results for a 100 micron bubble driven from 0.1 to 0.7 bar in 0.1 bar intervals.

Each of the fourteen curves described above took approximately one

Figure 10. Maximum normalized bubble radius as a function of normalized frequency for the CE method. $R_o=10$ microns, Pa=0.3, 0.4, and 0.5 bar.
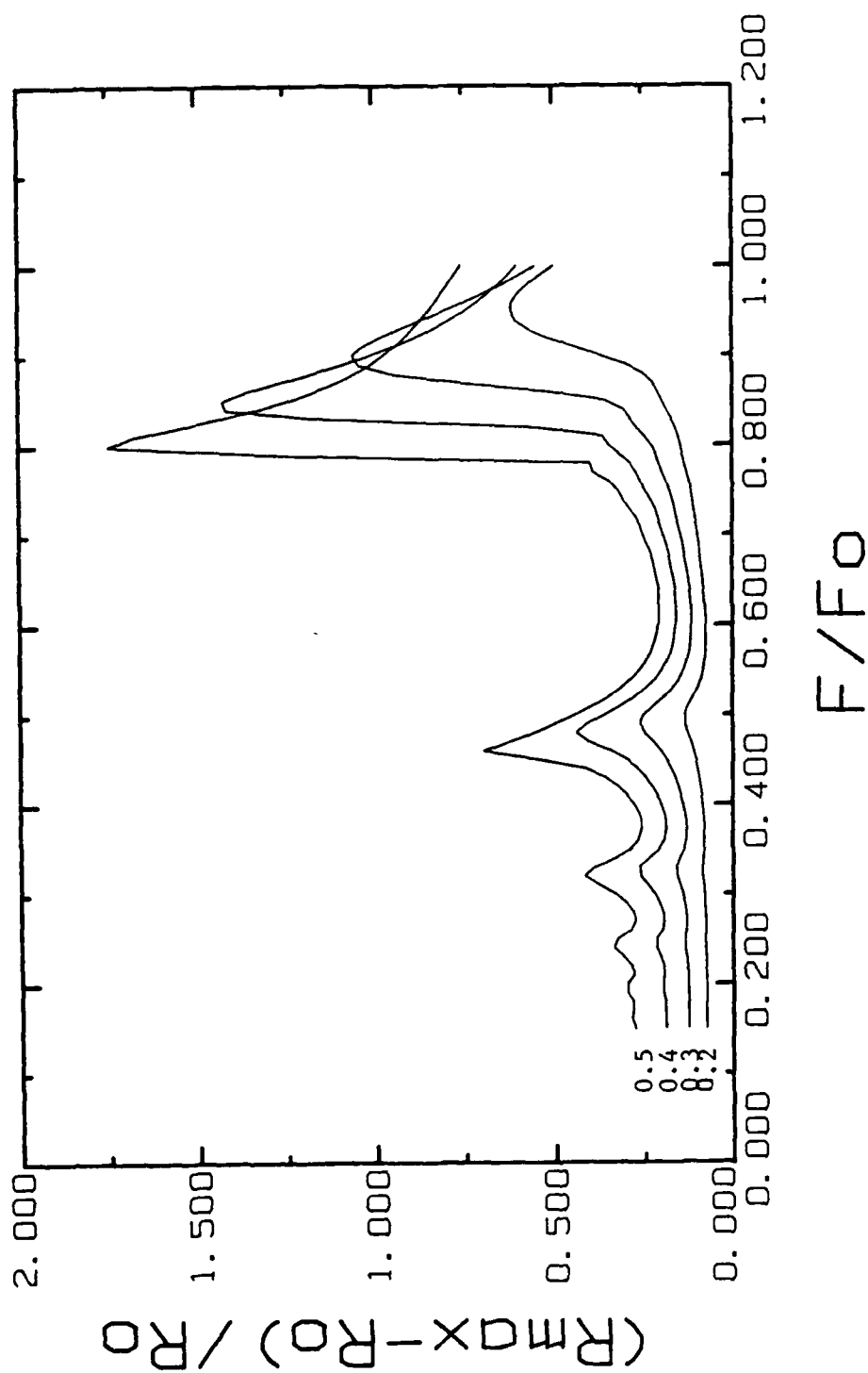
Figure 11. Maximum normalized bubble radius as a function of normalized frequency for the CE method. R_o=50 microns, Pa=0.2, 0.3, 0.4, and 0.5 bar.
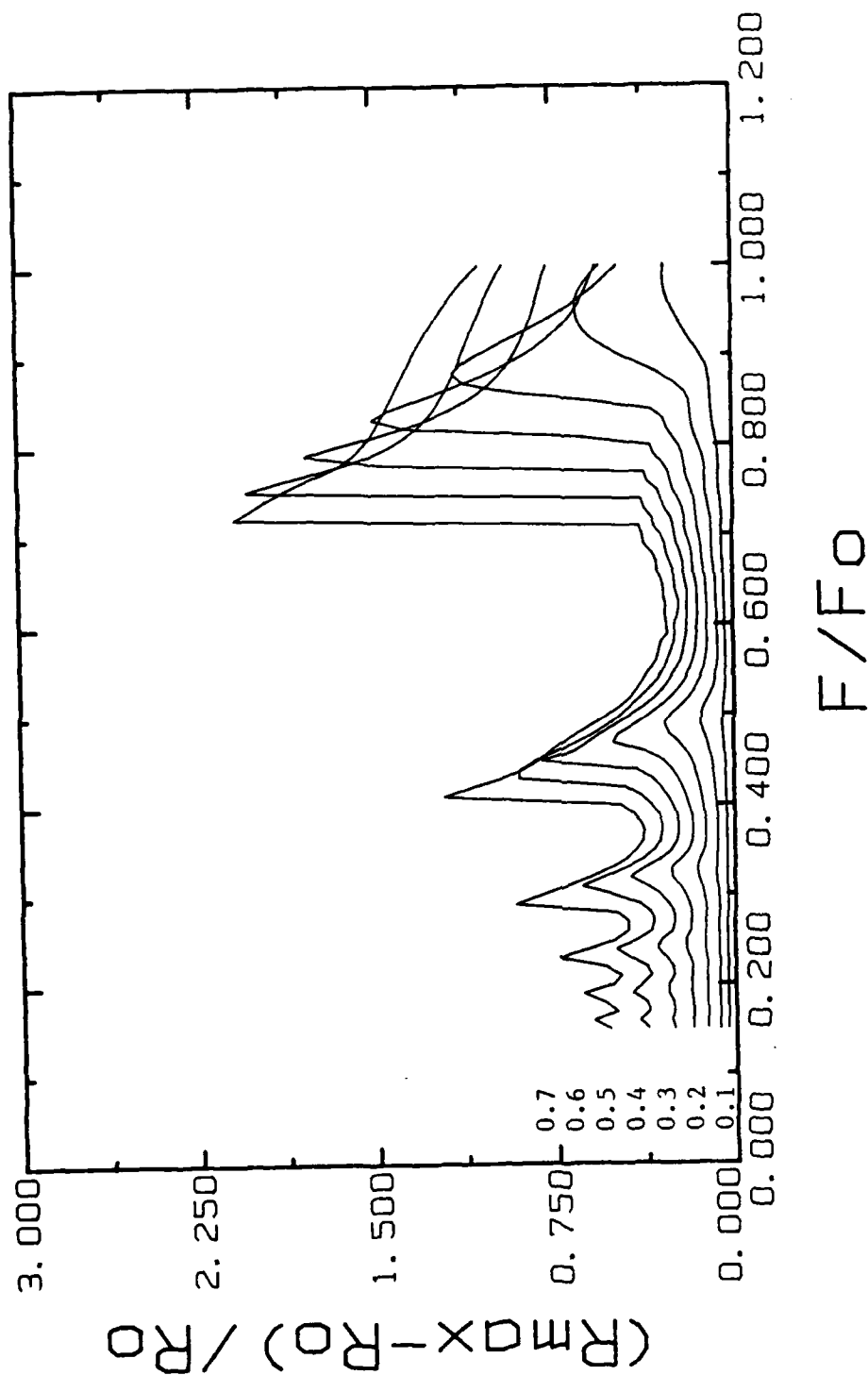
Figure 12. Maximum normalized bubble radius as a function of normalized frequency for the CE method. $R_o = 100$ microns, Pa=0.1, 0.2, 0.3, 0.4, 0.5, 0.6, and 0.7 bar.

day of cpu time on a Digital PDP 11/73 microcomputer. Of course the curves which show a large amplitude response took longer than those with small responses because of the difference in step sizes used in the time and space domains. This requirement of large amounts of computer time has somewhat limited the scope of this investigation; this point will be addressed again in chapter 4.

In figures 13 and 14 new results are compared with those by Lauterborn and Cramer. Figure 13 shows the frequency response curve for a 10 micron bubble driven at 0.7 bar. The asterisks represent points taken from the peaks of a figure by Lauterborn [52] (the value at f/f_o=1.0 is included as well). Note that there is a shift in both amplitude and frequency between the two theories. As f/f_o decreases the two theories give results that are quite close to one another. Figure 14 shows the new frequency response curve for a 100 micron bubble driven at 0.7 bar. Here the asterisks represent points taken from the peaks of a figure by Cramer [17]. Again, one sees the same trend as before, with small values of f/f_o giving even closer results than with the 10 micron bubble. These figures indicate that the new theory predicts less damping in the region around the main resonance peak and some of the subharmonic peaks as well. From the comparison to levitation number data in the next section one is inclined to believe that this new theory is more accurate. The definitive test, however, is experimental data which is not yet available.

Close examination of figure 13 and Lauterborn's figure 3 [52]
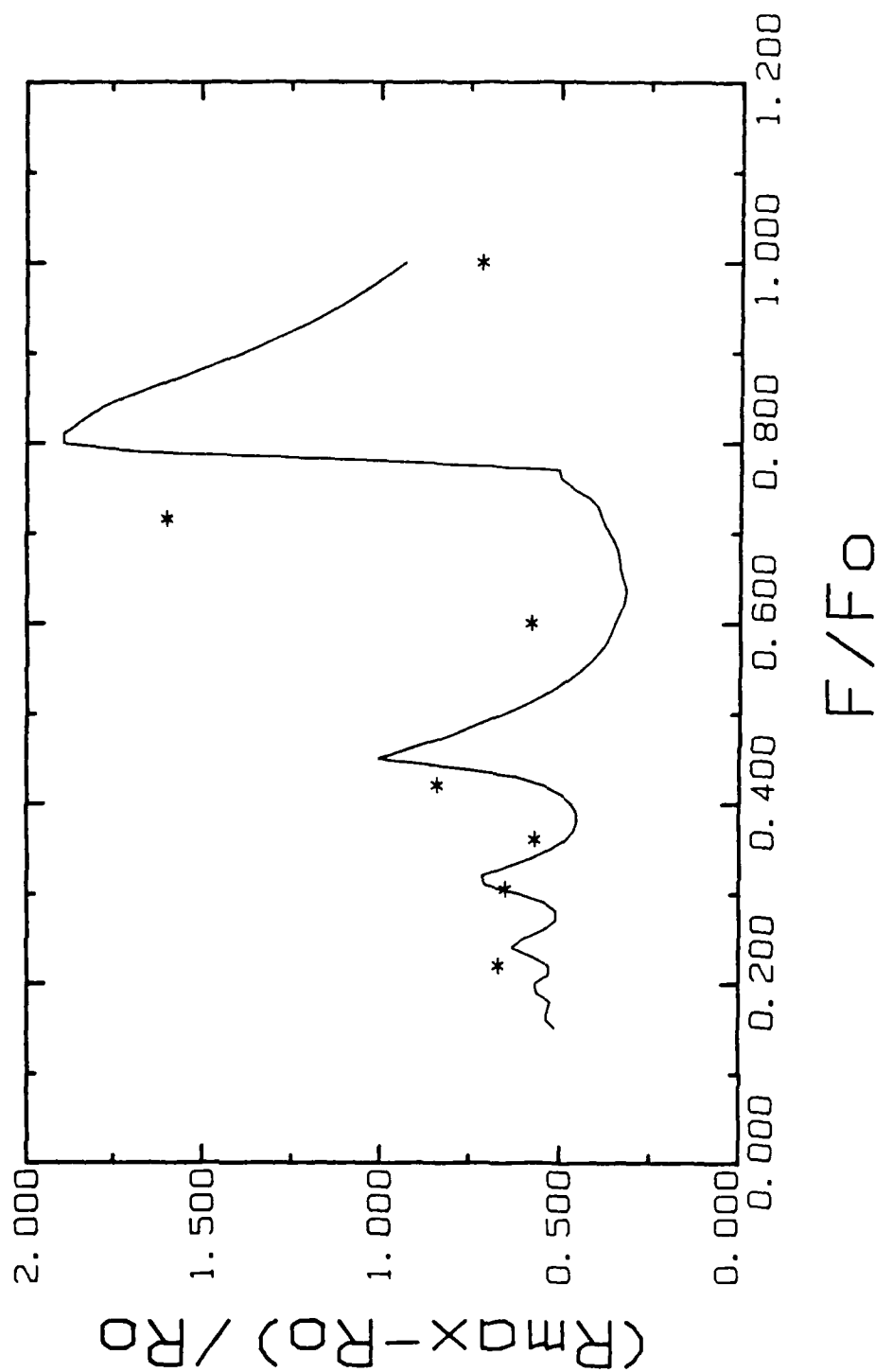
Figure 13. Maximum normalized bubble radius as a function of normalized frequency for the CE method. R_o =10 microns, Pa=0.7 bar, asterisks denote resonance peaks from a figure by Lauterborn [52].
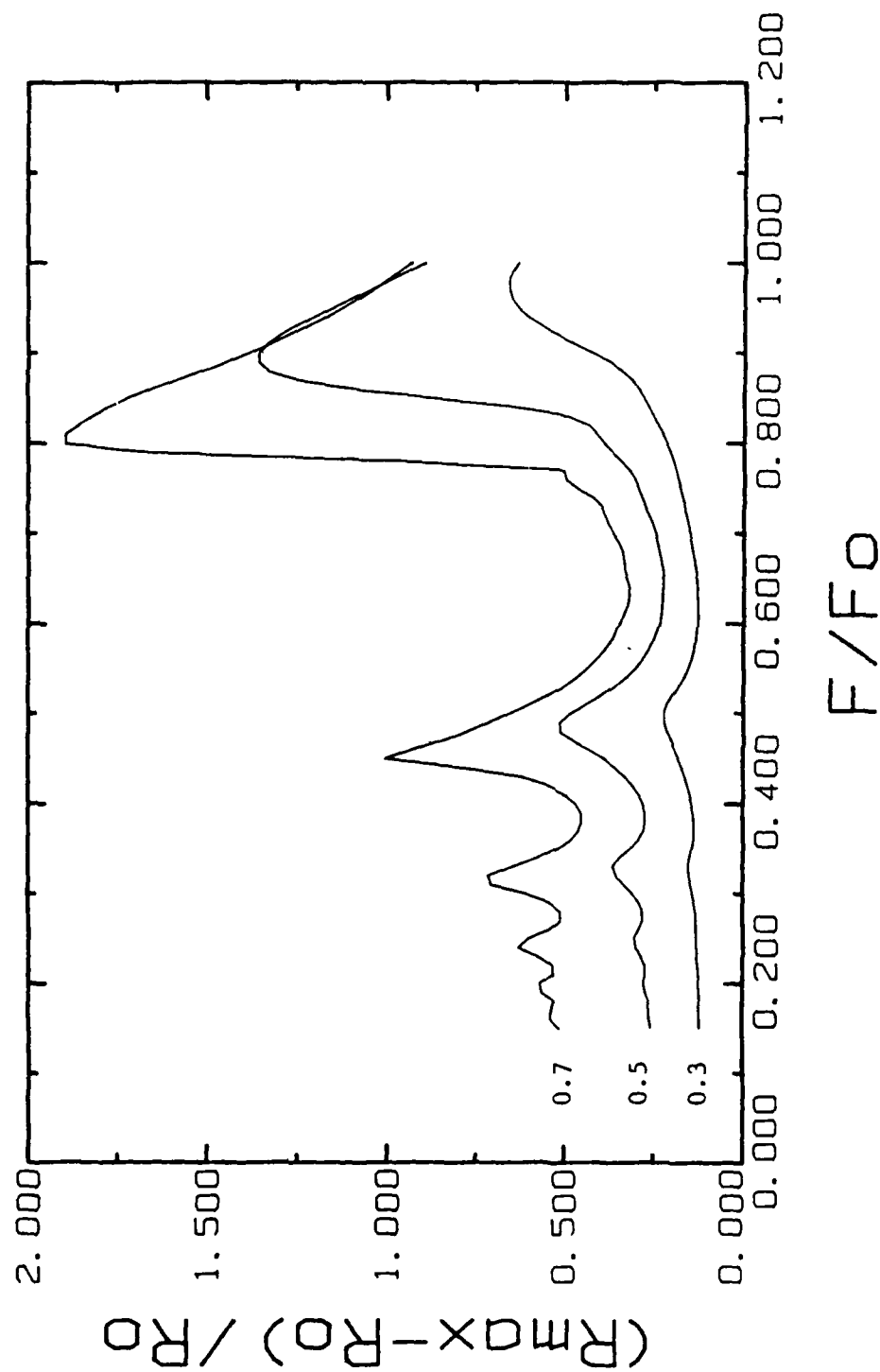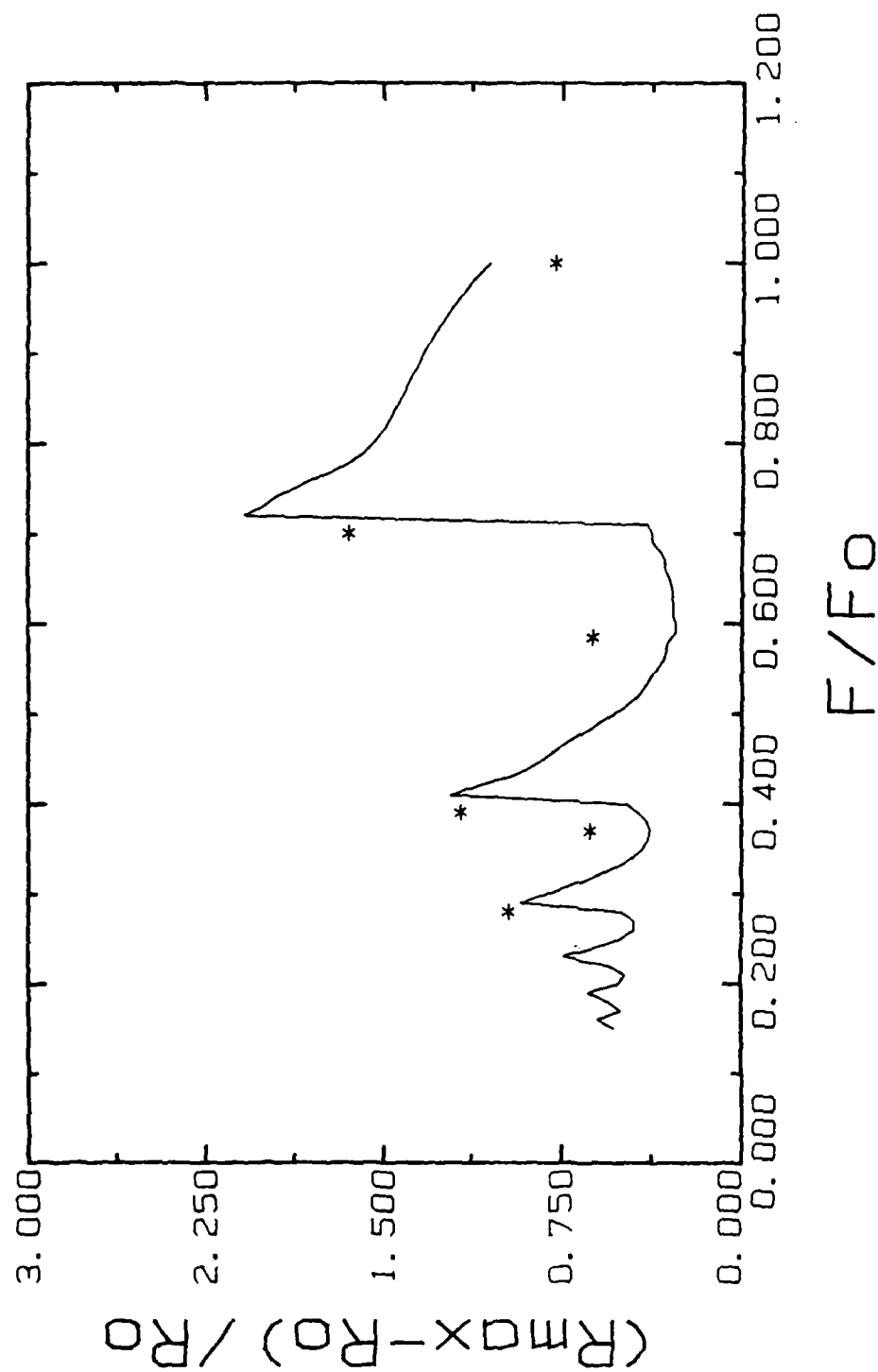
Figure 14. Maximum normalized bubble radius as a function of normalized frequency for the CE method. R_o =100 microns, Pa=0.7 bar, asterisks denote resonance peaks from a figure by Cramer [17].

the gas inside starts to increase due to heat conduction across the bubble wall. For small bubbles, the value of the radius where the minimum temperature is reached is near R_o, and for large bubbles it is near the maximum radius attained.

The figures above indicate that under the proper conditions, cavitating bubbles can produce temperatures high enough for free radical formation. This should cause some concern for those using ultrasonic instruments for medical purposes. One way to avoid this problem is to stay away from driving pressures and frequencies that cause large pulsation amplitudes. To avoid these regions, one must first know the size of the bubbles in the system of interest. This, however, is a difficult problem in itself and will not be addressed further.

Next, the center temperature of a bubble is examined as a function of time to see how long it maintains these high temperatures. Figures 22-24 show center temperatures as a function of time for 1, 10, and 100 micron bubbles driven at 0.4 and 0.8 times the linear resonance frequency of the particular bubble. Each figure indicates that high temperatures occur only for a short period of time while the bubble is near its minimum size. Figure 22 shows a 1 micron bubble driven at 1.4 bar, figure 23 a 10 micron bubble driven at 0.6 bar, and figure 24 a 100 micron bubble driven at 0.45 bar. The pulsation amplitude for the 10 micron bubble is much smaller than either the 1 or 100 micron bubble. Thus, the maximum temperature attained by the 10 micron bubble is much less than in either of the other two bubbles.
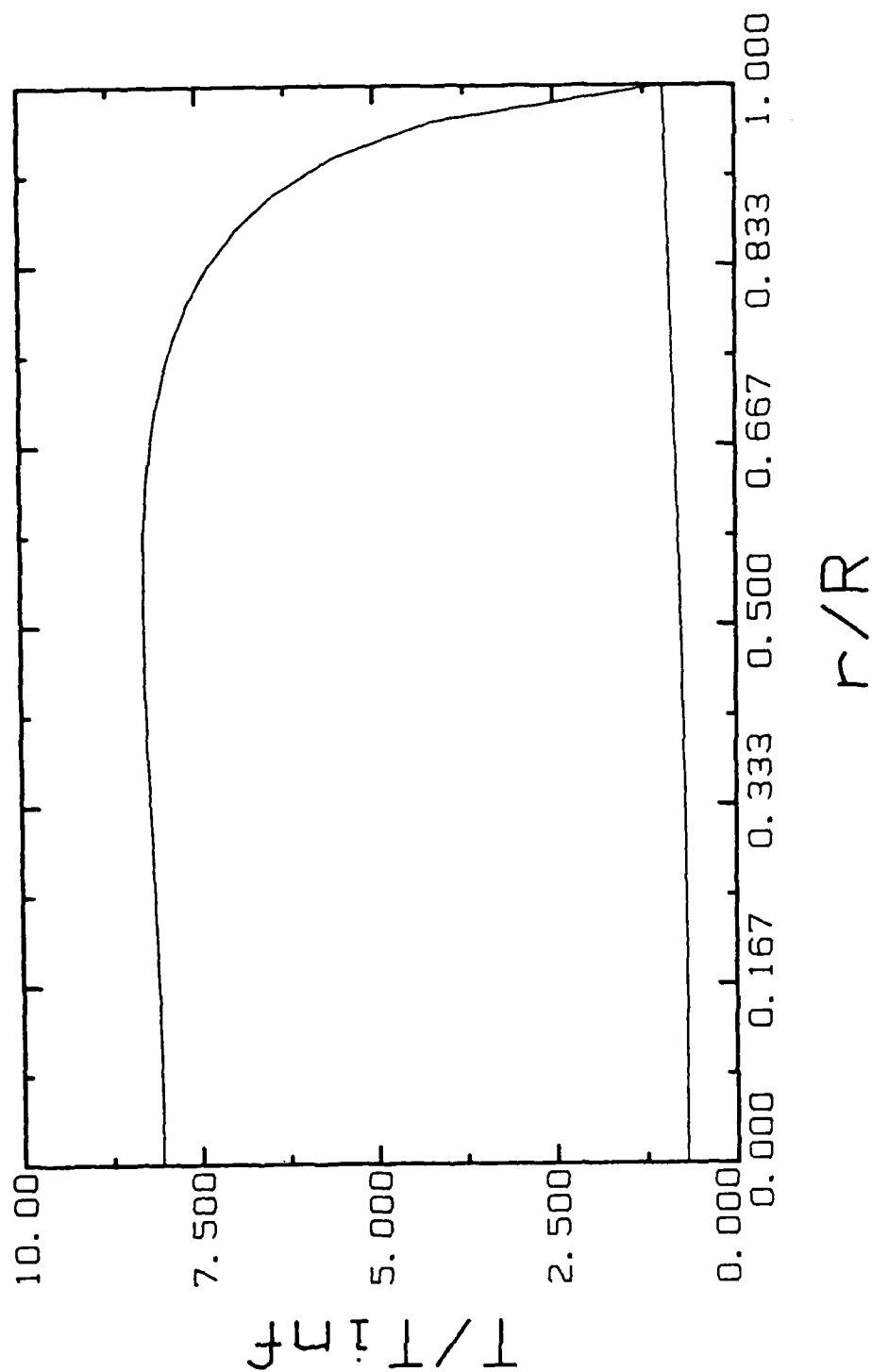
Figure 21. Temperature profile for a 100 micron bubble driven at 0.8 bar and 0.4 times the linear resonance frequency. Values for the minimum and maximum radius are shown.
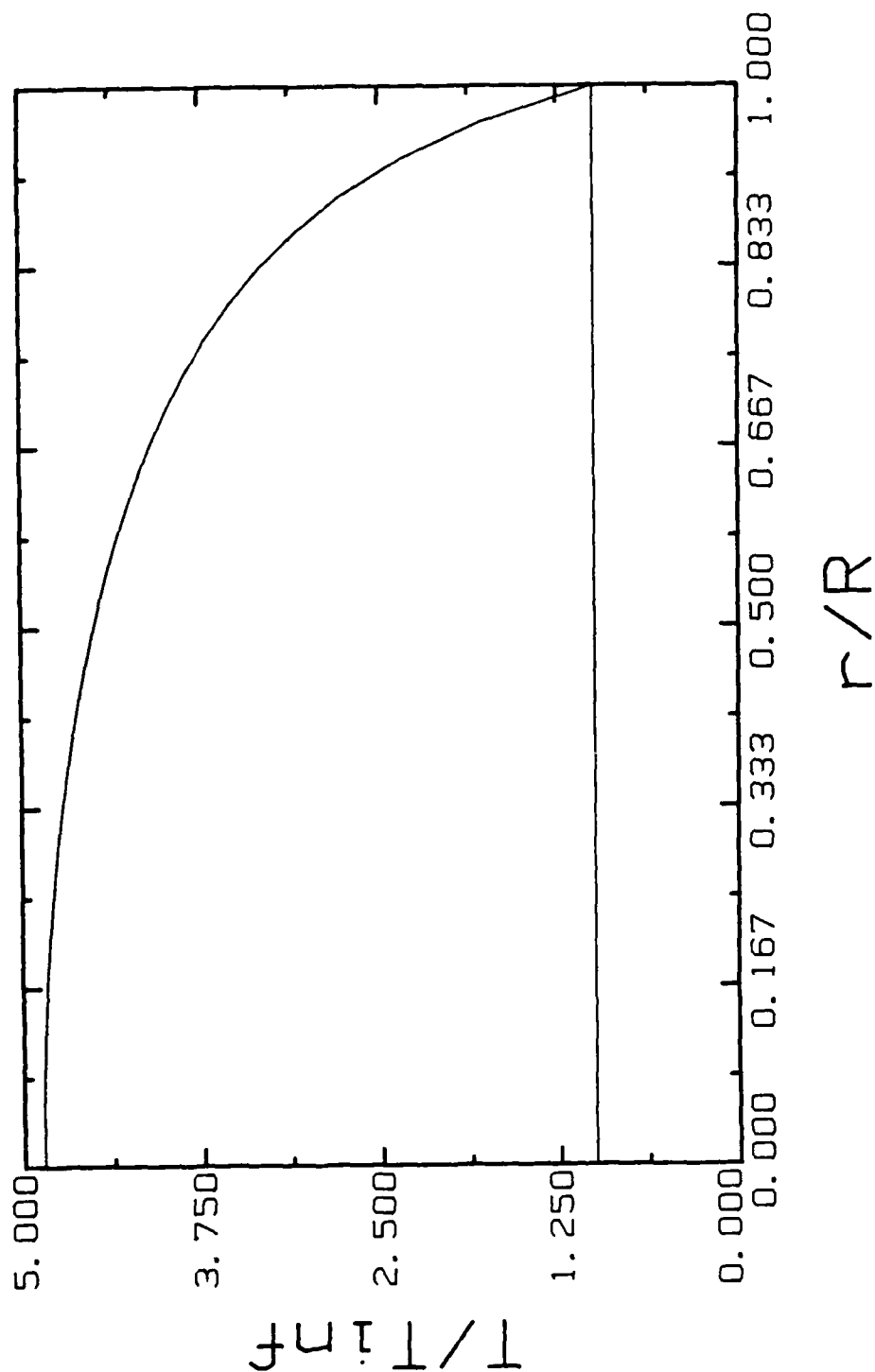
Figure 20. Temperature profile for a 10 micron bubble driven at 0.9 bar and 0.4 times the linear resonance frequency. Values for the minimum and maximum radius are shown.
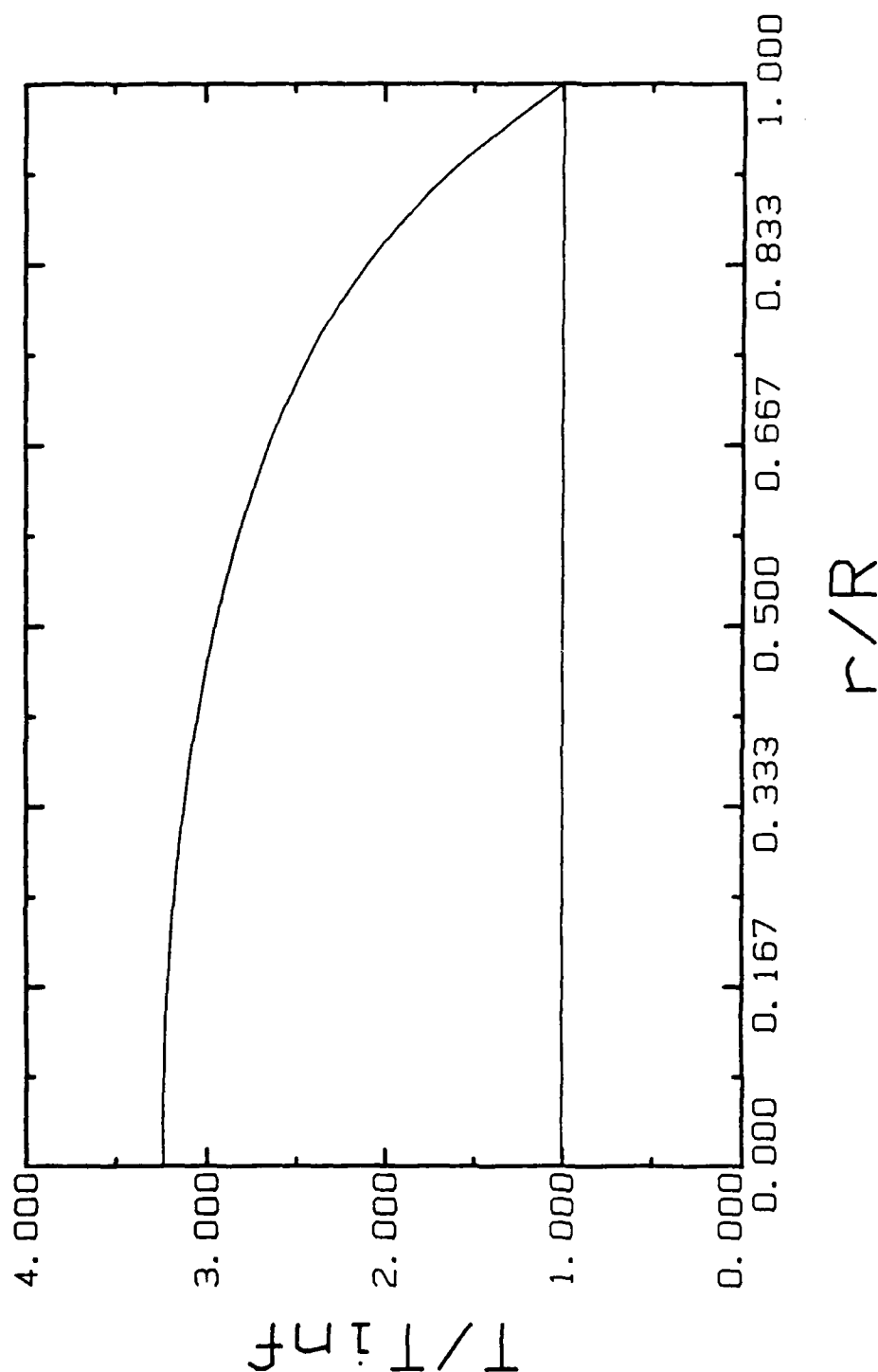
Figure 19. Temperature profile for a 1 micron bubble driven at 2.1 bar and 0.4 times the linear resonance frequency. Values for the maximum and minimum radius are shown.

volume and time, using the temperature profiles and an appropriate ionization probability function as the integrand.

Figures 19-21 are temperature profiles for 1, 10, and 100 micron bubbles at different stages of oscillation. The minimum and maximum value of the radius for each bubble during one cycle is chosen as the point where the temperature profiles are taken. The driving frequency for each figure is 0.4 times the linear resonance frequency of the bubble. The temperatures shown are normalized with respect to the ambient temperature of 293 degrees kelvin. Figure 19 shows a 1 micron bubble driven at 2.1 bar. Note that when the radius is a minimum, the center temperature is approximately 3.2 times the equilibrium temperature. Figure 20 shows a 10 micron bubble driven at 0.9 bar. Here the maximum temperature attained is approximately 4.9 times the equilibrium temperature. Finally, figure 21 shows a 100 micron bubble driven at 0.8 bar. For this case the maximum temperature attained is approximately 8.1 times the equilibrium value.

In each of these figures the maximum value of R/R_o is approximately 2.0. Thus, the small bubbles behave much more isothermally than do the large ones. Since the bubble wall moves slowly at large values of R/R_o, the interior temperature does not drop to the level that might be expected at the maximum value of the radius. Instead, a minimum temperature is reached when the radius of the bubble is somewhere between its equilibrium value and maximum value during the expansion cycle. As the bubble approaches its maximum size, the temperature of

D. Thermodynamics of the bubble interior

As has been mentioned previously, the internal pressure and temperature of a bubble are of particular interest to those studying the physiological effects of acoustic cavitation. There are several mechanisms by which a cavitating bubble can damage its surroundings. The best known of these mechanisms is that of destruction by the bubble wall itself. This area has been thoroughly studied because of cavitation damage to propellers on ships. However, we will not address this method of cavitation damage here. More recently, experimentalists have found that temperatures inside the bubble can become high enough to produce free radicals. The free radicals produced at these high temperatures can pose a serious threat to biological systems. One method of observing this phenomena is to look for sonoluminescence from cavitating bubbles.

The exact formulation for the internal pressure of the bubble has within itself a temperature array for the bubble interior. Thus, one solves for the internal temperature of a bubble as a function of both position and time. It is important to know how many free radicals are produced in a bubble over one cycle for a given set of parameters. One can estimate this number from the temperature profiles the computer program generates. One needs to know what fraction of the bubble's volume reaches the critical temperature for free radical formation and how long it remains at or above this temperature. A theoretical number of free radicals could be obtained by numerically integrating over
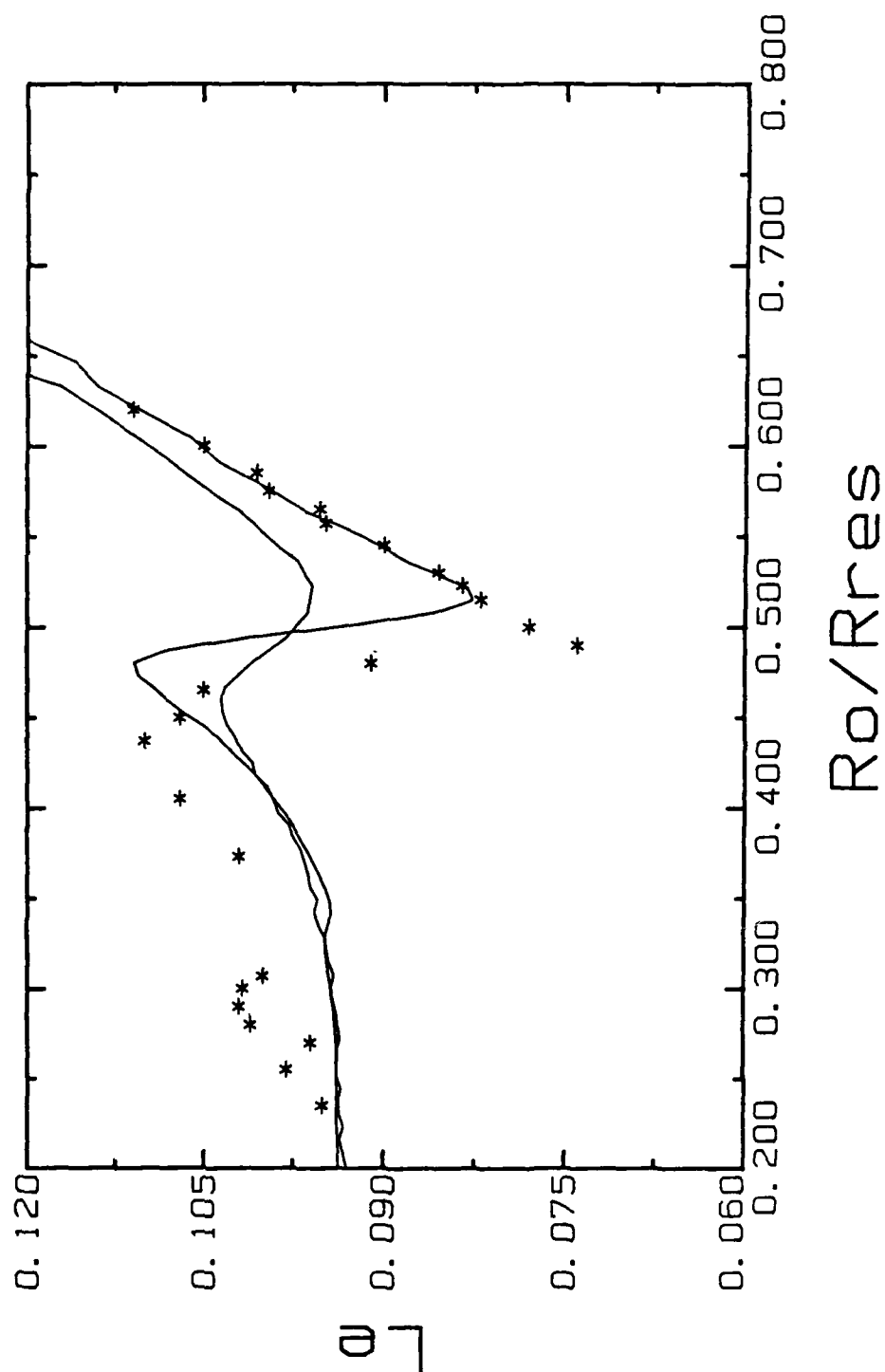
Figure 18. Levitation number as a function of the normalized radius for the CE and RPP methods. Freq.=22.2kHz, Pa=0.190 bar, asterisks denote experimental data from Crum [19].
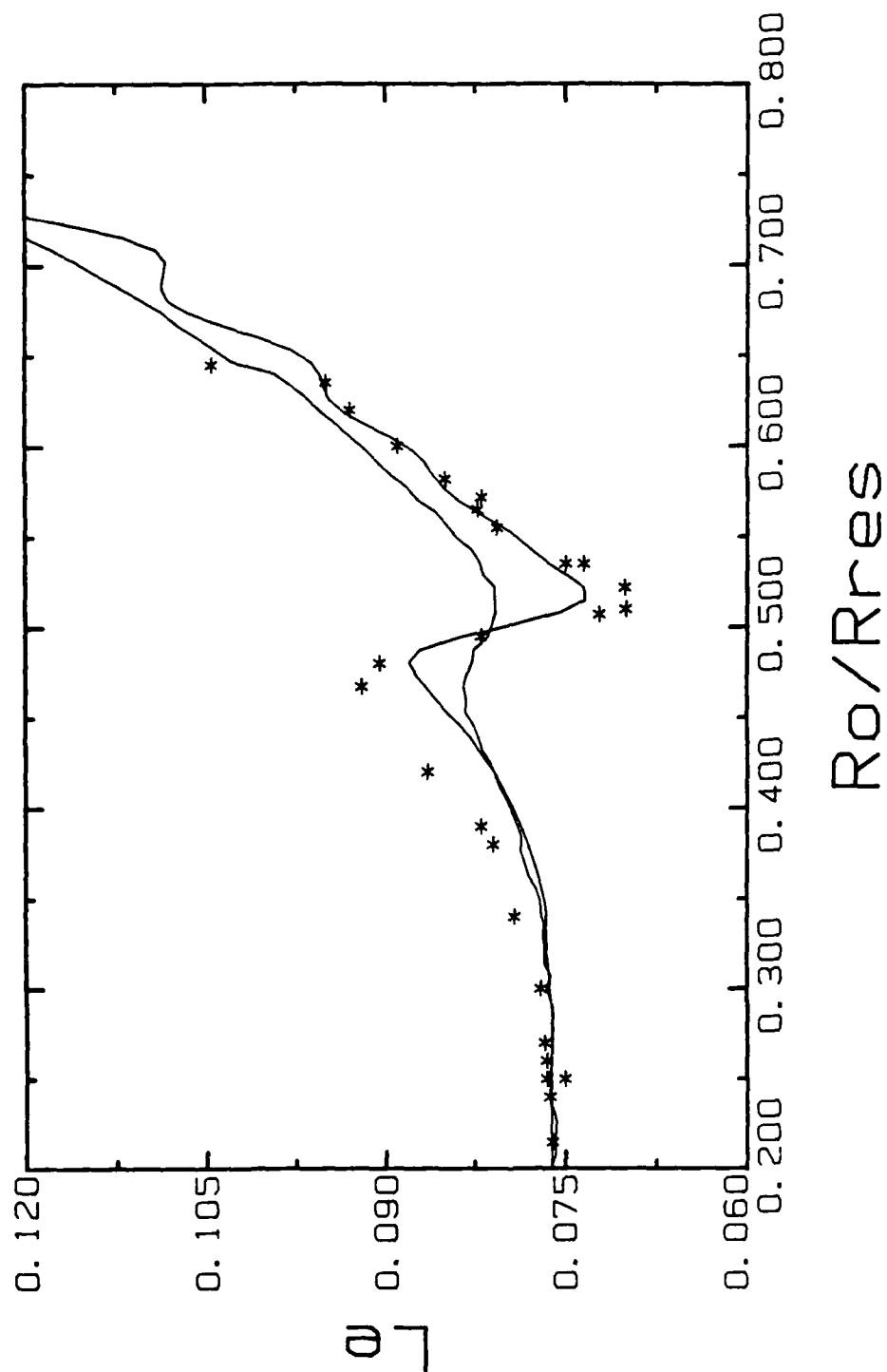
Figure 17. Levitation number as a function of the normalized radius for the CE and RPP methods. Freq.=22.2kHz, Pa=0.155 bar, asterisks denote experimental data from Crum [19].
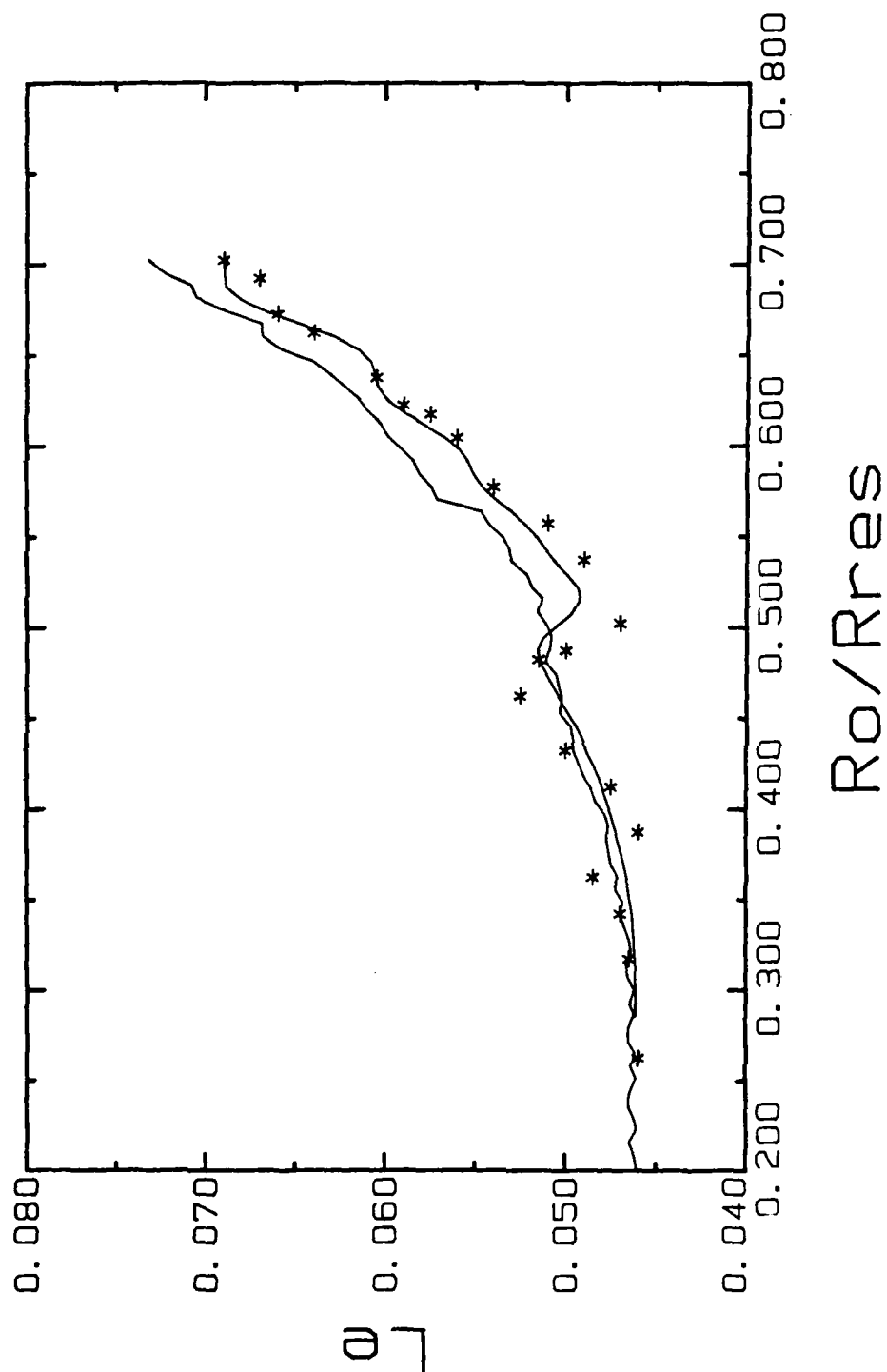
Figure 16. Levitation number as a function of the normalized radius for the CE and RPP methods. Freq.=22.2kHz, Pa=0.095 bar, asterisks denote experimental data from Crum [19].

as 1%. When this experiment is complete one should be able to determine the accuracy of the new theoretical model precisely.

Figures 16-18 show results for a frequency of 22.2 kHz and pressure amplitudes of 0.095, 0.155, and 0.190 bar respectively. In each figure the asterisks denote experimental points from reference [19]. The curve giving the best fit to the experimental data in each figure is the new theoretical model. From these figures one can conclude that the new theory is more accurate than the old polytropic exponent theory for the parameter range investigated.

the acoustic force is balanced by an average buoyancy force given by

$$F_B = \frac{4}{3}\pi R_o^3 \rho g <[R(t)/R_o]^3>, \tag{92}$$

where g is the acceleration due to gravity. Equating these two forces gives

$$|\nabla P_A| <[R(t)/R_o]^3 \cos\omega t> = \rho g <[R(t)/R_o]^3>. \tag{93}$$

Since ρg is the hydrostatic pressure gradient, one can rearrange equation (93) so that the right hand side is the levitation number as defined above. Thus equation (93) becomes

$$\frac{<[R(t)/R_o]^3 \cos\omega t>}{<[R(t)/R_o]^3>} = \frac{\rho g}{|\nabla P_A|} = L_e. \tag{94}$$

The left hand side of equation (94) can easily be evaluated for a numerical solution to equations modeling bubble oscillations. From this equation one can compute levitation numbers for both the CE method and the RPP method and compare the results to the experimental levitation numbers obtained by Crum. The experimental points are obtained in a rather straightforward manner and the technique is discussed in detail in reference [19]. There may be as much as a 10% error in obtaining the levitation numbers experimentally. However, it is assumed that the experimental data is accurate enough to determine which theoretical model best predicts the time evolution of an oscillating bubble when pulsation amplitudes are not too large. A more automated experimental procedure is being devised which could give results with

C. Levitation numbers

The ratio of the hydrostatic pressure gradient on a bubble to the acoustic pressure gradient has been referred to as the levitation number L_e by Crum and Prosperetti [19]. Before using this definition with the new theory, let us first recall where the expression arises in the first place.

The primary Bjerknes force or acoustic radiation pressure force on a bubble is given by Crum [53] as

$$F_A(\underline{r},t) = -<V(t)\nabla P(\underline{r},t)>, \tag{89}$$

where $V(t)$ is the time dependent volume of the bubble, $P(\underline{r},t)$ is the space and time dependent pressure outside the bubble, and the angle brackets denote the time average of the quantity inside. If one uses a levitation cell like the one used by Crum, then the pressure $P(\underline{r},t)$ in the cell is of the form

$$P(\underline{r},t) = P_\infty - P_A(z)\cos\omega t, \tag{90}$$

where $P_A(z)$ is the spatially dependent amplitude of the acoustic standing wave in the cell. Substitution of equation (90) into (89) gives the magnitude of the acoustic force as

$$F_A = \frac{4}{3}\pi R_o^3 |\nabla P_A| <[R(t)/R_o]^3 \cos\omega t>, \tag{91}$$

where R_o is the equilibrium radius of the bubble.

When the bubble remains in a fixed position in the levitation cell,
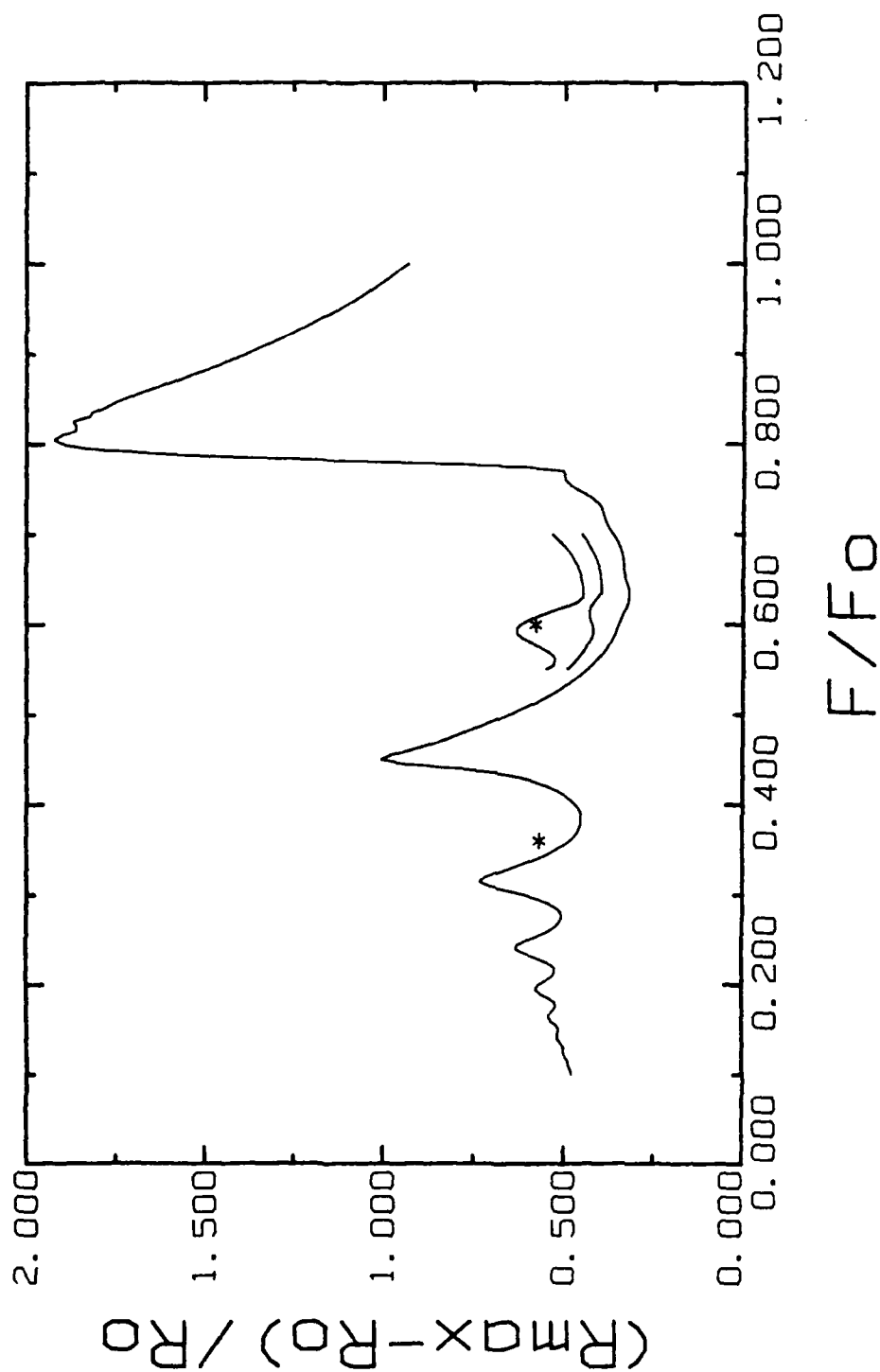
Figure 15. Maximum normalized bubble radius as a function of normalized frequency for the CE method. R_o =10 microns, Pa=0.7 bar, asterisks denote ultraharmonic resonance peaks from Lauterborn's figure [52] (partial curves are included for Pa=0.8 and 0.9 bar).

reveals missing ultraharmonic resonance peaks in figure 13. For example, Lauterborn's figure shows a 3/2 ultraharmonic, whereas figure 13 does not. In order to be sure that these peaks are not being skipped by too large a step size in the frequency domain, another calculation is made with twice as many points in the frequency domain than before. This result is presented in figure 15 for a 10 micron bubble driven at 0.7 bar along with some partial curves at 0.8 and 0.9 bar. Points taken from ultraharmonic peaks in Lauterborn's figure are denoted by asterisks. Again the ultraharmonic resonances are missing from our curve at 0.7 bar, but they begin to appear as the pressure is increased. Qualitatively, the two theories give similiar results, but there are significant quantitative differences which can be important in certain applications as mentioned previously.

Although there are good indications that the new theory is more accurate in some parameter domains, one should wait for future experimental results before deciding which theory best predicts the frequency response of the bubble in these high amplitude regions.

Figure 22. Center temperature as a function of time for a 1 micron bubble driven at 1.4 bar, and frequencies of 0.4 and 0.8 times the linear resonance frequency.

Figure 23. Center temperature as a function of time for a 10 micron bubble driven at 0.6 bar, and frequencies of 0.4 and 0.8 times the linear resonance frequency.

74
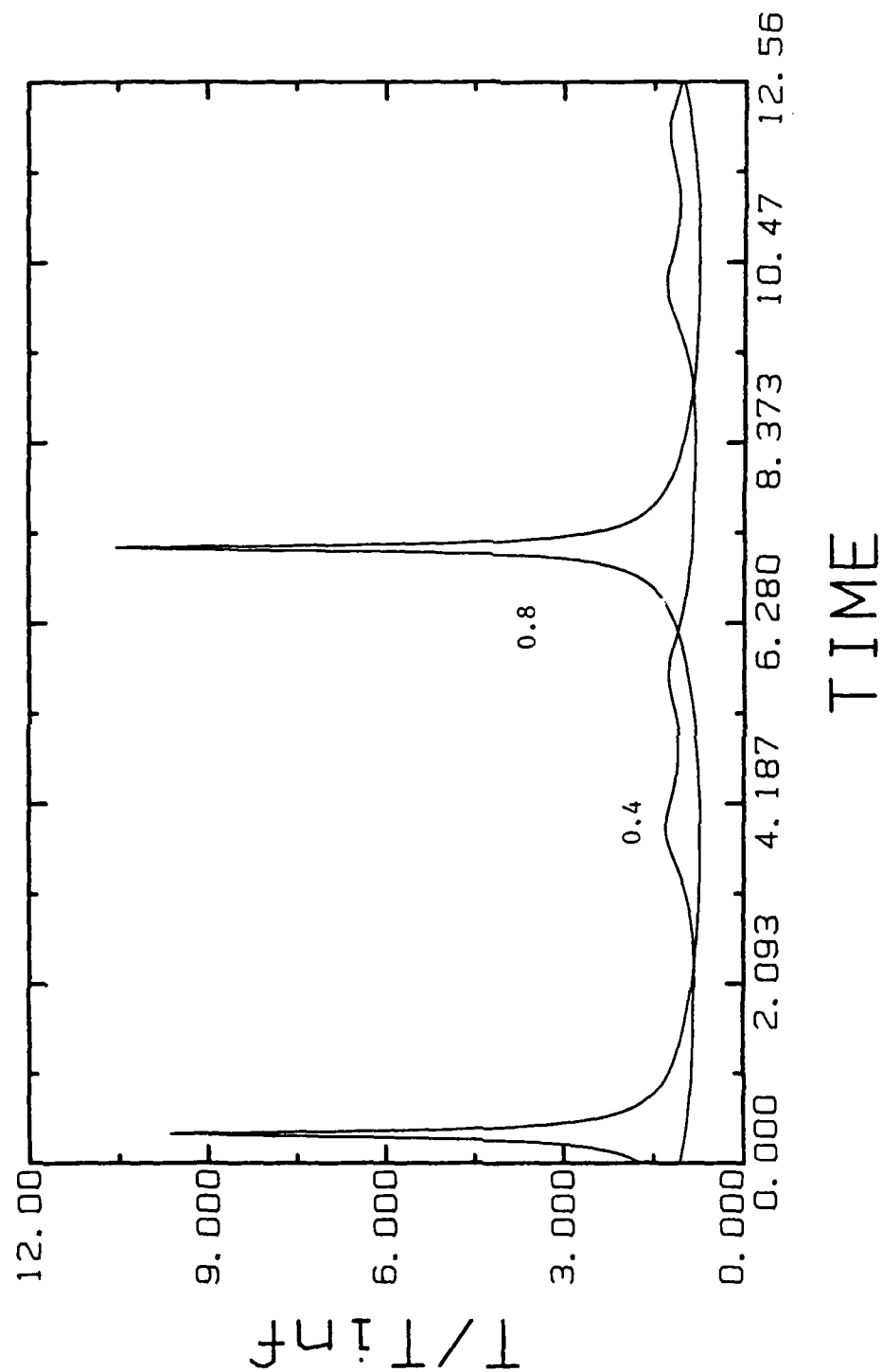
Figure 24. Center temperature as a function of time for a 100 micron bubble driven at 0.45 bar, and frequencies of 0.4 and 0.8 times the linear resonance frequency.

To complete this thermodynamic look at an oscillating bubble, one must examine the internal pressure of a bubble as a function of time. Recall that it was previously assumed that the internal pressure is a function of time only. It has been predicted that internal pressures of hundreds of atmospheres may be attained during the violent collapse of a bubble. It will be shown that under the proper conditions the new theory predicts that internal pressures on the order of hundreds of atmospheres are attained by bubbles with large pulsation amplitudes. Figures 25-27 were calculated under the same conditions as figures 22-24. In each case the pressure is normalized with respect to atmospheric pressure. Note that figure 27 shows an internal pressure higher than 300 atmospheres. These high pressures last only a short time as do the high temperatures discussed previously.

Finally, figure 28 is presented with the radius, internal pressure, and center temperature all on the same figure. The equilibrium radius of the bubble is 50 microns, the driving pressure amplitude 0.6 bar, and the driving frequency 0.4 times the linear resonance frequency. From this figure it is easy to see the phase relationship between the radius, pressure, and temperature of the bubble. The arrows on the figure indicate the positions of lowest internal temperature during the two cycles shown. This figure supports our earlier claim, that the minimum value of the gas temperature occurs when the radius of the bubble is increasing between R_o and its maximum value.
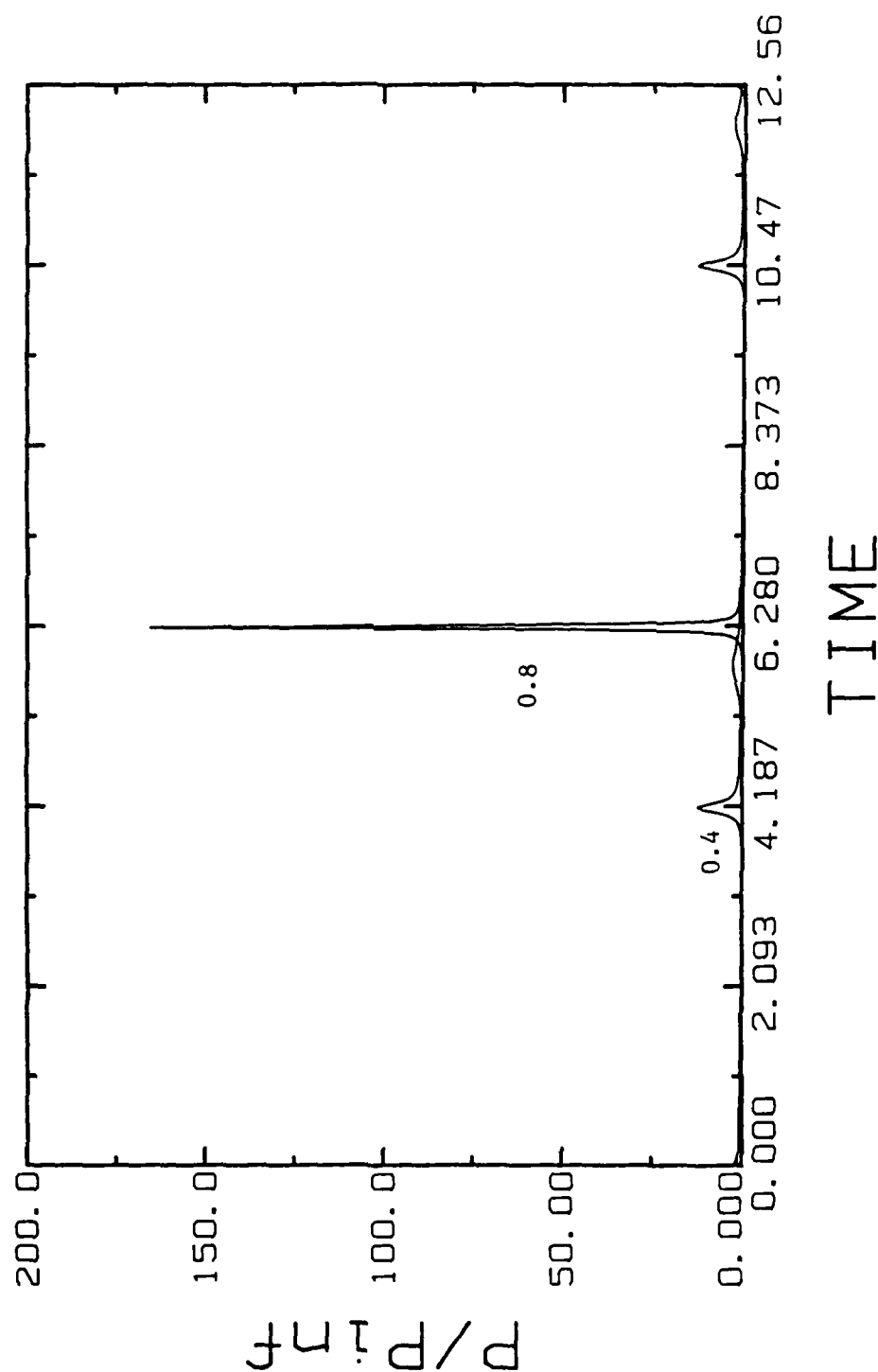
Figure 25. Internal pressure as a function of time for a 1 micron bubble driven at 1.4 bar, and frequencies of 0.4 and 0.8 times the linear resonance frequency.
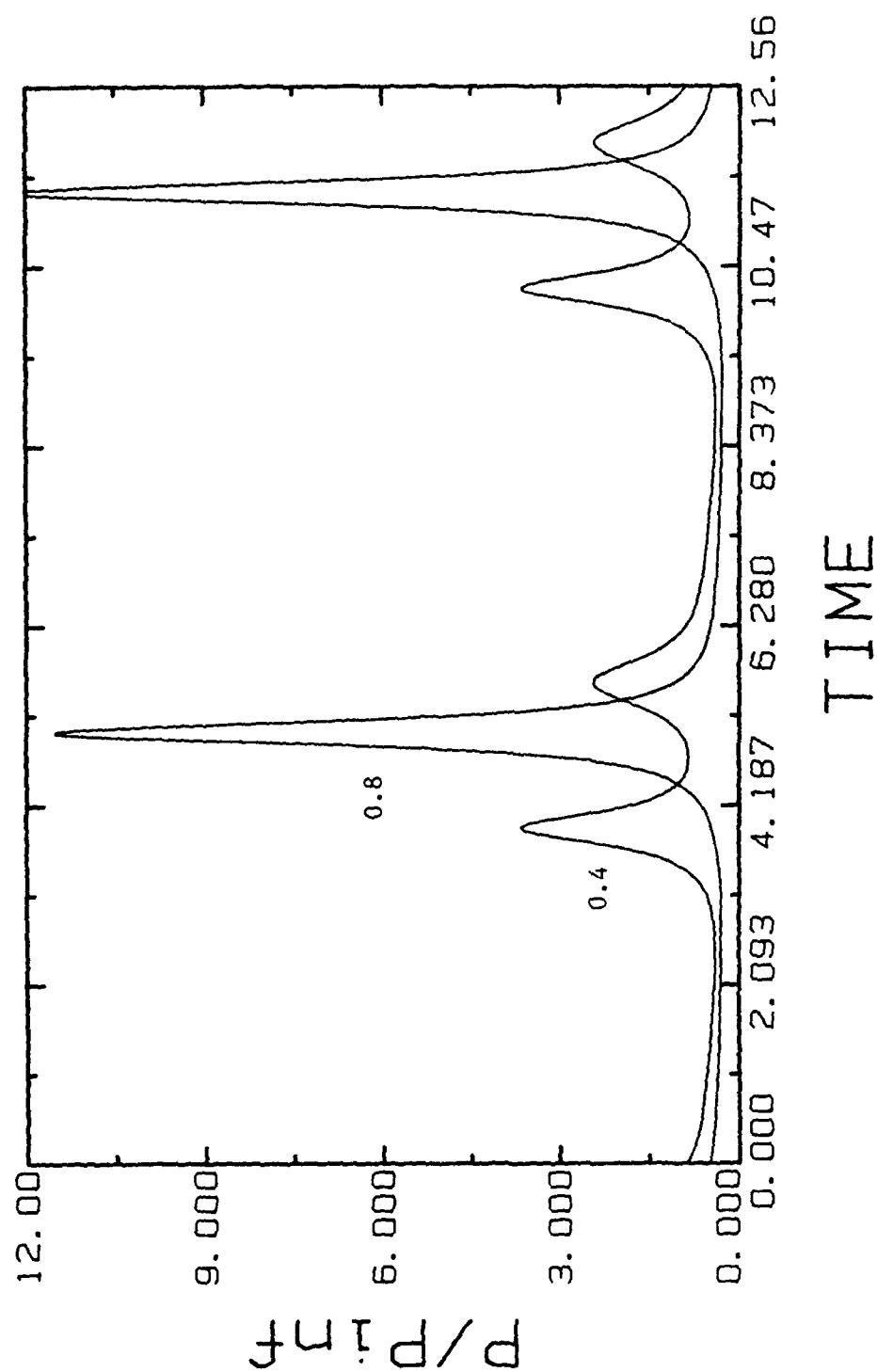
Figure 26. Internal pressure as a function of time for a 10 micron bubble driven at 0.6 bar, and frequencies of 0.4 and 0.8 times the linear resonance frequency.
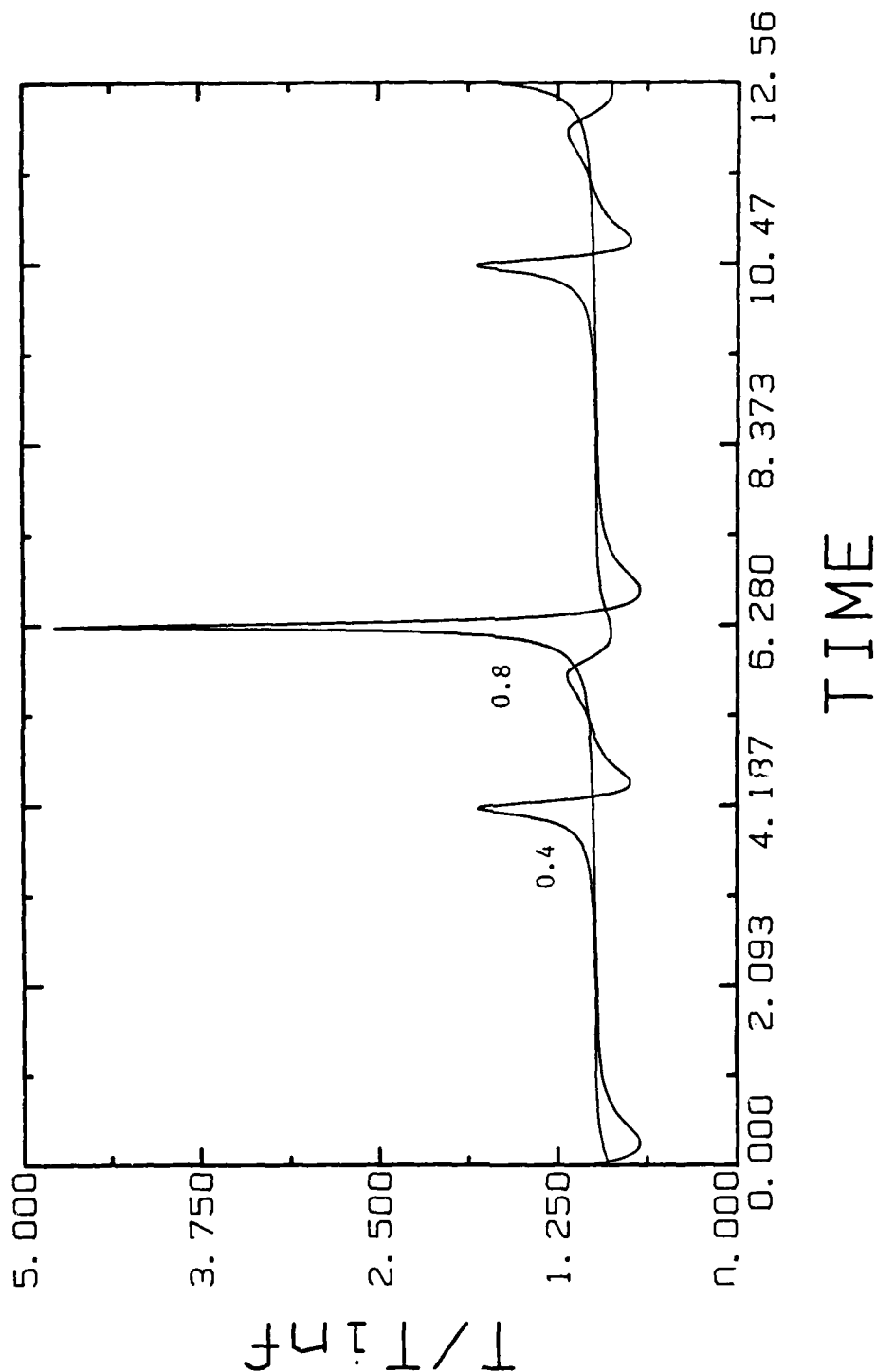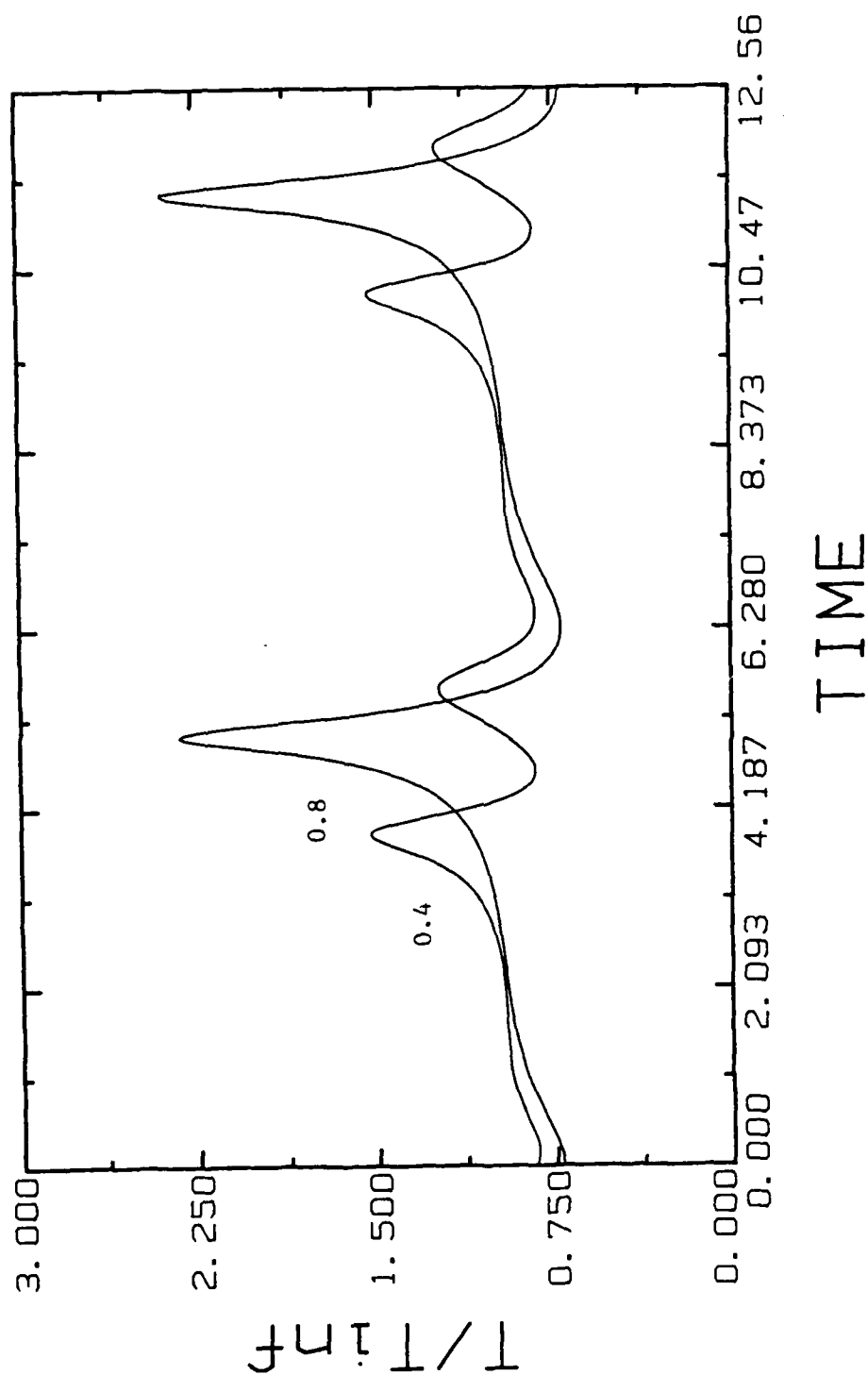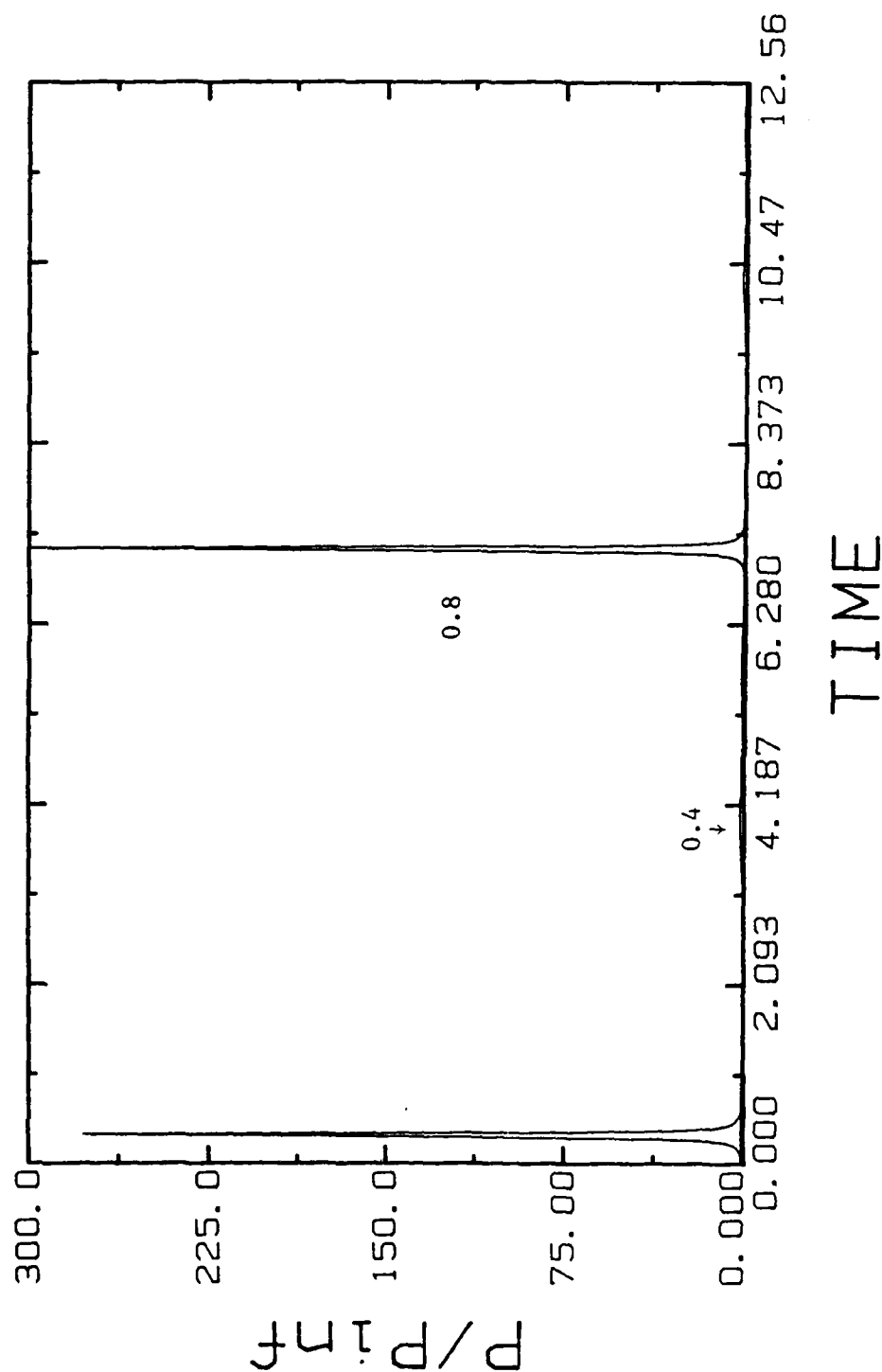
Figure 27. Internal pressure as a function of time for a 100 micron bubble driven at 0.45 bar, and frequencies of 0.4 and 0.8 times the linear resonance frequency.
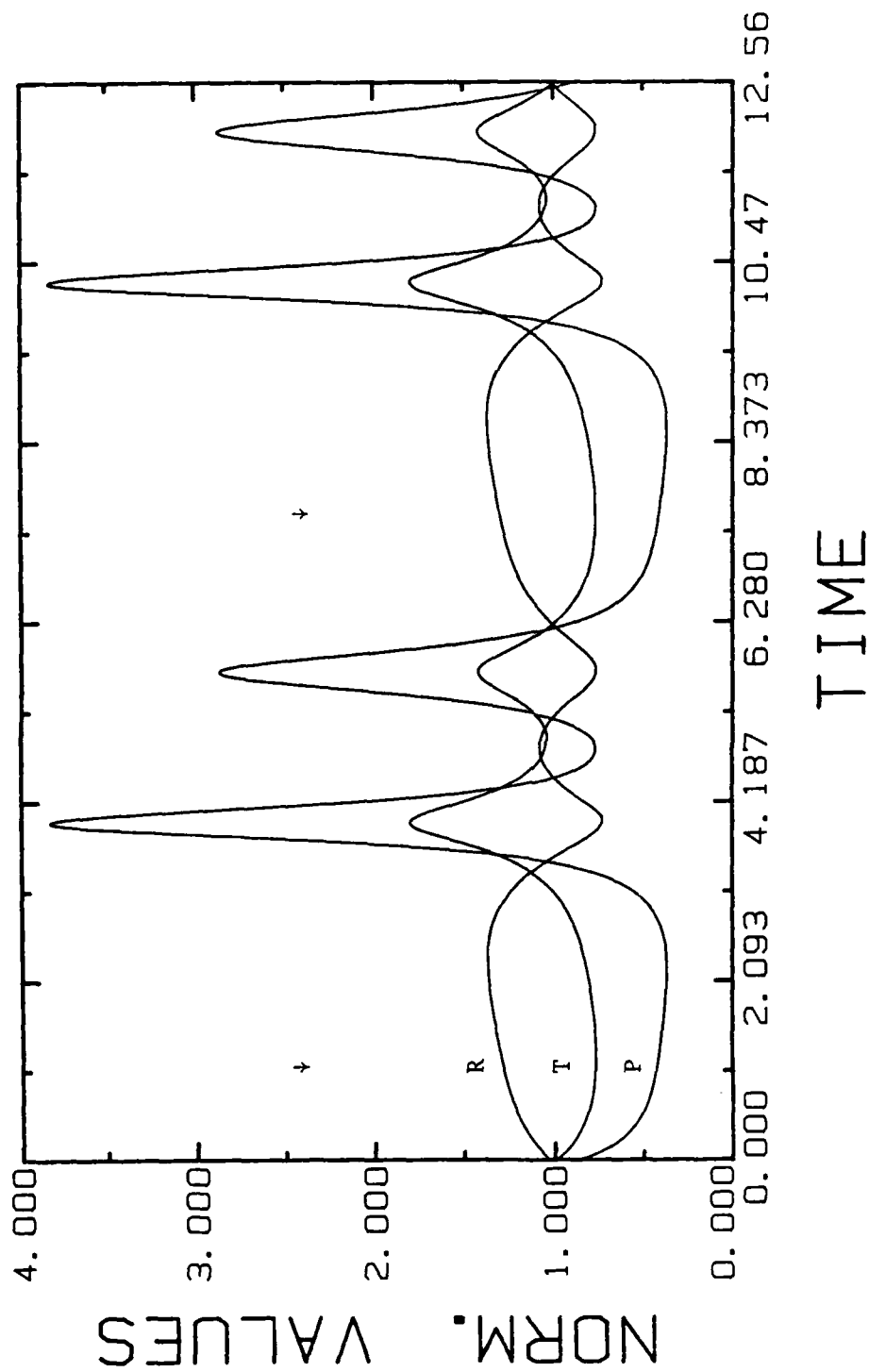
Figure 28. Radius, internal pressure, and center temperature as a function of time for a 50 micron bubble driven at 0.6 bar and a frequency of 0.4 times the linear resonance frequency.

Chapter 4

A Systematic approach to chaotic bubble motion

In recent years, the numerical investigation of nonlinear dynamical systems has revealed many exciting features. Perhaps the most exciting discovery of all was period-doubling bifurcation as a universal route to chaos [11]. Some other interesting discoveries are the coexistence of attractors with complex basin structures and the strange attractors which exhibit the property of sensitive dependence on initial conditions. A thorough discussion of these and many other features of nonlinear dynamical systems is found in the text by Guckenheimer and Holmes [54].

In 1983 a number of researchers discovered another exciting phenomenon associated with nonlinear dynamical systems [55-57]. These researchers have shown that a variety of dynamical systems exhibit the property of finite period doubling sequences merging with inversely advancing ones to form a finite number of "bubbles" on some cross section of the parameter space. A consequence of this merging of period doubling sequences is localized regions of stable orbits and other localized regions of chaotic motion [12].

Probably the most thoroughly studied dynamical system is the Duffing equation [58]

$$\ddot{X} + a\dot{X} + X + X^3 = b\cos(\omega t). \tag{95}$$

One outstanding feature of this equation is that it exhibits all of the properties we have mentioned above. Parlitz and Lauterborn [59] give a more global view of the Duffing equation by emphasizing the important role of the nonlinear resonances, which cause many of the striking features mentioned above.

One would like to have a global view of the new acoustic cavitation equations, similar to the one given for the Duffing equation in reference [59]. However, because of the complexity of the system, this is very difficult. The many parameters that can be varied in the acoustic cavitation equations make a global analysis virtually impossible. One can, however, learn a great deal about the system by using the techniques described above. Both the Rayleigh–Plesset equation employing the polytropic approximation, RPP, and the new exact formulation, CE, are examined in this fashon.

One particularly useful technique is that of bifurcation analysis of the solutions. In general, one follows the norm of a trajectory ϕ (which is a solution of the equations in the phase space $(\phi,\dot{\phi})$) as it changes with respect to changes in a control parameter μ. For the multi-parameter case, one holds all the parameters fixed except for the one of current interest – in the case of interest this is the driving pressure amplitude. One then constructs a bifurcation curve for that parameter; that is, one plots the locus of points in the Poincare section [60] verses the control parameter.

In simpler terms, this means one plots the value of the radius at

times that are multiples of the period of the driving pressure. This technique is used at each increment of the pressure amplitude to complete the figure. If the bubble is oscillating with a period equal to that of the driving pressure, one gets a single point for each value of the pressure amplitude. If the period of the bubble's oscillations is twice that of the driving pressure, two values of the radius are obtained for each value of the pressure amplitude, and so on. This type of graph is known as a "Feigenbaum tree".

In order to make a comparison between the two theories, one chooses the same set of initial conditions or parameters. We choose a bubble with an equilibrium radius of 50 microns and a driving frequency equal to half of the linear resonance frequency of the bubble. Figure 29 shows the results for the RPP equation and figure 30 the results for the CE equations. Since the damping is quite different for each model, the range of driving pressures where interesting phenomena occur is different as well.

The most striking difference between the two figures, however, is that the RPP equation exhibits a period-doubling bifurcation route to chaos, while the CE equations exhibit period bubbling and an intermittent transition to chaos. An interesting feature of the RPP Feigenbaum tree is the missing arms from the second bifurcation point. The reason for the missing arms is conjectured to be due to a broken symmetry in the mapping sequence at the second bifurcation poin [61]. From reference [12], one can conclude that varying the driving frequency

toward a resonance peak would introduce more structure in the figures, particularly in figure 30. One would expect to see period doubling in the bubbles of figure 30, and perhaps even a region of chaos in the bubble itself.

Unfortunately, the computer time required for a "Feigenbaum tree" using the CE equations is over one week on a Digital PDP 11/73. This time constraint has severely limited the scope of the present investigation. As faster microcomputers become available, this type of analysis is sure to become more and more popular.

Although global predictions cannot be made for either of the two theories investigated, we have learned that the damping used in each system determines, to a large degree, the characteristics of the oscillations. Thus, one can compare an analysis of this type to "Feigenbaum trees" obtained experimentally, to determine which model of the damping is more accurate. An experiment of this type is planned, using the technique described in section D of chapter 2.
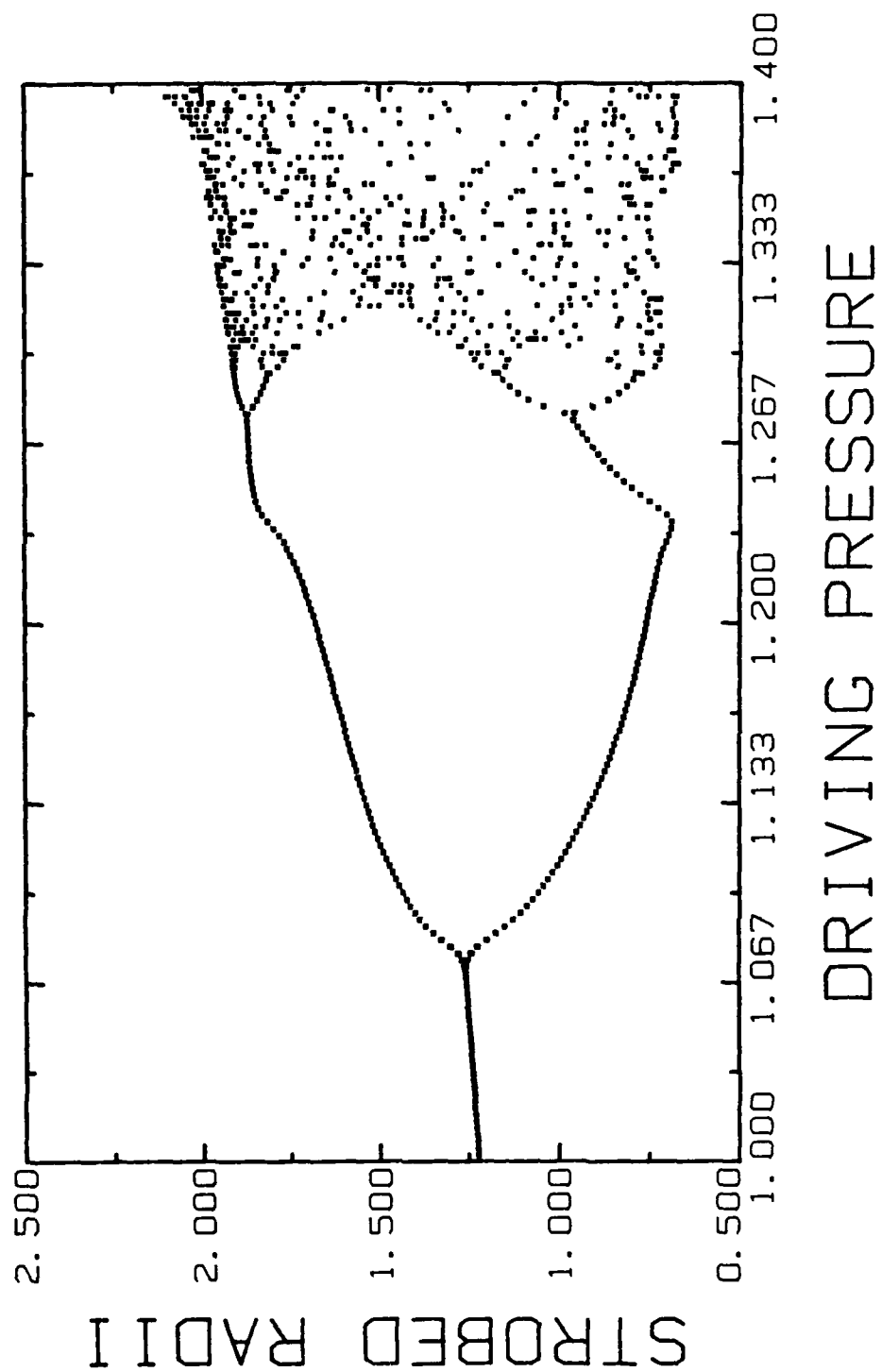
Figure 29. "Feigenbaum tree" for the RPP equation.
$R_o = 50$ microns and $f/f_o = 0.5$.
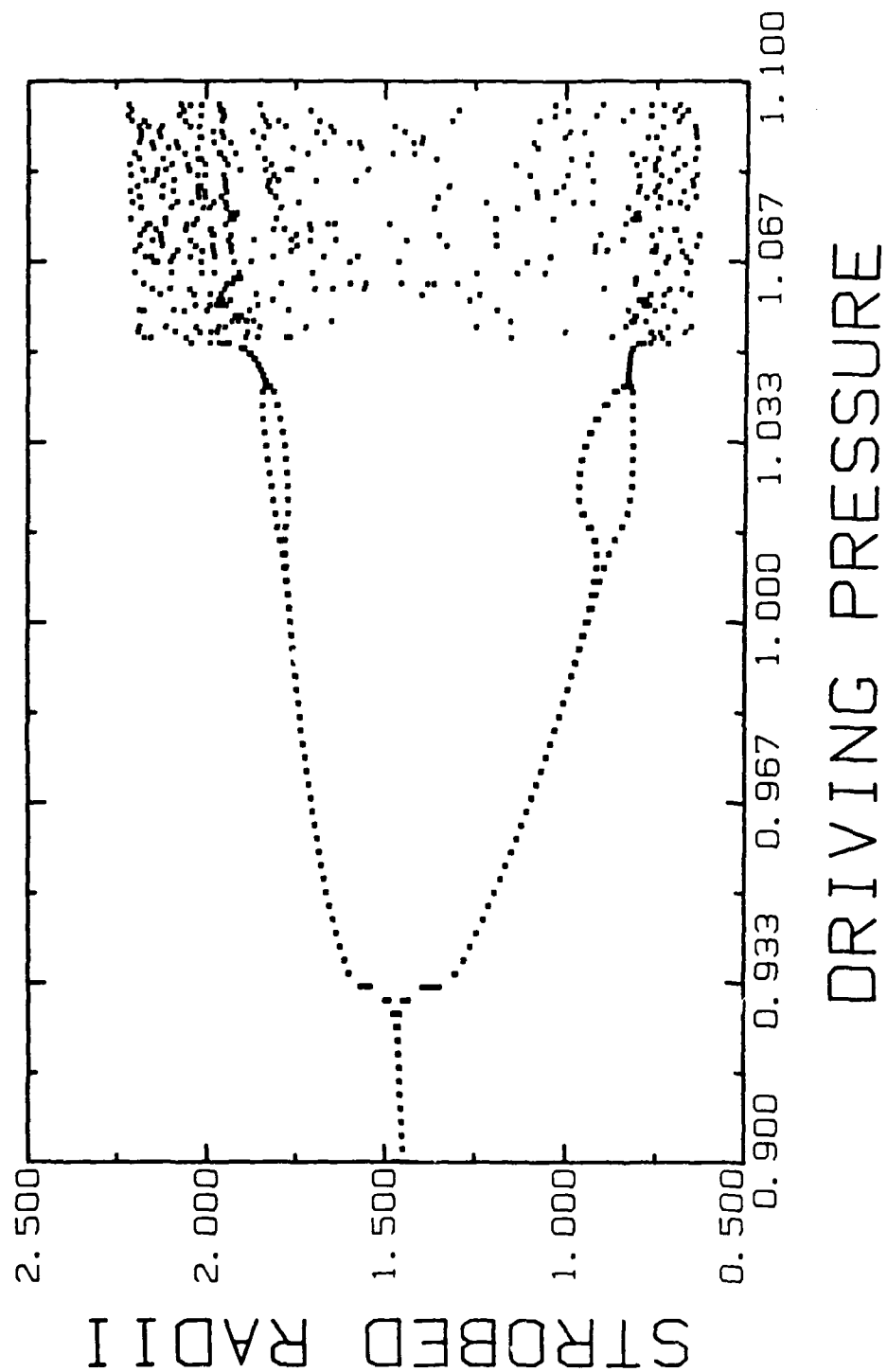
Figure 30. "Feigenbaum tree" for the CE equations.
R_o =50 microns and f/f_o =0.5.

1·0

2·8
3·15
3·5
4·0
4·5

2·5
2·2
2·0

1·1

1·8

1·25 1·4 1·6
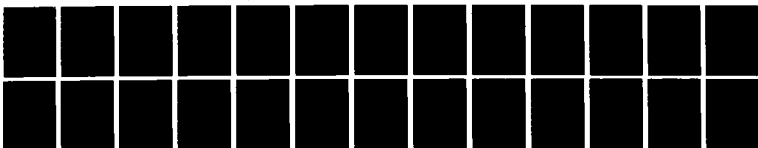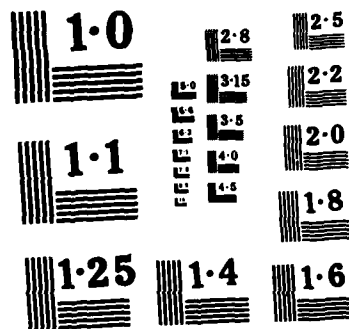
NATIONAL BUREAU OF STANDARDS
MICROCOPY RESOLUTION TEST CHART

Chapter 5

Conclusions and topics for future study

The purpose of this study was to show that an exact formulation for the internal pressure of a cavitating bubble leads to a more applicable solution of an equation modeling acoustic cavitation. The strongest evidence obtained to support this claim is the reasonably close agreement between experimental levitation numbers and the ones obtained numerically using the new theory. The exact formulation shows the strong second harmonic resonance peak in the levitation number curves, whereas the polytropic approximation shows very little resonance effect at all.

One can conclude from this study, that for small pulsation amplitudes and driving frequencies below one fourth of the resonance frequency of a bubble, the polytropic approximation is sufficiently accurate and should be used when computer time is a factor. Under other conditions, however, the new formulation should be used unless the pulsation amplitude is large. For large pulsation amplitudes one cannot be so positive about the new theory. Some of the approximations are no longer valid when the pulsation amplitude of the bubble approaches twice the equilibrium radius. One must wait for new experimental results before saying how accurate the new theory is in this region.

It has been observed that the polytropic approximation gives a

value for the damping that is too large when the driving frequency is near a harmonic resonance. There are a number of ways to modify the damping term in equations using the polytropic approximation to help compensate for the overdamping at the resonance peaks. Some of these methods may give results as accurate as the exact method. However, this is not very pleasing to the theoretician interested in understanding the physics of a cavitation bubble. Unfortunately, one must pay a high price for this elegant theory in terms of the complexity of its numerical solution. The exact formulation requires about an order of magnitude more computer time than does the polytropic formulation with an artificial damping term included.

The artificial damping techniques have some difficulties of their own, however. There is no one corrective term of this type that works well over a large range of equilibrium radii, driving frequencies, and driving pressure amplitudes. This is a serious limitation when trying to predict the global behavior of an acoustic cavitation theory.

One possible solution to this problem is to replace the polytropic exponent and artificial damping terms with a single function for the internal pressure. As stated previously, this function for the internal pressure must be dependent on the equilibrium radius, the driving frequency, and the driving pressure amplitude. A study such as the one here may be of great help in devising such a function. Figures have been presented for the internal pressure at various equilibrium radii, driving frequencies, and driving pressure amplitudes. These figures are

very useful when trying to find the functional dependence of the internal pressure on the parameters mentioned.

In several of the figures presented in the previous chapters, the new theory was pressed to the limits of its applicability. One would like to extend the applicabiblity of the exact formulation into the region of large pulsation amplitudes. There are essentially two problems which must be overcome in order to extend the theory to this region.

First, the second order numerical integrator needs to be replaced by the fourth order Adams—Moulton method. Also, one needs to find a more accurate method than the Crank-Nicolson method used to solve for the internal temperature. These higher order methods would greatly reduce the numerical error made during the collapse phase of the bubble's cycle when the pulsation amplitude is large.

The second problem encountered is that of inapplicability of the equations for the internal pressure when the pulsation amplitude of the bubble is too large. Recall that in deriving these equations, it was assumed in several places that the velocity of the bubble wall was small compared to the speed of sound in the gas. However, this condition does not hold when the pulsation amplitude of the bubble is very large. Hence, one must retain some of the terms discarded in the earlier derivation in order to maintain applicability in the large pulsation amplitude region. This will in turn make the numerical integration more complex and time consuming on the computer. Further investigations are

needed to find the most useful model which takes into account all of the difficulties mentioned above.

In previous chapters several experiments were described that would help to advance the theory of acoustic cavitation. The importance of these experiments cannot be overemphasized. Experimental data at large pulsation amplitudes that is sensitive to the damping is very important to the theory.

Lauterborn has carried out several experiments in which he examines the acoustic emissions of a bubble field and has been able to detect the onset of different modes of oscillation as the driving pressure is increased. The onset of these different modes corresponds to a bifurcation point on a "Fiegenbaum tree". An experiment of this type could be conducted with a single bubble in a levitation cell, such as the one used by Crum. This would give an experimental "Feigenbaum tree" which could be used to test the theories. In chapter 4 it was seen that the bifurcation points were very sensitive to the damping, so this is an appropriate test for the damping models.

The laser light scattering experiment described in chapter 2 is probably the most important experiment of all the ones mentioned. This experiment could provide an exact radius verses time curve that would be very useful in developing an appropriate model of the internal pressure or damping.

Until the successful completion of some of the experiments suggested, or perhaps some others not mentioned here, one can only

speculate as to the applicability of the present theory to bubbles with large pulsation amplitudes. One can, however, say that this exact approach to the internal pressure of a cavitating bubble gives more accurate results in its region of applicability than does the polytropic approximation. It is also pleasing to the physicist to have a theoretical model that agrees with experiments without resorting to artificial viscosities or damping terms.

REFERENCES

1. E. A. Neppiras, "Acoustic Cavitation", Physics Reports $\underline{61}$, 159-251 (1980).

2. W. H. Besant, *Hydrostatics and Hydrodynamics*, C.U.P., London (1859).

3. Lord Rayleigh, "On the pressure developed in a liquid during the collapse of a spherical cavity", Phil. Mag. $\underline{34}$, 94-98 (1917).

4. F. G. Blake Jr., Technical Memo No. 12, Acoustics Research Laboratory, Harvard University, (1949).

5. M. S. Plesset, "The Dynamics of Cavitation Bubbles", Journal of Applied Mechanics $\underline{16}$, 277-282 (1949).

6. B. E. Noltingk and E. A. Neppiras, Proc. Phys. Soc. B (London) $\underline{63B}$, 674, (1950).

7. E. A. Neppiras and B. E. Noltingk, Proc. Phys. Soc. B (London) $\underline{64B}$, 1032, (1951).

8. H. Poritsky, Proc. $1\underline{\underline{st}}$ U.S. National Congress in Applied Mechanics (A.S.M.E.) 813, (1952).

9. C. Sehgal, R. G. Sutherland, and R. E. Verrall, "Optical Spectra of Sonoluminescence from Transient and Stable Cavitation in Water Saturated with Various Gases", Journal of Physical Chemistry, $\underline{84}$, 338 (1980).

10. A. Prosperetti, "Physics of Acoustic Cavitation", Proceedings from "Frontiers in Physical Acoustics", Italian Physical Society, (1985).

11. M. J. Feigenbaum, "The Universal Metric Properties of Nonlinear Transformations", Journal of Statistical Physics $\underline{21}$, 669-706 (1979).

12. M. Bier and T. C. Bountis, "Remerging Feigenbaum Trees in Dynamical Systems", Physics Letters $\underline{104A}$, 239-244 (1984).

13. H. G. Flynn, Proc. 3$^{\text{rd}}$ International Congress on Acoustics, 336-339, (1959).

14. H. G. Flynn, Tech. memo No. 50, Acoustics Research Laboratory, Harvard University, (1963).

15. A. Prosperetti, "Nonlinear oscillations of gas bubbles in liquids: steady-state solutions", Journal of the Acoustical Society of America 56, 878-885 (1974).

16. L. A. Crum and A. Prosperetti, "Erratum and Comments on "Nonlinear oscillations of gas bubbles in liquids: An interpretation of some experimental results" (J.A.S.A. 73, 121-127, (1983)", Journal of the Acoustical Society of America 75, 1910-1912, (1984).

17. E. Cramer, "The Dynamics and Acoustic Emission of Bubbles Driven by a Sound Field", in Cavitation and Inhomogeneities in Underwater Acoustics, ed. W. Lauterborn, 54-63 (1984).

18. W. Lauterborn and E. Suchla, "Bifurcation Superstructure in a Model of Acoustic Turbulence", Phys. Rev. Letters 53, 2304-2307 (1984).

19. L. A. Crum and A. Prospretti, "Nonlinear oscillations of gas bubbles in liquids: An interpretation of some experimental results", Journal of the Acoustical Society of America 73, 121-127 (1983).

20. E. Ott, "Strange attractors and chaotic motions of dynamical systems", Reviews of Modern Physics 53, 655-671 (1981).

21. B. A. Huberman and J. P. Crutchfield, "Chaotic States of Anharmonic Systems in Periodic Fields", Phys. Rev. Letters 43, 1743-1747 (1979).

22. C. Grebogi, E. Ott, and J. A. Yorke, "Crises, Sudden Changes in Chaotic Attractors, and Transient Chaos", Physica 7D, 181-200 (1983).

23. G. K. Batchelor, An Introduction to Fluid Dynamics, Cambridge University Press, New York (1980).

24. R. Aris, Vectors, Tensors, and the Basic Equations of Fluid Dynamics, Prentice-Hall, Inc. Englewood Cliffs, N.J. (1962).

25. R. B. Bird, W. E. Stewart, and E. N. Lightfoot, Transport Phenomena, John Wiley & Sons, Inc. New York (1960).

26. L. D. Landau and E. M. Lifshitz, Fluid Mechanics, Pergamon Press, London (1959).

27. P. Lu, Introduction to the Mechanics of Viscous Fluids, Hemisphere Publishing Corp., Washington (1977).

28. J. E. A. John, Gas Dynamics, Allyn and Bacon, Inc., Boston (1969).

29. J. J. Bertin and M. L. Smith, Aerodynamics For Engineers, Prentice-Hall, Inc., Englewood Cliffs, N.J. (1979).

30. F. R. Gilmore, "The Collapse and Growth of a Spherical Bubble in a Viscous Compressible Liquid", Cal. Tech. Hydrodynamics Lab. Report No. 26-4 (1952).

31. L. Trilling, "The Collapse and Rebound of a Gas Bubble", Journal of Applied Physics 23, 14-17 (1952).

32. J. B. Keller and I. I. Kolodner, "Damping of Underwater Explosion Bubble Oscillations", Journal of Applied Physics 27, 1152-1161 (1956).

33. R. Hickling and M. S. Plesset, "Collapse and Rebound of a Spherical Bubble in Water", Physics of Fluids 7, 7-14 (1964).

34. W. E. Jahsman, "Collapse of a Gas-Filled Spherical Cavity", Journal of Applied Mechanics 35, 579-587 (1968).

35. D. Epstein and J. B. Keller, "Expansion and Contraction of Planar, Cylindrical, and Spherical Underwater Gas Bubbles", Journal of the Acoustical Society of America 52, 975-980 (1972).

36. H. G. Flynn, "Cavitation Dynamics I. A Mathematical Formulation", Journal of the Acoustical Society of America 57, 1379-1396 (1975).

37. G. J. Lastman and R. A. Wentzell, "Comparison of Five Models of Spherical Bubble Response in an Inviscid Compressible Liquid", Journal of the Acoustical Society of America 69, 638-642 (1981).

38. A. Prosperetti, "Acoustic cavitation series part two - Bubble phenomena in sound fields: part one", Ultrasonics 22, 69-77 (1984).

39. J. B. Keller and M. Miksis, "Bubble Oscillations of Large Amplitude", Journal of the Acoustical Society of America 68, 628-633 (1980).

40. S. A. Zwick, Journal of Mathematics and Physics 37, 246 (1958).

41. M. Fanelli, A. Prosperetti, and M. Reali, "Radial Oscillations of Gas-Vapor Bubbles in Liquids. Part I: Mathematical Formulation", Acustica 47, 253-265 (1981).

42. A. Prosperetti, "Acoustic cavitation series: part three - Bubble phenomena in sound fields: part two", Ultrasonics 22, 115-124 (1984).

43. L. A. Crum, "Measurements of the growth of air bubbles by rectified diffusion", Journal of the Acoustical Society of America 68, 203-211 (1980).

44. A. Prosperetti, "A Generalization of the Rayleigh-Plesset Equation of Bubble Dynamics", Physics of Fluids 25, 409-410 (1982).

45. H. B. Callen, Thermodynamics, John Wiley & Sons, New York (1960).

46. G. D. Smith, Numerical Solution of Partial Differential Equations: Finite Difference Methods, Oxford University Press, Oxford (1978).

47. R. C. Weast, ed., Handbook of Chemistry and Physics 56th edition, CRC Press, Cleveland (1975).

48. C. F. Gerald, Applied Numerical Analysis, Addison-Wesley Pub. Co., Reading, MA (1980).

49. G. E. Forsythe, M. A. Malcolm, and C. B. Moler, Computer Methods for Mathematical Computations, Prentice-Hall, Inc., Englewood Cliffs, NJ (1977).

50. A. Prosperetti, A private communication on application of numerical methods to sytems of ordinary and partial differential equations, (1985).

51. G. M. Hansen, "Mie scattering as a technique for the sizing of air bubbles", Applied Optics (to be published).

52. W. Lauterborn, "Numerical investigation of nonlinear oscillations of gas bubbles in liquids", Journal of the Acoustical Society of America 59, 283-293 (1976).

53. L. A. Crum, "Bjerknes forces on bubbles in a stationary sound field", Journal of the Acoustical Society of America 57, 1363-1370 (1975).

54. J. Guckenheimer and P. Holmes, Nonlinear oscillations, Dynamical Systems, and Bifurcations of Vector Fields, Springer-Verlag, New York (1983).

55. G. Contopoulos, "Infinite Bifurcations, Gaps and Bubbles in Hamiltonian Systems", Physica 8D, 142-156 (1983).

56. E. Knobloch and N. O. Weiss, "Bifurcations in a Model of Magnetoconvection", Physica 9D, 379-407 (1983).

57. G. Schmidt and B. H. Wang, "Alternate routes to chaos in Hamiltonian systems", preprint, Physics Dept., Stevens Institute of Technology (1983).

58. G. Duffing, "Erzwungene Schwingungen bei veranderlicher Eigenfrequenz und ihre technische Bedeutung", Vieweg, Braunschweig (1918).

59. U. Parlitz and W. Lauterborn, "Superstructure in the Bifurcation Set of the Duffing Equation", Physics Letters 107A, 351-355 (1985).

60. M. W. Hirsch and S. Smale, Differential Equations, Dynamical Systems, and Linear Algebra, Academic Press, New York (1974).

61. P. Coullet and D. Sornette, A private communication on the nature of the bifurcation in figure 30, (1985).

APPENDIX

A. Computer program for the exact formulation

The following FORTRAN program was used to make calculations for the compressible exact theory, which was denoted by CE. This program outputs the radius, internal pressure, and center temperature as a function of time. The modifications necessary to calculate the levitation numbers, frequency response curves, temperature profiles, and Feigenbaum tree are not shown. However, each of these modifications is straightforward to implement in the computer program.

The input parameters necessary to run the program are REQ, AMP, LAMBDA, NN, NTMSTP, NCYCLE, AND IPRINT, where

REQ is the equilibrium radius of the bubble in microns,

AMP is the driving pressure amplitude in atmospheres,

LAMBDA is the fraction of the resonance frequency at which the bubble is driven,

NN is the number of nodes (finite difference points) in the bubble,

NTMSTP is the number of time steps in 1 period of the driving pressure,

NCYCLE is the number of cycles of the driving pressure integrated over,

IPRINT is the fraction of the points that are output (1/IPRINT).

```
      PROGRAM CE
C
C                    VERSION 1.0    MARCH 5, 1985
C
C     THIS PROGRAM USES A PREDICTOR-CORRECTOR METHOD TO SOLVE THE
C     NONLINEAR SET OF EQUATIONS FOR RADIAL BUBBLE OSCILLATIONS.
C
C*******************************************************************
C
C               DEFINITION OF CONSTANTS & VARIABLES
C
C     GAM    = RATIO OF SPECIFIC HEATS - DIMENSIONLESS
C     RHOL   = DENSITY OF LIQUID - GRAMS/CC
C     F      = DRIVING FREQUENCY - HERTZ
C     REQ    = EQUILIBRIUM RADIUS OF BUBBLE - CENTIMETERS
C     PINF   = UNDISTURBED LIQUID PRESSURE - DYNES/CM/CM
C     SIGMA  = SURFACE TENSION - DYNES/CM
C     AMU    = LIQUID VISCOSITY - POISE
C     AMP    = DRIVING PRESSURE AMPLITUDE IN ATMOSPHERES
C     EPS    = DIMENSIONLESS PRESSURE AMPLITUDE AMP/PINF
C     KINF   = THERMAL CONDUCTIVITY OF AIR @ EQUILBRIUM COND. -
C              ERGS/(SEC*CM*DEG.KELVIN)
C     TINF   = AMBIENT LIQUID TEMPERATURE - DEGREES KELVIN
C     PO     = INTERNAL PRESSURE OF BUBBLE @ EQUIL. - DYNES/CM/CM
C     W      = RADIAL DRIVING FREQUENCY - RADIANS/SEC
C     DO     = THERMAL DIFFUSIVITY OF AIR @ EQUIL. - CM*CM/SEC
C     NN     = NUMBER OF FINITE DIFFERENCE POINTS IN BUBBLE
C     NTMSTP = NUMBER OF DIMENSIONLESS TIME STEPS IN ONE PERIOD
C     R      = DIMENSIONLESS RADIUS
C     RTL    = R TILDA @ N+1 TIME STEP
C     RP1    = DIMENSIONLESS @ N+1 TIME STEP
C     RST    = R STAR
C     U      = DIMENSIONLESS VELOCITY (BUBBLE WALL)
C     UTL    = U TILDA @ N+1 TIME STEP
C     UPR    = DU/DT @ TIME STEP N
C     UP1    = DIMENSIONLESS VELOCITY @ N+1 TIME STEP
C     UST    = U STAR
C     P      = DIMENSIONLESS INTERIOR PRESSURE
C     PTL    = P TILDA @ N+1 TIME STEP
C     PPR    = DP/DT @ TIME STEP N
C     PTLPR  = DPTL/DT @ N+1 TIME STEP
C     PST    = P STAR
C     PSTPR  = P STAR PRIME
C     PP1    = DIMENSIONLESS INTERIOR PRESSURE @ N+1 TIME STEP
C     T      = DIMENSIONLESS TIME
C     K      = DIMENSIONAL THERMAL CONDUCTIVITY OF AIR
C     VEL    = VELOCITY OF SOUND IN LIQUID IN CM/SEC
C     D      = DIMENSIONLESS THERMAL DIFFUSIVITY OF AIR
```

BIOGRAPHICAL SKETCH OF THE AUTHOR

Kerry Wayne Commander was born in Clarksdale, Mississippi on May 25, 1958, the son of Mr. G. D. Commander, Jr. and Mrs. R. W. Tedford. He attended Lee Academy in Clarksdale, graduating in May, 1976. He received a B.S. in mathematics and physics from the University of Mississippi in August, 1980. Continuing his studies at the University of Arizona, he received a M.S. in applied mathematics in August, 1982.

Kerry is a member of Sigma Pi Sigma, Pi Mu Epsilon, Phi Kappa Phi, The American Physical Society, The Society for Industrial and Applied Mathematics, and The Acoustical Society of America. He enjoys basketball, softball, water sports, flying, and hiking. For the immediate future, he plans to pursue a career in research and development outside the university circle.

His permanent address is Rt. 1 Box 121, Lyon, Mississippi 38645.

```
      OMO=DSQRT(OMO)
      DO 20 K=1,20
      THETA=R*DSQRT(2.*OMO/DIFF)
      EX=0.0
      IF(THETA.LT.10.0)EX=DEXP(-THETA)
      ST=2.*DSIN(THETA)
      CT=2.*DCOS(THETA)
      APLUS=(1.+EX*(ST-EX))/(1.+EX*(EX-CT))
      AMINUS=(1.-EX*(ST+EX))/(1.+EX*(EX-CT))
      T1=(THETA+THG1*AMINUS)*THETA
      T2=THG1*(THETA*APLUS-2.)
      DEN=T1*T1+T2*T2
      KAPPA=GAM*THETA*THETA*T1/DEN
      OMOLD=OMO
      OMO=PRR2*(3.*KAPPA+(3.*KAPPA-1.)*W)
      OMO=DSQRT(OMO)
      IF(DABS(OMO/OMOLD-1.0).LT.1.D-4)GOTO 40
20    CONTINUE
      GOTO 400
40    CONTINUE
      AIMPHI=3.*GAM*T2*THETA*THETA/DEN
      BETTH=.5*PIO*AIMPHI/(RHOL*OMO*R*R)
      BETAC=.5*OMO*OMO*R/VEL
      BETAV=2.*AMUL/(RHOL*R*R)
      FO=OMO/6.283185307179586
      THETA=R*DSQRT(2.*OMO/DIFF)
      BETA=BETTH+BETAV+BETAC
400   CONTINUE
      RETURN
      END
```

```
      DDR2=H*DDER
      R=RI+.5*DR2
      DR=DRI+.5*DDR2
      DDER=DER(R,DR,TT)
      DR3=H*DR
      DDR3=H*DDER
      R=RI+DR3
      DR=DRI+DDR3
      TT=T+H
      DDER=DER(R,DR,TT)
      DR4=H*DR
      DDR4=H*DDER
      RO=RI+(DR1+DR4+2.*(DR2+DR3))/6.
      DRO=DRI+(DDR1+DDR4+2.*(DDR2+DDR3))/6.
      RETURN
      END
C
      DOUBLE PRECISION FUNCTION DER(R,DR,T)
      IMPLICIT REAL*8(A-H,O-Z)
      REAL*8 KAPPA,LAMBDA
      COMMON/SET1/AMP,KAPPA,LAMBDA
      COMMON/COST/PAR,AMTH,AMEFF,PI,PIPOL
      COMMON/Q/W,PIO
      COMMON/SET4/THREEK,OMW
C
C PIPOL = P INTERNAL POLYTROPIC
C PI = PIPOL - THERMAL DAMPING CONTRIBUTION
C
      PIPOL=1./R**THREEK
      PI=PIPOL-AMTH*DR/R
      DER=PI-W/R-AMEFF*DR/R-OMW*(1.-AMP*DSIN(T))
      DER=(PAR*DER-1.5*DR*DR)/R
      RETURN
      END
C
      SUBROUTINE RESNCE(R)
      IMPLICIT REAL*8(A-H,O-Z)
      REAL*8 KAPPA
      COMMON/SET1/AMP,KAPPA,LAMBDA
      COMMON/PARAMS/GAM,DIFF,PINF,RHOL,SIGMA,VEL,AMUL
      COMMON/RES/FO,AIMPHI,BETTH,BETAV,BETAC,BETA
      COMMON/Q/W,PIO
      PIO=PINF+2.*SIGMA/R
      THG1=3.*(GAM-1.)
      PRR2=PINF/(RHOL*R*R)
      W=2.*SIGMA/(R*PINF)
      KAPPA=1.2
      OMO=PRR2*(3.*KAPPA+(3.*KAPPA-1.)*W)
```

```fortran
      H2=H/2.
      EPS=1.D-7
      EPSB=1.D-8
C
      DO 40 K=1,32500
C
      CALL RUNGE(RO,DRO,RA,DRA,T,H)
 20   CONTINUE
      CALL RUNGE(RO,DRO,RB,DRB,T,H2)
      T=T+H2
      CALL RUNGE(RB,DRB,RC,DRC,T,H2)
      T=T+H2
      IF(DABS(DRC).LT.EPSB)GOTO 30
      ERR=DABS(DRA/DRC-1.)
      IF(ERR.LT.EPS) GO TO 30
      RA=RB
      DRA=DRB
      T=T-H
      H=H2
      H2=H/2.
      GO TO 20
 30   CONTINUE
      RO=RC
      DRO=DRC
      DDER=DER(RO,DRO,T)
 35   PRES=DSIN(T)
      WRITE(1,38)RO,T
      WRITE(2,38)PI,T
      IF(T.GE.TMAX)GOTO 200
 38   FORMAT(F12.6)
 36   IF(ERR.GT.EPSB)GO TO 40
      H2=H
      H=2.*H2
 40   CONTINUE
 200  CONTINUE
      RETURN
      END
C
      SUBROUTINE RUNGE(RI,DRI,RO,DRO,T,H)
      IMPLICIT REAL*8(A-H,O-Z)
      DDER=DER(RI,DRI,T)
      DR1=H*DRI
      DDR1=H*DDER
      R=RI+.5*DR1
      DR=DRI+.5*DDR1
      TT=T+H/2.
      DDER=DER(R,DR,TT)
      DR2=H*DR
```

```
      COMMON/PARAMS/GAM,DIFF,PINF,RHOL,SIGMA,VEL,AMUL
      BETTHR=BETTH
      AIMPHR=AIMPHI
      BETACR=BETAC
      R0=1.0
      DR0=0.0
      H=6.283185307179586D-2
      OMW=1.-W
      OMO=6.283185307179586*FO
      OM=LAMBDA*OMO
      PAR=PIO/(RHOL*(OM*R)*(OM*R))
      AMVIS=4.*AMUL*OM/PIO
      THETA=R*DSQRT(2.*OM/DIFF)
      EX=0.0
      IF(THETA.LT.10.0)EX=DEXP(-THETA)
      ST=2.*DSIN(THETA)
      CT=2.*DCOS(THETA)
      APLUS=(1.+EX*(ST-EX))/(1.+EX*(EX-CT))
      AMINUS=(1.-EX*(ST+EX))/(1.+EX*(EX-CT))
      T1=(THETA+3.*(GAM-1)*AMINUS)*THETA
      T2=3.*(GAM-1.)*(THETA*APLUS-2.)
      DEN=T1*T1+T2*T2
      AIMPHN=3.*GAM*T2*THETA*THETA/DEN
      KAPPA=GAM*THETA*THETA*T1/DEN
      THREEK=3.0*KAPPA
      BETACN=.5*OM*OM*R/VEL
      BETTHN=.5*PIO*AIMPHN/(RHOL*R*R*OM)
      BETTH=BETTHR
      AIMPHI=AIMPHR
      BETAC=BETACR
      IF(OPTTH.EQ.1.0)GOTO 10
C
C  NOW COMPUTE THE THERMAL DAMPING AT OM RATHER THAN OMO
C
      AIMPHI=AIMPHN
      BETTH=BETTHN
      BETAC=BETACN
C
10    CONTINUE
      AMAC=2.*RHOL*OM*R*R*BETAC/PIO
      AMTH=AIMPHI
C
C  NEXT STATEMENT IS FOR NO THERMAL DAMPING
C     AMTH=0.0
C
      AMEFF=AMVIS+AMAC
      TMAX=6.283185307179586*NNNN
      T=0.0D0
```

```fortran
      PROGRAM RPP
      IMPLICIT REAL*8(A-H,O-Z)
      REAL*8 KAPPA,LAMBDA,RDSK
      COMMON/COST/PAR,AMTH,AMEFF,PI,PIPOL
      COMMON/SET1/AMP,KAPPA,LAMBDA
      COMMON/SET2/NNNN
      COMMON/SET3/WRK,NTM1,DT
      COMMON/PARAMS/GAM,DIFF,PINF,RHOL,SIGMA,VEL,AMUL
C
C  OPTTH=0.0 GIVES NONRESONANCE VALUES:1.0 GIVES RESONANCE
      OPTTH=0.0
C
      GAM=1.4
      DIFF=0.2
      PINF=1.013D6
      RHOL=1.0
      AMUL=1.0D-2
      SIGMA=72.8
      VEL=1.481D5
C
      WRITE(5,55)
   55 FORMAT('  INPUT RO, LAMBDA, PA, NO. OF CYCLES')
      READ(5,*)RDIM,LAMBDA,PA,NNNN
C
      R=RDIM*1.0D-4
      AMP=PA
      PA=PA*1.0D6
C
      CALL RESNCE(R)
C
      WRITE(5,56)
   56 FORMAT(1H )
C
      CALL WORK(R,OPTTH)
C
      STOP
      END
C
      SUBROUTINE WORK(R,OPTTH)
      IMPLICIT REAL*8(A-H,O-Z)
      REAL*8 KAPPA,LAMBDA
      COMMON/SET5/DELAY,TR1
      COMMON/SET2/NNNN
      COMMON/SET1/AMP,KAPPA,LAMBDA
      COMMON/SET4/THREEK,OMW
      COMMON/Q/W,PIO
      COMMON/RES/FO,AIMPHI,BETTH,BETAV,BETAC,BETA
      COMMON/COST/PAR,AMTH,AMEFF,PI,PIPOL
```

B.   Computer program for the Rayleigh-Plesset polytropic equation

The following FORTRAN program was used to make calculations for the Rayleigh-Plesset equation using the polytropic approximation. The integration is carried out using a fourth order Runge-Kutta algorithm. The output from this program is radius and internal pressure as a function of time.

The input parameters necessary to run the program are RDIM, LAMBDA, PA, NNNN, where,

RDIM is the equilibrium radius of the bubble in microns,

Lambda is the fraction of the resonance frequency at which the bubble is driven,

PA is the driving pressure amplitude in atmospheres, and

NNNN is the number of cycles of the driving pressure amplitude integrated over.

```fortran
      RETURN
      END
C
C     TRIDIAGONAL SYSTEM SOLVER
C
      SUBROUTINE TRIDG(VEC)
      DIMENSION DI1(51),DI2(51),DI3(51),RHS(51),VEC(51)
      COMMON/SET2/DI1,DI2,DI3,RHS,NM1,N
      DO 10 I=1,NM1
      DI2(I+1)=DI2(I+1)-DI3(I)*DI1(I)/DI2(I)
   10 RHS(I+1)=RHS(I+1)-RHS(I)*DI1(I)/DI2(I)
      VEC(N)=RHS(N)/DI2(N)
      DO 20 M=NM1,1,-1
   20 VEC(M)=(RHS(M)-DI3(M)*VEC(M+1))/DI2(M)
      RETURN
      END
```

```
        WRITE(1,96)R,T
        WRITE(2,96)P,T
        WRITE(3,96)TG(1),T
 96     FORMAT(F12.5)
1000 CONTINUE
1100 CONTINUE
C
C
        STOP
        END
C
C       SUBROUTINE TO CALCULATE RESONANCE FREQUENCY F0
C
        SUBROUTINE RESNCE(R,F0)
        REAL KAPPA,LAMBDA
        COMMON/SET1/GAM,PINF,RHOL,SIGMA,VEL,AMUL,KINF,TINF
        PIO=PINF+2.*SIGMA/R
        THG1=3.*(GAM-1.)
        DIFF=(GAM-1.0)*KINF*TINF/(GAM*PIO)
        DIFF=.2
        PRR2=PINF/(RHOL*R*R)
        W=2.*SIGMA/(R*PINF)
        KAPPA=1.2
        OMO=PRR2*(3.*KAPPA+(3.*KAPPA-1.)*W)
        OMO=SQRT(OMO)
        DO 20 K=1,20
        THETA=R*SQRT(2.*OMO/DIFF)
        EX=0.0
        IF(THETA.LT.10.0)EX=EXP(-THETA)
        ST=2.*SIN(THETA)
        CT=2.*COS(THETA)
        APLUS=(1.+EX*(ST-EX))/(1.+EX*(EX-CT))
        AMINUS=(1.-EX*(ST+EX))/(1.+EX*(EX-CT))
        T1=(THETA+THG1*AMINUS)*THETA
        T2=THG1*(THETA*APLUS-2.)
        DEN=T1*T1+T2*T2
        KAPPA=GAM*THETA*THETA*T1/DEN
        OMOLD=OMO
        OMO=PRR2*(3.*KAPPA+(3.*KAPPA-1.)*W)
        OMO=SQRT(OMO)
        IF(ABS(OMO/OMOLD-1.0).LT.1.E-4)GOTO 40
 20     CONTINUE
        WRITE(5,30)
 30     FORMAT('      NO CONVERGENCE IN SUBROUTINE RESNCE')
        GOTO 400
 40     CONTINUE
        F0=OMO/6.2831853
400     CONTINUE
```

```
C
      RST2=RST*RST
      DUM1=3.0*DTDY2*CHI*DST(1)/RST2
      DI2(1)=1.0+DUM1
      DI3(1)=-DUM1
      RHS(1)=TAU(1)+.5*DT*(DTAUDT(1)+DST(1)*PSTPR)
         DO 80 I=2,NN
      TERM=(DTDY2*CHI/(2.0*RST2))*(GM1G*(.5*(TAUST(I+1)-TAUST(I-1))
     1+Y(I)*TAUST(NN))/PST)
      DI1(I-1)=-TERM-(DTDY2*CHI/(2.0*RST2))*DST(I)*YM(I)
      DI2(I)=1.0+DTDY2*CHI*DST(I)/RST2
      DI3(I)=TERM-DST(I)*YP(I)*(DTDY2*CHI/(2.0*RST2))
      RHS(I)=TAU(I)+.5*DT*(DTAUDT(I)+DST(I)*PSTPR)
   80    CONTINUE
C
      CALL TRIDG(TAUP1)
C
C        OTHER CORRECTOR EQUATIONS
C
      MACH=UST/C
      DRIVER=PFP0*(1.0-EPS*SIN(T+DT+RST/DUME))
      DUM1=1.0+(DT/(2.0*RST*(1.0-MACH)))*(1.5*UST*(1.0-MACH/3.0)+CAPP*
     1(1.0+MACH)*CAPM/RST)
      DUM2=U+.5*DT*(UPR+CAPP*((PST-DRIVER-CAPW/RST)*(1.0+MACH)+
     1(1.0+0.0)*RST*PSTPR/C)/(RST*(1.0-MACH)))
      UP1=DUM2/DUM1
      RP1=R+.5*DT*(U+UP1)
      PP1=P+.5*DT*(PPR-3.0*GM1*CHI*TAUP1(NN)/(DY*RP1*RP1))
      PP1=PP1/(1.0+1.5*GAM*DT*UP1/RP1)
         DO 85 I=1,NN
      TGP1(I)=(SQRT(1.0+GM1G2A*TAUP1(I))-BETA)/ALPHA
      DP1(I)=(ALPHA*TGP1(I)+BETA)*TGP1(I)/PP1
   85    CONTINUE
C
C******************************************************************
C
C                UPDATE AND OUTPUT AREA
C
      T=TCC+FLOAT(J)*6.28318531/FLOAT(NTMSTP)
      R=RP1
      P=PP1
      U=UP1
         DO 90 I=1,NN
      TG(I)=TGP1(I)
      TAU(I)=TAUP1(I)
      D(I)=DP1(I)
   90    CONTINUE
      IF(MOD(J,IPRINT).NE.0)GOTO 1000
```

```
        RTL=R+DT*U
        RTL2=RTL*RTL
        DRIVER=PFP0*(1.0-EPS*SIN(T+R/DUME))
        UPR=-1.5*U*U*(1.-MACH/3.)+CAPP*((P-DRIVER-(CAPW+CAPM*U)/R)
       1*(1.0+MACH)+(1.0+0.0)*R*PPR/C)/(R*(1.0-MACH))
        UTL=U+DT*UPR
        PTLPR=3.0*(GM1*CHI*(-TAUTL(NN))/RDY-GAM*PTL*UTL)/RTL
C
C           START OF FIRST CORRECTOR SECTION
C
C        TRI-DIAGONAL SOLUTION FOR TAUST = TAU STAR @ N+1 STEP
C
        DUM1=3.0*DTDY2*CHI*DTL(1)/RTL2
        DI2(1)=1.0+DUM1
        DI3(1)=-DUM1
        RHS(1)=TAU(1)+DT*(DTAUDT(1)+DTL(1)*PTLPR)/2.0
          DO 70 I=2,NN
        TERM=(DTDY2*CHI/(2.0*RTL2))*(GM1G*(.5*(TAUTL(I+1)-TAUTL(I-1))
       1+Y(I)*TAUTL(NN))/PTL)
        DI1(I-1)=-TERM-(DTDY2*CHI/(2.0*RTL2))*DTL(I)*YM(I)
        DI2(I)=1.0+DTDY2*CHI*DTL(I)/RTL2
        DI3(I)=TERM-DTL(I)*YP(I)*(DTDY2*CHI/(2.0*RTL2))
        RHS(I)=TAU(I)+.5*DT*(DTAUDT(I)+DTL(I)*PTLPR)
   70     CONTINUE
C
        CALL TRIDG(TAUST)
C
C        OTHER CORRECTOR EQUATIONS
C
        MACH=UTL/C
        DUM1=1.0+(DT/(2.0*RTL*(1.0-MACH)))*(1.5*UTL*(1.0-MACH/3.0)+CAPP*
       1(1.0+MACH)*CAPM/RTL)
        DRIVER=PFP0*(1.0-EPS*SIN(T+DT+RTL/DUME))
        DUM2=U+.5*DT*(UPR+CAPP*((PTL-DRIVER-CAPW/RTL)*(1.0+MACH)+
       1(1.0+0.0)*RTL*PTLPR/C)/(R*(1.0-MACH)))
        UST=DUM2/DUM1
        RST=R+.5*DT*(U+UST)
        PST=P+.5*DT*(PPR-3.0*GM1*CHI*TAUST(NN)/(DY*RST*RST))
        PST=PST/(1.0+1.5*GAM*DT*UST/RST)
        PSTPR=3.0*(GM1*CHI*(-TAUST(NN))/(RST*DY)-GAM*PST*UST)/RST
          DO 75 I=1,NN
        TGST(I)=(SQRT(1.0+GM1G2A*TAUST(I))-BETA)/ALPHA
        DST(I)=(ALPHA*TGST(I)+BETA)*TGST(I)/PST
   75     CONTINUE
C
C           SECOND CORRECTOR EQUATIONS START HERE
C
C        TRI-DIAGONAL SOLUTION FOR TAUP1 = NEW VALUE OF TAU @ N+1 STEP
```

```fortran
        Y(II)=Y(II-1)+DY
        YP(II)=1.0+DY/Y(II)
        YM(II)=1.0-DY/Y(II)
        TG(II)=1.0
        TAU(II)=0.0
 50     CONTINUE
C
C******************************************************************
C
C          USEFUL EXPREESSIONS TO SAVE COMPUTATIONAL TIME
C
        DUME=W*C
        DY2=DY*DY
        DY22=DY2*2.0
        DTDY2=DT/DY2
C
C******************************************************************
C
C                         WORK AREA
C
        DO 1100 II=1,NCYCLE
        TCC=(II-1)*6.283185307
          TYPE *,II
        DO 1000 J=1,NTMSTP
C
C          START OF PREDICTOR ROUTINE
C
        R2=R*R
        RDY=R*DY
        R2DY2=R2*DY2
        PPR=-3.0*(GM1*CHI*TAU(NN)/RDY+GAM*P*U)/R
        PTL=P+DT*PPR
        DTAUDT(1)=D(1)*(6.0*CHI*(TAU(2)-TAU(1))/R2DY2+PPR)
        TAUTL(1)=TAU(1)+DT*DTAUDT(1)
        TGTL(1)=(SQRT(1.0+GM1G2A*TAUTL(1))-BETA)/ALPHA
        DTL(1)=(ALPHA*TGTL(1)+BETA)*TGTL(1)/PTL
          DO 60 I=2,NN
        DTAUDT(I)=D(I)*((CHI/R2DY2)*(YP(I)*TAU(I+1)-2.0*TAU(I)+
       1YM(I)*TAU(I-1))+PPR)-(GM1G*CHI/(R2*P))*((TAU(I+1)-TAU(I-1))/2.0
       2+Y(I)*TAU(NN))*(TAU(I+1)-TAU(I-1))/DY22
        TAUTL(I)=TAU(I)+DT*DTAUDT(I)
        TGTL(I)=(SQRT(1.0+GM1G2A*TAUTL(I))-BETA)/ALPHA
        DTL(I)=(ALPHA*TGTL(I)+BETA)*TGTL(I)/PTL
 60     CONTINUE
C
C    REST OF PREDICTOR CALCULATIONS
C
        MACH=U/C
```

```
C
C        CALCULATION OF THE RESONANCE FREQUENCY F0
C
        CALL RESNCE(REQ,F0)
C
C                       DERIVED CONSTANTS
C
        F=F0*LAMBDA
        EPS=AMP/PINF
        DT=6.2831853/FLOAT(NTMSTP)
        DELAY=6.2831853*(NCYCLE-2)
        DY=1.0/FLOAT(NN)
        NP1=NN+1
        NM1=NN-1
        P0=PINF+2.0*SIGMA/REQ
        PFP0=PINF/P0
        W=6.2831853*F
        C=VEL/(W*REQ)
        GM1=GAM-1.0
        GM1G=GM1/GAM
        D0=GM1G*KINF*TINF/P0
        CHI=D0/(W*REQ*REQ)
        CAPP=P0/(RHOL*W*W*REQ*REQ)
        CAPW=2.0*SIGMA/(REQ*P0)
        CAPM=4.0*AMU*W/P0
        ALPHA=M*TINF/KINF
        BETA=B/KINF
        GM1G2A=2.0*GM1G*ALPHA
C
C****************************************************************
C
C
C                       INITIAL CONDITIONS
C
        R=1.0
        P=1.0
        T=0.0
        U=0.0
        D(1)=1.0
        TG(1)=1.0
        TG(NP1)=1.0
        TAU(1)=0.0
        TAU(NP1)=0.0
        DTAUDT(NP1)=0.0
        Y(1)=0.0
        Y(NP1)=1.0
C NOTE- YP & YM @ 1 ARE NOT REQUIRED IN COMPUTATIONS.
        DO 50 II=2,NN
        D(II)=1.0
```

```
C       DST    = D STAR
C       DTL    = D TILDA
C       DP1    = D ARRAY AT NEW TIME STEP
C       TG     = DIMENSIONLESS INTERIOR GAS TEMPERATURE ARRAY
C       TGTL   = TG TILDA
C       TGST   = TG STAR
C       TGP1   = TG @ N+1 TIME STEP
C       TAU    = DIMENSIONLESS INTERIOR GAS TEMPERATURE ARRAY
C       TAUTL  = TAU TILDA
C       TAUST  = TAU STAR
C
C******************************************************************
C
      REAL KINF,M,K,LAMBDA,MACH
      DIMENSION TGTL(51),TGST(51)
      DIMENSION DI1(51),DI2(51),DI3(51),RHS(51),DP1(51)
      DIMENSION D(51),DST(51),DTL(51),Y(51),YM(51),YP(51),DTAUDT(51)
      DIMENSION TG(51),TGP1(51),TAU(51),TAUTL(51),TAUST(51),TAUP1(51)
      COMMON/SET1/GAM,PINF,RHOL,SIGMA,VEL,AMU,KINF,TINF
      COMMON/SET2/DI1,DI2,DI3,RHS,NM1,NN
C
C******************************************************************
C
C                      INPUT FROM TERMINAL
C
      WRITE(5,10)
  10  FORMAT(' INPUT RADIUS IN MICRONS, PA, AND LAMBDA')
      READ(5,*)REQ,AMP,LAMBDA
      WRITE(5,20)
  20  FORMAT(' INPUT NN, NTMSTP, NCYCLE, AND IPRINT')
      READ(5,*)NN,NTMSTP,NCYCLE,IPRINT
      REQ=REQ*1.0E-4
      AMP=AMP*1.013E6
C
C******************************************************************
C
C                          CONSTANTS
C
      M=5.528
      B=1165.0
      GAM=1.4
      RHOL=0.998
      PINF=1.013E6
      SIGMA=72.8
      AMU=0.01
      TINF=293.15
      KINF=TINF*M+B
      VEL=1.481E5
```

END

FILMED

10-85

DTIC